Imaging and diagnostic of sub-wavelength micro-structures, from closed-form algorithms to deep learning

Peipei Ran

Thèse de doctorat

NNT : 2020UPASG061

université PARIS-SACLAY

Imaging and diagnostic of sub-wavelength micro-structures, from closed-form algorithms to deep learning

Thèse de doctorat de l'Université Paris-Saclay

École doctorale n° 580, Sciences et technologies de l'information et de la communication (STIC)
Spécialité de doctorat : Traitement du signal et des images
Unité de recherche : Université Paris-Saclay, CNRS, CentraleSupélec, Laboratoire des signaux et systèmes, 91190, Gif-sur-Yvette, France
Référent : Faculté des sciences d'Orsay

Thèse présentée et soutenue en visioconférence totale le 15 décembre 2020, par

Peipei RAN

Composition du jury:

Thomas Rodet Professeur, Ecole Normale Supérieure Paris-Saclay	Président
Oliver Dorn Maître de conférences, Université de Manchester	Rapporteur & Examinateur
Rémi Douvenot Professeur, Ecole Nationale de l'Aviation Civile	Rapporteur & Examinateur
Sandor Bilicz Maître de conférences, Université de Technologie et d'Economie de Budapest	Examinateur
Sébastien Lambot Professeur, Directeur de recherche FNRS, Université Catholique de Louvain	Examinateur
Joe LoVetri Professeur, Université de Manitoba	Examinateur
Peter Maaß Professeur Dr., Université de Brême	Examinateur
Dominique Lesselier Directeur de recherche émérite, CNRS	Directeur de thèse
Mohammed Serhir Professeur Adjoint, CentraleSupélec	Invité, Co-encadrant
Roberto Miorelli Ingénieur de recherche, CEA	Invité

Acknowledgements

I wish to express my appreciation to my supervisor Dr. Dominique Lesselier, Directeur de Recherche, Centre National de la Recherche Scientifique (CNRS). He is a really good supervisor, he always tries his best to give me help in the research, and he provides lots of communication opportunities with the smart researchers all over the world, which greatly broadened my academic view.

I also would like to thank a lot my co-supervisor Dr. Mohammed Serhir, now at GeePs, CentraleSupélec. He helps me a lot for the implementation of experiments and good suggestions on the research direction. My warm thanks are given to my colleague and friend Yingying Qin, who is now at Ecole Normale Supérieure Paris-Saclay, we have cooperated a lot.

During the study at the Laboratoire des signaux et systèmes (L2S), I have been feeling really lucky to work with Dr. Marc Lambert and Dr. Vincent Lescarret, they give me smart suggestions and pratical help during my work. Dr. Roberto Miorelli also gave me smart suggestions during my PhD study.

I would like to thank Dr. Sandor Bilicz, Professor Sébastien Lambot, Professor Joe Lovetri, Professor Peter Maaß, and Professor Thomas Rodet for serving as my jury members, Dr. Oliver Dorn and Dr. Rémi Douvenot as referees, Dr. Roberto Miorelli and Dr. Mohammed Serhir as invited members.

I want to thank my boyfriend Nan Deng, who is a PhD student in ENSTA, he encourages me and gives supports from life to work, I'm so lucky to have him with me during these years. I also wish to express thanks to Li Wang, Shanshan Wang and Jun Zhu, they are my best friends, we have spent lots of happy time together, their company is my precious wealth.

My great appreciation goes to my parents and grandparents for their never-ending love, they teach me that being happy everyday is the most important thing, and they support me to do what I want to do and encourage me to be who I want to be, they are my strongest backing.

Résumé et introduction en français

Le contexte de recherche

Les micro-structures telles que celles étudiées dans ce travail doctoral sont généralement constituées d'un certain nombre d'éléments de même nature, qui sont distribués de manière périodique dans une certaine région de l'espace (dite *Region of Interest* ou ROI), et la taille de ces éléments et leur séparation possèdent des caractéristiques de sous-longueur d'onde, ici mesurées par rapport à la longueur d'onde d'opération si il s'agit de signaux mono-fréquences ou à la bande de fréquence concernée s'il s'agit de signaux multi-fréquences (ou impulsionnels).

Si les cristaux phononiques et photoniques correspondent bien à la description ci-dessus, c'est également le cas notamment des laminés fibrés comme devenus courants dans nombre de pièces aéronautiques et automobiles, tandis que les réseaux d'antennes destinés aux illuminations agiles ainsi qu'aux communications privilégiées peuvent également satisfaire cette description.

Mais comment se comporte une micro-structure si certains éléments ne fonctionnent pas comme prévu, ou sont simplement manquants, ou diffèrent de l'élément nominal, que le phénomène résultant soit apprécié d'ailleurs en terme de rayonnement (par exemple, le réseau) ou en terme de diffusion/diffraction (par exemple, le cristal, le laminé) ?

Une bonne compréhension et une bonne analyse des micro-structures intactes et éventuellement affectées sont donc nécessaires, et nous devons les tester, localiser tout changement significatif et, au mieux, cartographier ce qui se passe dans la micro-structure, en pouvant aller bien au-delà du critère classique de demi-longueur d'onde de résolution de Rayleigh (vu cette déterminante propriété sous-longueur d'onde), même si le champ proche est absent de nos données.

Le cas d'étude

La micro-structure dans le travail présent est constituée d'un ensemble en forme de grille régulière d'un nombre fini de tiges diélectriques cylindriques circulaires, le rayon d'une tige étant assez petit et les tiges adjacentes étant proches les unes des autres, de telles dimensions étant donc plus petites, voire significativement plus petites que la demi-longueur d'onde, comme insisté ci-dessus. Compte tenu de ce phénomène de sous-longueur d'onde, le défi est de parvenir à une localisation significative, améliorée (on parlera d'*enhancement*) en résolution, ou même super-résolue (*super-resolved*).

Cette super-résolution est difficile à obtenir par les méthodes conventionnelles avec l'existence de caractéristiques géométriques sous-longueur d'onde. Cela nécessite donc des approches élaborées et tout particulièrement une utilisation appropriée des a priori, tout en essayant d'atténuer les coûts de calcul et de rester fiable même si les données recueilies sont erronées ou rares.

Pour traiter des systèmes micro-structurés complexes, et de fait celui introduit ci-dessus l'est déjà, malgré simplifications certaines, une compréhension exhaustive de la physique comme support de l'analyse des ondes et des champs est nécessaire, ce qui signifie que la caractérisation des structures matérielles à partir du champ électromagnétique qui est diffracté sous des illuminations données nécessite efforts combinés de modélisation, simulation, imagerie et traitement du signal.

Le modèle computationnel direct

Au début des travaux présents, deux méthodes ont été développées afin de procéder à la modélisation de la micro-structure. La méthode dite de diffraction multiple (*Multiple Scattering Method* ou MST, mais on rencontre d'autres désignations) est spécialisée au cas de tiges cylindriques circulaires et est basée sur des développements en ondes cylindriques rigoureux adaptées à cette géométrie spécifique. Elle est précise pour la structure étudiée car les ondes cylindriques sont aisément prises en compte, et de comportement bien connu. Une autre approche est la méthode des moments (*Method of Moments* ou MoM); elle convertit les équations intégrales qui décrivent le champ en un système linéaire discret, et l'on a choisi par simplicité (tout en maintenant une précision correcte, comme nous l'avons constatée) des fonctions de base d'impulsions (*pulse-basis*) et des fonctions de test en Dirac (*point-matching*).

Chaque méthode présente "plus" et "moins". A titre d'exemple, la MST telle que nous la déployons est donc limitée à notre géométrie circulaire[1]. Ce n'est pas le cas comme il est iévident de la MoM (ainsi, imaginons des sections transversales carrées de tiges), sachant aussi que si le contraste des tiges au sein de la ROI (contraste vu par rapport à l'air qui les entoure en fait) augmente fortement, voire même est associé à des conductivités de tiges métalliques, la MST n'y voit point inconvénient.

Une méthode par discrétisation en temps et en espace est aussi mise en œuvre (*Finite Difference Time Domain* ou FD-TD) en ce travail, quand on s'intéresse au domaine temporel, alors à l'aide d'une plate-forme *open source*, dénommée gprMax —clairement concernée par le radar à pénétration de sol (*Ground Probing Radar* ou GPR) et des objets naturels ou artificiels enfouis en des sols, mais qui s'adapte avec aisance à notre cas de figure. Le cœur de l'algorithme FD-TD est comme bien connu que les dérivées partielles spatiales et temporelles des équations différentielles de Maxwell sont discrétisées, la réponse de l'interaction entre une impulsion fournie par une antenne appropriée et la structure matérielle concernée étant alors obtenue.

Une fois modélisé avec précision et si possible efficacité de calcul le problème direct, permettant donc d'acquérir des données sous des formes variées pour un ensemble de micro-structures, mais plus encore d'insérer les solveurs (MST, MoM, FD-TD) dans les algorithmes d'inversion, le problème inverse (donc d'imagerie, si l'on recherche une carte de contraste, et/ou de diagnostic, si l'on recherche une indication de présence ou d'absence, la première indication de fait contenant la seconde) peut être résolu par différentes méthodes allant des méthodes semi-analytiques —nous les notons *closed-form* dans le titre du manuscrit— aux méthodes d'apprentissage profond, comme discuté ci-après.

L'inversion

Il existe déjà de nombreuses méthodes semi-analytiques bien développées, comme l'approximation de Born distordue (*Distorted (Wave) Born approximation* ou D(W)BA), les méthodes d'optimisations de sous-espaces (*Sub-space Optimization Methods* or SOM), ces dernières qui possèdent de multiples variantes, entre beaucoup d'autres. La méthode d'inversion de source de contraste (*contrast source inversion* ou CSI) est pour sa part l'une des méthodes les plus couramment utilisées pour les problèmes de diffraction inverse,

[1]Des développements plus élaborés permettent de traiter des cylindres non-circulaires, mais ceux-ci sont hors notre cadre d'étude, d'autant plus que les diamètres des tiges sont petits devant la longeur d'onde et que leur apport serait limité.

deux séquences, le contraste et la source de contraste étant alternativement mises à jour par une optimisation de type gradient conjugué en minimisant une fonction objectif (ou fonction coût) qui combine des différences normalisées dans l'équation de données (qui lie les données aux sources dans la structure) et dans l'équation d'état (qui les lie à elles-mêmes).

Ici, nous utilisons non seulement le CSI traditionnel, mais nous profitons également des informations de binarité afin d'assurer une meilleure performance, binaire signifiant que l'état normal (une tige effectivement présente) est représentée par "1", et toute tige manquante est représentée par "0".

Une autre méthode que nous développons est basée sur la parcimonie, c'est-à-dire qu'elle prend celle-ci comme un a priori. En effet, les tiges manquantes sont escomptées être peu nombreuses par rapport au nombre de tiges effectivement présentes, de sorte que ces tiges manquantes peuvent être traitées comme des sources fictives à l'intérieur de la micro-structure investiguée. L'inversion de source équivalente à contrainte de parcimonie (qui implique un développement en ondes cylindriques des champs et est donc basée sur la MST) assure par construction une super-résolution, puisque diagnostic absence/présence, quel que soit le (petit) diamètre d'une tige, mais au prix d'hypothèses fortes sur la micro-structure endommagée, ce sur quoi que l'on vient d'insister.

En contraste avec ce qui précède, les méthodes basées sur les données, ou méthodes d'apprentissage, qui jouent un rôle de plus en plus important dans de multiples communautés de recherche et d'application —on n'entrera pas ici dans l'abondante et croissante litérature, avec insistance sur le traitement du langage naturel, le traitement d'image et la reconnaissance de formes, pour ne citer que quelques domaines applicatifs— ne bénéficient pas des connaissances préalables et elles utilisent à leur place de grands ensembles de données, afin d'apprendre la solution inconnue du problème inverse posé.

Les réseaux de neurones profonds sont notre choix, sachant que l'augmentation du nombre de couches améliore les performances du réseau de neurones, par extraction de caractéristiques couche par couche, la représentation des caractéristiques des échantillons dans l'espace d'origine étant transformée en un nouvel espace de caractéristiques, ce qui facilite classification ou prédiction —de nombreuses contributions existent déjà dans le domaine de l'imagerie, différentes architectures étant aussi appliquées à différentes situations. Notons que nous bénéficions ici de l'adaptabilité d'un GPU et d'un langage élaboré (type Python), qui facilitent nos algorithmiques et simulations.

Deux types de réseaux sont considérés par nous : les réseaux de neurones convolutifs (*Convolutional Neural Network* ou CNN) et les réseaux de neurones récurrents (*Recurrent Neural Network* ou RNN). CNN est un type de réseau neuronal artificiel d'apprentissage

en profondeur conçu à l'origine pour analyser des images visuelles, tandis que RNN est conçu pour traiter des données séquentielles et reconnaître des modèles. Et les combinant en CRNN (*Convolutional Recurrent Neural network*) sera montré novateur et performant.

Ceci est complété par l'utilisation du retournement temporel (*Time Reversal* ou TR) afin de réaliser la localisation d'une source ou d'une ou plusieurs tiges manquantes (vues comme des sources artificielles de contraste localisées dans la ROI).

L'organisation du manuscrit

Le manuscrit est constitué de sept chapitres principaux. Le chapitre 1 décrit le contexte de la recherche et résume la contribution de cette thèse. La modélisation directe du système micro-structuré utilisant deux méthodes différentes, la méthode de diffusion multiple et la méthode des moments, est présentée au chapitre 2. Le chapitre 3 illustre méthode d'inversion à contrainte de parcimonie, et méthode d'inversion de source de contraste, essentiellement avec la binarité étant imposée. L'application des méthodes basées sur les données suit. Le réseau de neurones convolutif est présenté au chapitre 4, et le réseau de neurones récurrent l'est aux chapitre 5 et chapitre 6, les détails de mise en œuvre de la validation expérimentale sont également présentés dans ce chapitre. Le chapitre 7 contient la méthode d'imagerie directe : le retournement temporel, qui, en résumant, enregistre une onde entrante puis retransmet sa version inversée dans le temps. Le chapitre 8 résume le travail accompli et présente quelques perspectives. Les annexes proposent des documents supplémentaires. La dissémination nationale et internationale des résultats est fournie à la fin du manuscrit.

L'expérimentation

Cette expérience en chambre anéchoïque a été réalisée sur deux prototypes de micro-structure diélectrique bien conçus (avec des tiges manquantes), avec la complexité supplémentaire que les antennes utilisées émettrices et réceptrices sont évidemment 3-D, même si les tiges sont assez longues. pour s'adapter à l'hypothèse 2-D susmentionnée, en plus des problèmes d'étalonnage (un champ total est collecté, non pas un champ diffracté, et l'antenne n'est pas un récepteur ou un transmetteur idéal). Au-delà de la transmission des données acquises au CNN ci-dessus, le principal défi est de savoir comment combiner simulations et expériences, par exemple, via des réseaux antagonistes génératifs (*generative adversarial network* ou GAN), nous y reviendrons ci-après.

Sur les résultats

Les performances des différentes méthodes ne peuvent pas être jugées selon un critère simple, ce sont des avantages et des inconvénients, de chacune, et cela, compte tenu de la question effectivement posée. Les méthodes semi-analytiques nécessitent une bonne connaissance de la physique et des mathématiques, elles sont difficiles à comprendre si ces connaissances ne sont pas disponibles. De l'autre côté, de grandes quantités de données sont la condition sine qua none de l'utilisation de méthodes d'apprentissage, mais les performances ne peuvent pas être garanties, car la méthode d'apprentissage en profondeur ressemble dans une bonne mesure à une boîte noire, bien que beaucoup s'efforcent d'obtenir plus d'explications ; comme avec la non-linéarité élevée de la capacité de modélisation de CNN, le RNN apparaît être une bonne approximation de la séquence temporelle, mais il reste encore beaucoup de questions ouvertes.

Dans l'ensemble, la méthode CNN spécialisée en binaire réalise une reconstruction précise de la carte de contraste dans tous les cas étudiés, sauf contrastes vraiment élevés, à la fois en terme de localisation des tiges et en terme de récupération de leurs contrastes, même si des données bruitées sont entrées. Vérité terrain et la carte récupérée sont presque impossibles à distinguer. Le cas binaire concerne la localisation des tiges manquantes, mais le réseau construit peut être utilisé pour obtenir la distribution du contraste aléatoire, comme il est aussi montré.

Comme discuté dans le manuscrit, CRNN présente de bonnes performances sur les données générées par MoM, alors que les performances sur les données générées par FD-TD sont légèrement moins bonnes, et nous n'avons pas pu trouver la raison exacte de cet écart de comportement. Quant à la méthode de "physique expérimentale", le retournement temporel, il présente de bonnes performances non seulement pour le problème de source inverse mais aussi pour le problème de diffraction inverse, étant souligné que la résolution du résultat n'est pas assez élevée, comme prévu —seule la prise en compte de résonances de la structure via l'analyse des singularités de sa fonction de Green (associée à la micro-structure intacte) pourrait le permettre via un développement adéquat de MST.

D'un autre point de vue, l'applicabilité des méthodes est et demeure un sujet de préoccupation. La méthode de parcimonie ne peut pas être transférée facilement pour traiter d'autres problèmes en raison de la modélisation très spécialisée. En revanche, la méthode d'apprentissage souffre moins de ce type de limitations, les méthodes CNN ou RNN ont plus de chances de s'appliquer à des problèmes similaires. Pour être plus précis, avec un réseau bien formé, seules des tâches telles que le réglage des paramètres ou la modification de certaines couches sont nécessaires pour les adapter à d'autres

micro-structures, qui seraient différentes en termes de contraste, de nombre, de taille et d'inter-distance des tiges, et aussi de différentes configurations de mesure.

Le cas binaire et le cas aléatoire sont tous deux analysés dans la présente recherche ; le cas binaire concerne la localisation des tiges manquantes, et le cas du contraste aléatoire peut être étendu aux cas généraux de reconstruction d'un objet pour en obtenir les paramètres physiques exacts, la carte de la permittivité ici. Différentes valeurs et différentes formes sont également développées dans cette recherche sur ce type d'extension.

Les travaux envisageables

Bien que la micro-structure sous-longueur d'onde ait été analysée en profondeur, par diverses méthodes, en allant de la modélisation directe à la résolution de problèmes inverses, d'autres explorations apparaissent d'un bon intérêt.

Tout d'abord, la recherche proposée est toujours limitée à des situations qui sont bi-dimensionnelles (tiges infiniment longues) ou quasi bi-dimensionnelles (tiges suffisamment longues), aller à trois dimensions complètes (tiges de hauteur finie, e.g., au plus un couple de longueurs d'onde) semble nécessaire, une fois noté que le problème en trois dimensions est plus difficile en termes de modélisation mathématique, simulations numériques, problèmes inverses eux-mêmes, et expérimentations devant supporter les avancées.

Pour ce qui concerne la partie expérimentale, au-delà de la généralisation à trois dimensions, une correction intelligente entre les données de simulation et celles d'expérimentation est nécessaire, en utilisant une méthode comme celle des GAN afin de générer les (des) données simulées, évitant expérimentations manuelles, possiblement chronophages. Pour mémoire, un GAN se compose d'un discriminateur qui estime la probabilité qu'un échantillon donné provienne de l'ensemble de données réel, et d'un générateur qui produit des échantillons synthétiques à partir d'une entrée de variable de bruit. Ce dernier est construit pour capturer la distribution réelle des données afin que les échantillons génératifs puissent "tromper" le discriminateur pour offrir une probabilité élevée.

Sinon, utiliser les méthodes d'analyse et d'apprentissage proposées pour traiter directement les données expérimentales demeure une solution. À l'exception de l'application directe des réseaux de neurones pour les traiter, la combinaison de la physique et des réseaux de neurones est une voie à suivre. Entre autres exemples, une méthode de rétro-propagation fournissant une carte de contraste approximative utilisée comme entrée d'une architecture type U-net se rencontre déjà. L'apprentissage profond peut aussi être intégré dans la CSI pour de nouvelles améliorations. Les RNN, que nous avons considérés en combinaison CRNN avec les CNN, sont aussi prometteurs, en combinant

approche semi-analytique et méthode d'apprentissage, une image profonde étant analysée pour résoudre le problème inverse en association avec une régularisation classique pour surmonter le problème du manque de généralisation après entraînement avec données insuffisantes.

Changement de paradigme, la fusion de données provenant de différentes modalités d'imagerie peut tirer parti de différents comportements. Les méthodes de fusion sont diverses, nous ne les considérons pas ici en détail, mais la méthode bayésienne bénéficie d'une bonne réputation et a fait l'objet de réalisations fructueuses. Quant à une méthode d'apprentissage, elle rassemblerait les données de différents modèles dans plusieurs canaux de l'ensemble de données, de sorte que les réseaux neuronaux puissent apprendre les données en vue de réaliser différents objectifs à partir des informations desdits canaux. Une remarque, ceci s'appliquerait naturellement à des laminés à fibres, pour lesquels ultrasons et ondes millimétriques peuvent facilement se combiner au sein d'un contrôle non destructif, ceci semble moins évident dans notre cas, même s'il existe une littérature originale portant sur des réseaux de fils et retournement temporel en acoustique sonore.

Table of contents

List of figures xvii

List of tables xxi

1 Introduction 1
- 1.1 Research background . . . 1
- 1.2 Outline . . . 5

2 Modelling of the forward problem 7
- 2.1 Multiple scattering method . . . 8
- 2.2 Method of moments . . . 12
- 2.3 Validation of the modelling . . . 16

3 Sparsity constrained inversion and contrast source inversion 19
- 3.1 Sparsity constrained method . . . 19
  - 3.1.1 Results of sparsity-constrained method . . . 24
- 3.2 Contrast source inversion . . . 31
  - 3.2.1 Results of binary-specialized contrast source inversion . . . 34
- 3.3 CSI for reconstruction of random contrast distribution . . . 34

4 Imaging by convolutional neural networks in frequency domain 39
- 4.1 CNN architecture . . . 39
- 4.2 Loss function . . . 43
- 4.3 Training method . . . 43
- 4.4 Training dataset . . . 44
- 4.5 Implementation . . . 44
- 4.6 The binary-specialized CNN: a reference example . . . 45
  - 4.6.1 Different configurations for the test . . . 46
  - 4.6.2 Single frequency vs. multiple frequencies of operation . . . 46

4.6.3 Different data noise ratios . . . 48
4.6.4 Different values of contrast . . . 48
4.6.5 Additional results for different numbers of missing rods and different shapes using binary-specialized CNN . . . 49
4.6.6 Extension to random contrast distribution . . . 49

5 Imaging by recurrent neural networks in time domain 55
5.1 Motivation of using RNN . . . 55
5.2 LSTM structure . . . 59
5.2.1 Dataset . . . 61
5.2.2 Training process . . . 61
5.2.3 Results . . . 62
5.3 Comparison with imaging by convolutional neural networks . . . 65
5.3.1 CNN architecture . . . 65
5.3.2 CNN results . . . 66
5.3.3 Comparison between CNN and RNN . . . 66
5.4 Validation on laboratory-controlled Data . . . 69
5.4.1 The configuration of experiments . . . 69
5.4.2 Results on experimental data . . . 70

6 Imaging by convolutional-recurrent neural networks 75
6.1 Architecture of proposed CRNN . . . 75
6.2 Training process . . . 77
6.3 Results of CRNN . . . 78

7 Direct imaging method: time reversal 83
7.1 Time reversal for localization of source . . . 83
7.2 Time Reversal for localization of missing rods . . . 87

8 Conclusion 91
8.1 Summary of the work as completed . . . 91
8.2 Potential work . . . 93

Appendix A Graf's addition theorem 95

Appendix B The Lippman-Schwinger formulation 97

Appendix C Further complementary material on time reversal I 99

Appendix D Further complementary material on time reversal II 101

Bibliography 103

List of figures

1.1 Structure of the work, the same color means the corresponding process . 5

2.1 Inverse scattering architecture, T: transmitter, R: receiver. 8
2.2 Cylindrical wave expansion coefficients 11
2.3 Division of ROI into N cells 14
2.4 Comparison of two methods (MSM, MOM) for $\epsilon_r = 2.5$ (left) and $\epsilon_r = 10$ (right). 16
2.5 Comparison of two methods (MSM, MOM) for $\epsilon_r = 2.5$ (left) and $\epsilon_r = 10$ with three rods missing. 16

3.1 Sketch of the missing-rod scattering configuration. 19
3.2 Results of localization for three cases: one missing rod, two missing rods, three missing rods, finding missing rods in the micro-structure, here indexed from 1 to 36, left to right, top to bottom, $\epsilon = 2.5$. 25
3.3 Results of localization for three cases: one missing rod, two missing rods, three missing rods, finding missing rods in the micro-structure, here indexed from 1 to 64, left to right, top to bottom, $\epsilon = 2.5$. 26
3.4 left column is the 36-rod case, right column is the 64-rod case, from top to bottom: the radius of the rod c equals $\lambda/10$,$\lambda/12$,$\lambda/14$, the distance between rods d is $\lambda/4$. 27
3.5 left column is the 36-rod case, right column is the 64-rod case, from top to bottom: the distance between rods d equals $\lambda/2$,$\lambda/4$,$\lambda/6$, the radius of rods c is $\lambda/12$. 28
3.6 left column is the 36-rod case, right column is the 64-rod case, from top to bottom: $\epsilon = 2.5$, 5, 7.5. 29
3.7 Results of the binary-specialized CSI without prior position information. 35

3.8 Results of the binary-specialized CSI for three examples of damages in the 16 rods case; left column is the ground truth, right column is the binary-specialized CSI result. 36
3.9 Results of the binary-specialized CSI for three examples of damages in the 36 rods case; left column is the ground truth, right column the binary-specialized CSI result. 37
3.10 Maps provided by CSI. Top to bottom: ground truth, CSI with prior information, CSI without it. Left: 16 rods case, right: 36 rods case. . . . 38

4.1 CNN architecture 40
4.2 convolutional layer 41
4.3 max pooling layer 42
4.4 Example of training set, left: the real part of scattered field, right: the corresponding contrast map of the micro-structure 45
4.5 The error variation as a function of the iteration number. 45
4.6 Results of the binary-specialized CNN for 36 rods, left column is the ground truth, right column is the CNN reconstruction result, from top to bottom the contrast values are 2.5, 4 and 5. 47
4.7 Maps provided by CNN trained by different missing rods cases. Top to bottom: missing 2 rods cases, missing 3 rods cases, missing 4 rods cases, missing 5 rods cases. Left: ground truth, right: binary-specialized CNN reconstruction result. 50
4.8 Test examples for different missing numbers: first row is missing 1 rod case, second and third rows are two missing 6 rods cases: one is a good reconstruction result, another one is an imperfect reconstruction result. . 51
4.9 Test examples for different shapes: from top to bottom: 16 rods, 20 rods, 25 rods, 30 rods 52
4.10 Maps provided by CNN for examples involving 16 rods. Top to bottom: ground truth, CNN result. Left column: example 1 with lower permittivity. Right column: example 2 with higher permittivity. 53
4.11 Maps provided by CNN for examples involving 36 rods. Top to bottom: ground truth, CNN result. Left column: example 1 with lower permittivity. Right column: example 2 with higher permittivity. 54

5.1 RNN cell. 56
5.2 LSTM cell. 57
5.3 GRU cell. 59

5.4 Architecture of the proposed LSTM structure, input: collected field, output: index of rods. 60
5.5 Example of dataset for LSTM, the left part is an example of input, the normalized received field at one receiver for one transmitter, each input should have 18 received signals with 18 transmitters, the right part is an example of rod's index. 60
5.6 Iteration curve during the training. 62
5.7 LSTM retrievals, from top to bottom: 1, 2, and 3 missing rods, the blue line represents the predicted index, the black line represents the true index. 63
5.8 LSTM retrievals for 4 and 5 missing rods, the blue line represents the predicted index, the black line represents the true index. 64
5.9 Proposed CNN structure, input: the collected field, output: the map of RoI. 65
5.10 Example of dataset for CNN, the left part displays the normalized signal collected at the first receiver when the structure is illuminated by the first transmitter, the right part is the corresponding map of the RoI. 66
5.11 CNN retrievals, from top to bottom: 1, 2 and 3 missing rods, the left column shows the CNN retrieved results, the right column shows the ground truth. 67
5.12 CNN retrievals for 4 and 5 missing rods, the left column shows the CNN retrieved results, the right column shows the ground truth. 68
5.13 Configuration of the laboratory-controlled experiment. 69
5.14 Example of collected experimental data. 70
5.15 LSTM retrievals with experimental data, the black line is the ground truth, the blue line shows the RNN results. 72
5.16 CNN retrievals with experimental data, the left part is the ground truth, the right part shows the RNN results, the two upper ones appear as good retrievals, the bottom one as a failed retrieval. 73

6.1 Architecture of proposed CRNN structure. 76
6.2 Details of RNN layer. 76
6.3 Example of dataset. 77
6.4 Iteration curve during the training. 78
6.5 CRNN retrievals when 3 GHz, from top to bottom: 1 missing rod, 2 missing rods, 3 missing rods, blue line represents predicted index, black line represents truth index. 79
6.6 CRNN retrieval with less data, blue line represents predicted index, black line represents truth index. 80

6.7 CRNN retrieval for square shape rod distribution, blue line represents predicted index, black line represents truth index. 81
6.8 CRNN retrieval for 4 (top) and 5 (bottom) missing rods, blue line represents predicted index, black line represents truth index. 82

7.1 Procedure of time reversal. 84
7.2 2D and 3D representations of the time-reversed field for three different source locations within a $20d \times 20d$ box. 85
7.3 Enhancement of resolution, source at center, cross-section along the horizontal axis passing by it, as function of rod permittivity $\epsilon_r = 1$ (no rod) (red), 10 (green) and 100 (blue), Top: TM case, bottom: TE case. 86
7.4 Elementary cell of the system, illustration of areas S_1 and S_2. 87
7.5 Illustration of Time Reversal procedure 87
7.6 Illustration of Time Reversal of one position 88
7.7 Examples of time reversal result 89

8.1 Table of used methods. 92

A.1 Application of the Graf's addition theorem. 95

List of tables

4.1 Errors of reconstruction for different noise levels. 48
4.2 Errors ERR of reconstruction using binary-specialized CNN. 48

Chapter 1

Introduction

1.1 Research background

Micro-structures, the type of object under investigation herein, are usually made of a number of elements of same nature, which are distributed in periodic fashion within a certain region of space most of the time, and the characteristic size of such elements and their separation, which have sub-wavelength features, are measured with respect to the wavelength of operation for the time-harmonic single-frequency signals, or to the frequency band of operation for multi-frequency signals [1], [2]. Micro-structures have applications in industry and daily life, so the good understanding and analysis is necessary.

If phononic and photonic crystals well correspond to the above description, this is also the case with fibered laminates as now common in aeronautic and automotive work pieces, while antenna arrays devoted to agile illuminations as well as to privileged communications can also be seen as fitting to that description. And if considering those situations, people often ask how does a micro-structure behave if some elements do not work as expected or are simply missing or differ from the nominal element, be the resulting phenomenon appreciated in terms of radiation (e.g., the array) or scattering (e.g., the crystal, the laminate).

So, the challenge is multi-fold, since a good understanding and analysis of the intact as well as the possibly affected micro-structures are needed, and since we need to test those, locate any meaningful change, and at best in effect map what is happening in the micro-structure, possibly reaching far beyond the Rayleigh criterion.

Plenty of imaging tools have already been developed in past years, and a microwave imaging method is often chosen for multiple advantages, like the low cost and safe implementation, compared with other methods. For example, ultrasonic methods are

often applied for the characterization of metals and alloys, but it requires a coupling medium, and significant attenuation of the high-frequency components might cause miss-detection. Infra-red thermography is also widely applied, however it does not with the low lossy medium. Lots of methods based on microwave imaging then have been developed, like time reversal, linear sampling, Born approximation, distorded Born approximation, contrast source inversion or subspace-based optimization methods, and so on. Different methods are developed in effect for different situations of application, and each also has its own merits.

The micro-structure in my work contains a grid-like set of a finite number of circular cylindrical dielectric rods, the radius of a rod being quite small and the adjacent rods being close to each other, such dimensions smaller than the sub-wavelength. In view of the sub-wavelength feature, the main challenge is how to achieve meaningful localization, resolution-enhanced or even, super-resolved.

Super-resolution is hard to achieve by conventional methods with the existence of sub-wavelength geometrical features. This calls for smart approaches and also proper use of priors, while trying to mitigate computational costs and being reliable even if data were to be erroneous or scarce. As a result, conventional methods combined with some prior information or data-driven methods can provide some new direction to solve the problem. Some examples of the above are found in the contributions [3] and [4]; the work in [3] is specially dedicated to non-destructive electromagnetic testing with the sparsity-constrained method to diagnose the composite materials. In contrast, the work in [4] is to be applied in the field of telecommunications, using time reversal to realize the super-resolution of an antenna array in order to increase the transmission performance.

To deal with complex micro-structured systems, exhaustive understanding of physics as support of the wave and field analysis is necessary, which means that the characterization of material structures from electromagnetic fields which are scattered under given wave-field illuminations should be analysed in a proper mathematical framework; such a work requires effort on computational modelling, imaging, and signal processing as well.

As the start of my research, two methods have been used to proceed with the forward modelling of the micro-structure. The so-called multiple scattering method (MST) [5], [6] is specialized to the circular cylindrical rod case, and is based on rigorous cylindrical wave expansions tailored to this peculiar geometry[1]. It is quite accurate for the investigated structure as cylindrical waves are easily accounted for.

[1]More elaborate developments, e.g., [7], make it possible to treat non-circular cylinders, but those lie outside our scope of study, especially as the rod diameters are small compared to the wavelength and their contribution would then be limited.

Another approach is the method of moments (MoM) [8]; this method as is well-known converts the integral equations which describe the field into a discrete system, here one has been choosing for the sake of simplicity (with still maintaining proper accuracy) pulse basis functions and delta testing functions. Yet we need to mention that each method has advantages and limitations, as an example the MST as deployed is limited to our specific geometry which is not the case as obvious of the MoM (imagine squared cross-sections of rods).

The Finite Difference Time Domain (FDTD) method is also used for the work in time domain with the help of an open source software named gprMax [9]. The core of FDTD algorithm is that the time-dependent Maxwell's equations are discretized using central-difference approximations to the space and time partial derivatives, and then, to simulate the response of the interaction between the assumed pulse signals and the object interacting with.

Once accurately modeled the forward problem, the inverse one can be solved by different methods from closed-form methods to learning methods. There are already many well developed analytical methods, as said in the above, like the distorted Born approximation, the subspace optimization method and many variants. As for the contrast source inversion (CSI) method, it is one of the most commonly used methods for inverse scattering problems, two sequences, namely, the contrast and the contrast source being alternately updated using the conjugate gradient direction by minimizing an objective function which combines normalized mismatches in the data equation and in the state equation. In the research, we not only use the traditional CSI but we also take advantage of the binary information to achieve a better performance, binary here meaning that the normal status (an effectively present rod) is represented by 1 and any missing rod is represented by 0.

Another method is based on sparsity [10], [11], i.e., it takes sparsity as the prior information [12]. In brief, considering the system faced with, the missing rods are expected to be few compared with the number of normal rods, so those missing rods can be treated as sources inside the periodic structure in the forward modelling. Sparsity-constrained equivalent-source inversion [13], involving cylindrical wave expansion of the field everywhere can thus yield the location of missing rods provided that those are indeed few and that the intact structure is known beforehand, and in doing so it yields super-resolution (in terms of diagnostic of absence/presence of a sub-wavelength-sized rod) yet at the price of strong hypotheses about the damaged micro-structure as just insisted upon.

In an era of explosive data growth, data-driven methods play a more and more important role in different aspects. Unlike aforementioned methods for which the problem is explicitly defined and domain knowledge carefully engineered into the solution, learning methods do not benefit from such prior knowledge and instead they make use of large data sets in order to learn the unknown solution to the inverse problem. A lot of learning methods are applied to solve the electromagnetic problems, one popular machine learning method —support vector regression(SVM)— has created significant results in non-destructive evaluation, artificial neural networks are widely used in the medical imaging problem [14], including imaging and image processing, like medical images segmentation.

Neural networks have been applied to electromagnetic detection for a long time [15]. With the exploration of big data and improvement of computational performance of computers, deep neural networks play a more and more important role among numerous learning methods. The increase of the number of layers improves the performance of the neural network, by layer-by-layer feature extraction, the feature representation of samples in original space is transformed into a new feature space, which makes classification or prediction easier.

Convolutional neural networks (CNN) and recurrent neural networks (RNN) are two of the most important deep learning models [16] and are widely used in tasks like natural language processing, image processing, and pattern recognition, to mention but a few of applicative fields. CNN is a type of artificial deep learning neural network designed to analyse visual images, while RNN is designed to process sequential data and recognize patterns, which has achieved good results in text generation, machine translation, and face detection [17], [18], without pretence to exhaustivity of our tour of the literature.

Quite many contributions are already made by the researchers in the imaging domain, different architectures are applied to different situations [19], [20]. Neural networks learning techniques are also considered to tackle detection and imaging issues in applications of the ground penetrating radar [21], [22], [23], the modified neural network is applied to contribute to antenna design and optimization [24]. Neural networks are also used to analyse model-based sensitivity of non destructive testing systems [25].[26], RNN is used in Magnetic Resonance image reconstruction [27], and there are also existing works that analyse the equivalence between wave dynamics and recurrent neural networks [28].

As introduced in the above, most of the work in this thesis is about the inverse scattering problem related to the probing of a micro-structure, mapping from the scattered field to the dielectric distribution of the region of interest (ROI) containing the said micro-structure being run so as to realize the localization of the missing rods. In effect,

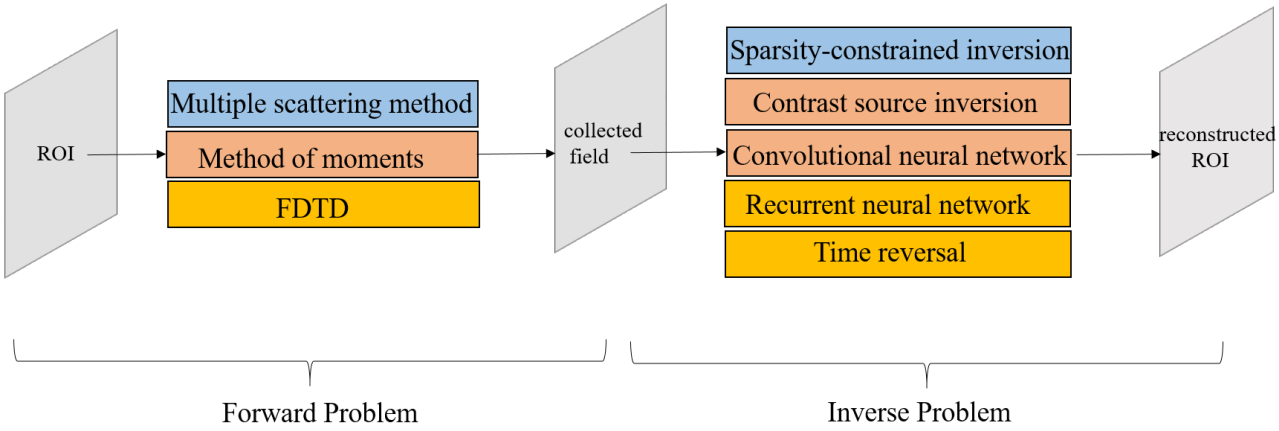

Figure 1.1: Structure of the work, the same color means the corresponding process

some further works like using time reversal in order to realize the localization of a source have also been carried out to investigate the micro-structure from different points of view. Time reversal is a direct imaging method with the help of time reversal mirror [29], [30], it can be carried out in the frequency domain or in the time domain. Time reversal has plenty of applications, for example, telecommunications, source localizations, medical imaging. In the present research, time reversal is used to find the active source and the missing rods, which are consequently regarded as passive sources.

Laboratory-controlled experiments in a microwave anechoic chamber have also been carried out to perform further validation of our research on a micro-structure prototype, experiments being performed in a broad band. The work about these experiments involves calibration of the experimental data and simulated data, and aims at validation of the previous methods, like CNN, using such experimental data.

1.2 Outline

The thesis contains seven main chapters in full. Chapter 1 (this one) describes the background of the research and summarizes the contribution of this thesis. The forward modelling of the micro-structure system using two different methods, namely, multiple scattering method and method of moments, is introduced in Chapter 2. Chapter 3 illustrates two conventional inversion methods: using sparsity prior information inversion method and contrast source inversion method. As for the application of data-driven methods: convolutional neural networks are presented in Chapter 4, recurrent neural networks are presented in Chapter 5 and Chapter 6 for both time domain and frequency

domain, the implementation details of the experimental validation are also introduced in this chapter. Chapter 7 contains the direct imaging method: time reversal, Chapter 8 summarizes the achieved work and outlines some perspectives. In Fig. 1.1, the main work is sketched, here alos including the direct imaging method (time reversal is not strict inversion method, technically). Appendices provide supplementary materials. The dissemination of the work is also listed at the end of the manuscript.

Chapter 2

Modelling of the forward problem

The direct problem is about modelling the physics of the interaction between a known interrogating (electromagnetic) wave and the object, which is supposed to be known as well. The configuration of the system is sketched in Fig. 2.1. Sources and receivers are put outside of the region of interest (ROI) in free space (air), and a finite number of infinitely long circular cylindrical rods, indexed l, counting from left to right, top to bottom in the structure —consider a cross-sectional transverse plane as displayed in the figure—, with same radius c, are periodically arranged inside the ROI with period d (counted in this transverse plane), λ is the wavelength in air, here c and d are smaller even much smaller (the radius) than the wavelength, which means that each rod is thin and close to its neighbours with respect to the wavelength of operation. Rods in the structure are homogeneous, isotropic, their common relative dielectric permittivity being ϵ_r, the relative permeability being unit, $\mu_r = 1$, yet some of the rods may also be absent, with then $\epsilon_r = 1$.

The scattered field is collected by receivers when the structure is illuminated by the transmitters. From the collected field samples, we can attempt to determine the physical or geometrical properties of the probed micro-structure. Emphasize that the essential of the work considered thereafter deals with a Transverse Magnetic or TM field polarization (the electric field is orientated parallel to the axis, unit vector $\mathbf{e}_z$, of the rods, and has only a single component). Examples with the dual Transverse Electric or TE polarization and the corresponding z-orientated single-component magnetic field are found in Chapter 6. Whenever time-harmonic fields, the dependance, implied from now, is e^{-jwt}.

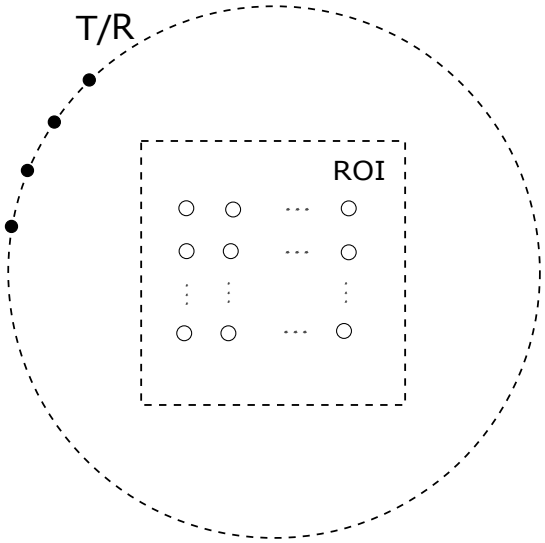

Figure 2.1: Inverse scattering architecture, T: transmitter, R: receiver.

2.1 Multiple scattering method

The multiple scattering method is the mathematical formalism that can be used handily to describe the propagation of a wave through a collection of scatterers, and it is already well applied in acoustics and optics [5]. In the research, as seen, the micro-structure is composed of collection of rods, line sources are used to illuminate the structure, sources are of unit amplitude and radiate a single-component electric field $H_0^{(1)}(kr_s)/4i$, $H_0^{(1)}$ zero-order first-kind Hankel function, r_s the distance between observation point and the line source. For the field of the model described by the multiple scattering method, within the vicinity of the l-th rod, the exterior field in local coordinates is written as

$$E^{ext}(\mathbf{r}) = \sum_{m=-\infty}^{\infty} [A_m^l J_m(kr_l) + B_m^l H_m^{(1)}(kr_l)] e^{im\theta_l}, \tag{2.1}$$

where J_m and $H_m^{(1)}$ are the Hankel function of m-th order and the first-kind Bessel function of m-th order, k is the wave number in air, $\mathbf{r} = (r_l, \theta_l)$ are coordinates of observation point in local coordinate system originated at the center of the l-th rod.

The field outside the rod is a summation of fields scattered by all rods and the one due to the emitting source,

$$E^{ext}(\mathbf{r}) = \sum_{l=1}^{L} \sum_{m=-\infty}^{+\infty} B_m^l H_m^{(1)}(k|\mathbf{r} - \mathbf{c}_l|) e^{im \arg(\mathbf{r}-\mathbf{c}_l)} + \frac{1}{4i} H_0^{(1)}(k|\mathbf{r} - \mathbf{c}_s|). \tag{2.2}$$

where $\mathbf{c}_l$ is the center of l-th rod and $\mathbf{c}_s$ is the center of the source. Applying Graf's addition theorem (refer to Appendix A) to Eq. 2.2,

$$H_m^{(1)}(k|\mathbf{r}-\mathbf{c}_q|)e^{im\arg(\mathbf{r}-\mathbf{c}_q)} = \sum_{p=-\infty}^{+\infty} H_{p-m}^{(1)}(k|\mathbf{c}_q-\mathbf{c}_l|)e^{-i(p-m)\arg(\mathbf{c}_q-\mathbf{c}_l)}J_p(k|\mathbf{r}-\mathbf{c}_l|)e^{ip\arg(\mathbf{r}-\mathbf{c}_l)}, \tag{2.3}$$

$$H_0^{(1)}(k|\mathbf{r}-\mathbf{c}_s|) = \sum_{p=-\infty}^{+\infty} H_p^{(1)}(k|\mathbf{c}_s-\mathbf{c}_l|)e^{-ip\arg(\mathbf{c}_s-\mathbf{c}_l)}J_p(k|\mathbf{r}-\mathbf{c}_l|)e^{ip\arg(\mathbf{r}-\mathbf{c}_l)}, \tag{2.4}$$

then one can exchange m and p and express the global field expansion in the local coordinates of the lth cylinder, so as we get

$$\begin{aligned} E^{ext}(\mathbf{r}) = &\frac{1}{4i}\sum_{m=-\infty}^{+\infty} H_m^{(1)}(kc_{ls})e^{-im\theta_{ls}}J_m(kr_l)e^{im\theta_l} + \sum_{p=-\infty}^{+\infty} B_p^l H_p^{(1)}(kc_l)e^{ip\theta_l} \\ &+ \sum_{q=1,q\neq l}^{L}\sum_{p=-\infty}^{+\infty} B_p^q \sum_{m=-\infty}^{+\infty} H_{m-p}^{(1)}(kc_{lq})e^{-i(m-p)\theta_{iq}}J_m(kr_l)e^{im\theta_l}. \end{aligned} \tag{2.5}$$

By equating the global expansion Eq. 2.5 with the local expansion Eq. 2.1, the following equations are obtained,

$$\begin{aligned} \sum_{m=-\infty}^{\infty} A_m^l J_m(kr_l)e^{im\theta_l} = &\frac{1}{4i}\sum_{m=-\infty}^{+\infty} H_m^{(1)}(kc_{ls})e^{-im\theta_{ls}}J_m(kr_l)e^{im\theta_l} \\ &+ \sum_{q=1,q\neq l}^{L}\sum_{p=-\infty}^{+\infty} B_p^q \sum_{m=-\infty}^{+\infty} H_{m-p}^{(1)}(kc_{lq})e^{-i(m-p)\theta_{iq}}J_m(kr_l)e^{im\theta_l}, \end{aligned} \tag{2.6}$$

$$A_m^l = \frac{1}{4i}H_m^{(1)}(kc_{ls})e^{-im\theta_{ls}} + \sum_{q=1,q\neq l}^{L}\sum_{p=-\infty}^{+\infty} B_p^q H_{m-p}^{(1)}(kc_{lq})e^{-i(m-p)\theta_{iq}}, \tag{2.7}$$

and they can be rewritten as

$$A_m^l = K_m^l + \sum_{q=1,q\neq l}^{L}\sum_{p=-\infty}^{+\infty} S_{mp}^{lq}B_p^q, \tag{2.8}$$

where

$$K_m^l = \frac{1}{4i}H_m^{(1)}(kc_{ls})e^{-im\theta_{ls}}, \tag{2.9}$$

$$S_{mp}^{lq} = H_{m-p}^{(1)}(kc_{lq})e^{-i(m-p)\theta_{iq}}, \tag{2.10}$$

so the matrix form is

$$\mathbf{A} = \mathbf{SB} + \mathbf{K}, \tag{2.11}$$

where $(c_{lq},\, \theta_{lq})$ are the local polar coordinates of $\mathbf{c}_{lq} = \mathbf{c}_l - \mathbf{c}_q$ meaning the position of cylinder q relative to cylinder l, and (c_{ls}, θ_{ls}) are the local polar coordinates $\mathbf{c}_l s = \mathbf{c}_s$- $\mathbf{c}_l$. The interior field expansion within the rod l in such a local system is

$$E^{int}(\mathbf{r}) = \sum_{m=-\infty}^{\infty} [C_m^l J_m(k\sqrt{\epsilon_r} r_l) + Q_m^l H_m^{(1)}(k\sqrt{\epsilon_r} r_l)] e^{im\theta_l}, \tag{2.12}$$

$$Q_m^l = \chi_l J_m(k\sqrt{\epsilon_r} r_l^s) e^{(-im\theta_l^s)}/4i, \tag{2.13}$$

where χ_l equals to 1 if a line source would be present inside and 0 otherwise, (r_l^s, θ_l^s) are polar coordinates of the line source in the local coordinate system associated with the l-th rod. The interior field expansion within the rod l in global coordinates is written as:

$$E^{int}(\mathbf{r}) = \sum_{l=1}^{L} \sum_{m=-\infty}^{+\infty} C_m^l J_m^{(1)}(k\sqrt{\epsilon_r}|\mathbf{r} - \mathbf{c}_l|) e^{im \arg(\mathbf{r}-\mathbf{c}_l)} + \frac{1}{4i} H_0^{(1)}(k\sqrt{\epsilon_r}|\mathbf{r} - \mathbf{c}_s|). \tag{2.14}$$

The boundary continuity conditions shown in Fig. 2.2 are expressed in terms of cylindrical harmonic reflection and transmission coefficients as:

$$B_m^l = R_m^l A_m^l + T_m^l Q_m^l, \tag{2.15}$$

$$C_m^l = T_m'^l A_m^l + R_m'^l Q_m^l, \tag{2.16}$$

or in matrix form,

$$\mathbf{B} = \mathbf{RA} + \mathbf{TQ}, \tag{2.17}$$

$$\mathbf{C} = \mathbf{T}'\mathbf{A} + \mathbf{R}'\mathbf{Q}, \tag{2.18}$$

$$\mathbf{B} = (\mathbf{I} - \mathbf{RS})^{-1}(\mathbf{RK} + \mathbf{TQ}). \tag{2.19}$$

To calculate the reflection and transmission coefficients, the boundary conditions at a smooth enough boundary between a medium 1 and a medium 2, with the cylindrical coordinate system, for the TM case of our main interest, the angular and radial components

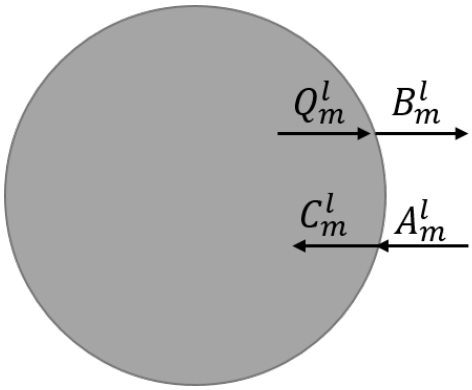

Figure 2.2: Cylindrical wave expansion coefficients

of the electric field being null, read as

$$\frac{\partial E_1}{\partial r}|_{r_l=a_l} = \frac{\partial E_2}{\partial r}|_{r_l=a_l}, \tag{2.20}$$

$$\frac{\partial E_1}{\partial \theta}|_{r_l=a_l} = \frac{\partial E_2}{\partial \theta}|_{r_l=a_l}, \tag{2.21}$$

where a_l is the radius of the l-th cylinder, actually in the structure all the rod has same radius $a_l = c$. Upon application of the relation in Eq. 2.1 and Eq. 2.12,

$$k\sum_{m=-\infty}^{\infty}[A_m^l J_m'(ka_l)+B_m^l H_m^{(1)'}(ka_l)]e^{im\theta_l} = k\sqrt{\epsilon_r}\sum_{m=-\infty}^{\infty}[C_m^l J_m'(k\sqrt{\epsilon_r}a_l)+Q_m^l H_m^{(1)'}(k\sqrt{\epsilon_r}a_l)]e^{im\theta_l}, \tag{2.22}$$

$$i\sum_{m=-\infty}^{\infty} m[A_m^l J_m(ka_l)+B_m^l H_m^{(1)}(ka_l)]e^{im\theta_l} = i\sum_{m=-\infty}^{\infty} m[C_m^l J_m(k\sqrt{\epsilon_r}a_l)+Q_m^l H_m^{(1)}(k\sqrt{\epsilon_r}a_l)]e^{im\theta_l}. \tag{2.23}$$

From Eq. 2.22 and Eq. 2.23, one can know the expression of B_m^l, and from the comparison with the Eq. 2.19, one can get the values of R_m^l T_m^l $R_m^{l'}$ $T_m^{l'}$ as:

$$R_m^l = -\frac{\sqrt{\epsilon_r}J_m'(k\sqrt{\epsilon_r}a_l)J_m(ka_l) - J_m(k\sqrt{\epsilon_r}a_l)J_m'(ka_l)}{\sqrt{\epsilon_r}J_m'(k\sqrt{\epsilon_r}a_l)H_m^{(1)}(ka_l) - J_m(k\sqrt{\epsilon_r}a_l)H_m^{(1)'}(ka_l)}, \tag{2.24}$$

$$T_m^l = \frac{\sqrt{\epsilon_r}J_m(k\sqrt{\epsilon_r}a_l)H_m^{(1)'}(ka_l) - \sqrt{\epsilon_r}J_m'(k\sqrt{\epsilon_r}a_l)H_m^{(1)}(k\sqrt{\epsilon_r}a_l)}{J_m(k\sqrt{\epsilon_r}a_l)H_m^{(1)'}(ka_l) - n_l J_m'(k\sqrt{\epsilon_r}a_l)H_m^{(1)}(ka_l)}, \tag{2.25}$$

$$R_m^{l'} = -\frac{\sqrt{\epsilon_r}H_m'(k\sqrt{\epsilon_r}a_l)H_m^{(1)}(ka_l) - H_m^{(1)}(k\sqrt{\epsilon_r}a_l)H_m^{(1)}(ka_l)}{\sqrt{\epsilon_r}J_m'(kn_la_l)H_m^{(1)}(ka_l) - J_m(k\sqrt{\epsilon_r}a_l)H_m^{(1)'}(ka_l)}, \tag{2.26}$$

$$T_m^{l'} = \frac{J_m(ka_l)H_m^{(1)'}(ka_l) - J_m'(ka_l)H_m^{(1)}(ka_l)}{J_m(k\sqrt{\epsilon_r}a_l)H_m^{(1)'}(ka_l) - \sqrt{\epsilon_r}J_m'(k\sqrt{\epsilon_r}a_l)H_m^{(1)}(ka_l)}. \tag{2.27}$$

From these values, one can calculate the **A**, **B**, **C**, **Q**, so that the field can be gotten. The field calculated by the multiple scattering method is well applied in the time reversal direct imaging method, and the sparsity-constrained inversion method, more detail is in next chapters.

2.2 Method of moments

The interaction between wave and object is described in this approach by the Helmholtz wave equation. Applying the Green's theorem to this equation and taking into account the conditions of continuity of the fields and of radiation at infinity, the forward problem can be appraised from an integral representation of the electric field consisting of two coupled integral equations: observation and state equations. The solution of the direct problem requires the discrete counterparts of these integral equations which are obtained in an algebraic framework using the method of moments [8].

Letting the $p-$th transmitter illuminating the ROI, the state equation describes the electric field

$$E_p^{tot}(\mathbf{r}) = E_p^{inc}(\mathbf{r}) + k^2 \int_D g(\mathbf{r}, \mathbf{r}')\chi(\mathbf{r}')E_p^{tot}(\mathbf{r}')d\mathbf{r}', \mathbf{r} \in D, \tag{2.28}$$

where $E_p^{tot}(\mathbf{r})$ is the total electric field, $E_p^{inc}(\mathbf{r})$ the incident field, and $g(\mathbf{r}, \mathbf{r}')$ the 2-D scalar Green's function, $\chi(\mathbf{r})$ being the dielectric contrast defined as $\epsilon_r(\mathbf{r}) - 1$, D is the region of interest. The other equation is the observation equation

$$E_p^{sca}(\mathbf{r}) = k^2 \int_D g(\mathbf{r}, \mathbf{r}')\chi(\mathbf{r}')E_p^{tot}(\mathbf{r}')d\mathbf{r}', \mathbf{r} \in S, \tag{2.29}$$

where $E_p^{sca}(\mathbf{r})$ is the scattered field, S is the region of observation. Here, one defines $J_p(\mathbf{r}) = \chi(\mathbf{r})E_p^{tot}(\mathbf{r})$ as the contrast source, and henceforth considers operators G_s and G_d as

$$G_s(\mathbf{J}_p) = k_0^2 \int_D g(\mathbf{r}, \mathbf{r}')J_p(\mathbf{r}')d\mathbf{r}', \mathbf{r} \in S, \tag{2.30}$$

$$G_d(\mathbf{J}_p) = k_0^2 \int_D g(\mathbf{r}, \mathbf{r}') J_p(\mathbf{r}') d\mathbf{r}', \mathbf{r} \in D, \tag{2.31}$$

so the equations can be concatenated as

$$E_p^{tot}(\mathbf{r}) = E_p^{inc}(\mathbf{r}) + G_d(\chi \mathbf{E_p^{tot}}), \mathbf{r} \in D, \tag{2.32}$$

$$E_p^{sca}(\mathbf{r}) = G_s(\chi \mathbf{E_p^{tot}}), \mathbf{r} \in S. \tag{2.33}$$

From these two equations the value of $\mathbf{E}_p^{tot}$ and $\mathbf{E}_p^{sca}$ can be calculated. The method of moments is used to that effect, with pulse basis functions and delta testing functions, in order to convert the integral equations into a linear system solved numerically.

Let L be a linear operator $L : G \to H$, and $h = L(g)$ where $g \in G$ and $h \in H$, the purpose here is determine g as knowing L and h. The function g can be written in the form $g = \sum_{i=1}^{I} \alpha_i u_i$, where α_i is constant coefficient $u_1, u_2, ..., u_I$ are a set of basis functions. The property of linearity of the operator L is

$$h = L(g) = L(\sum_{i=1}^{I} \alpha_i u_i) = \sum_{i=1}^{I} \alpha_i L u_i. \tag{2.34}$$

To approach Eq. 2.34 by a discrete linear system, a set of test functions $t_1, t_2, .., t_N$ is introduced, so,

$$\langle t_n, h \rangle_H = \sum_{i=1}^{I} \alpha_i \langle t_n, L u_i \rangle, \forall n = 1, ..., N, \tag{2.35}$$

where $\langle ., . \rangle_H$ is a scalar product on H such as $\langle t_n, h \rangle_H = \int_H t_n(x) h^*(x) dx$. By omitting the index H, we can obtain the algebraic writing $h = L\alpha$ with

$$L = \begin{bmatrix} \langle t_1, Lu_1 \rangle & \langle t_1, Lu_2 \rangle & \dots & \langle t_1, Lu_I \rangle \\ \langle t_2, Lu_1 \rangle & \langle t_2, Lu_2 \rangle & \dots & \langle t_2, Lu_I \rangle \\ \vdots & \vdots & \ddots & \vdots \\ \langle t_N, Lu_1 \rangle & \langle t_N, Lu_2 \rangle & \dots & \langle t_N, Lu_I \rangle \end{bmatrix}, \alpha = \begin{bmatrix} \alpha_1 \\ \vdots \\ \alpha_I \end{bmatrix}, h = \begin{bmatrix} \langle t_1, h \rangle \\ \vdots \\ \langle t_N, h \rangle \end{bmatrix},$$

so $\alpha = L^{-1} h$, then the value of $g = \sum_{i=1}^{I} \alpha_i u_i$ is determined. The method of moments is used to solve the state and observation equations, the choice of basis functions and test functions essentially depends upon the nature of the physical state. The ROI is divided into N small square subunits D_n, whose centres are located at $\mathbf{r}_i$ $(i = 1, 2, ..., N)$. One take basis functions as the characteristic functions of the pixels partitioning the domain D, hence field and permittivity are assumed to be constant within each pixel. $E(\mathbf{r})$ and

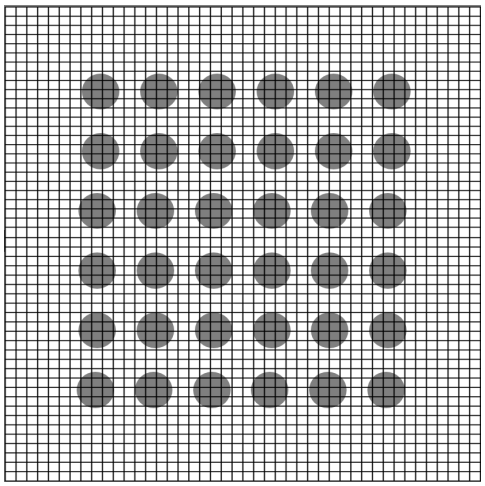

Figure 2.3: Division of ROI into N cells

$\chi(\mathbf{r})$ are approximated by using pulse basis functions defined over the square cells:

$$E(\mathbf{r}) = \sum_{i=1}^{N} E_i f(\mathbf{r_i} - \mathbf{r}), \tag{2.36}$$

$$\chi(\mathbf{r}) = \sum_{i=1}^{N} \chi_i f(\mathbf{r_i} - \mathbf{r}), \tag{2.37}$$

where $f(\mathbf{r_i} - \mathbf{r})$ is the basis function defined as

$$f(\mathbf{r_i} - \mathbf{r}) = \begin{cases} 1 \ \mathbf{r} \in D_i \\ 0 \ \mathbf{r} \notin D_i \end{cases} \tag{2.38}$$

where χ is a $N \times 1$ vector storing the samples of $\chi(r)$. The test functions are a distribution of Dirac δ located at the center of the pixels, so

$$E^{inc}(\mathbf{r}) = \sum_{i=1}^{N} E_i^{inc} \delta(\mathbf{r_i} - \mathbf{r}), \ \delta(\mathbf{r_i} - \mathbf{r}) = \begin{cases} 1 \ \mathbf{r} = \mathbf{r}_i \\ 0 \ \mathbf{r} \neq \mathbf{r}_i \end{cases} \tag{2.39}$$

So, upon projection of the basis functions onto the state equation:

$$E^{tot}(\mathbf{r}) = E^{inc}(\mathbf{r}) + k_0^2 \sum_{i=1}^{N} \int_{D_i} g(\mathbf{r}, \mathbf{r}') f(\mathbf{r} - \mathbf{r}') d\mathbf{r}' \chi_i E_i^{tot}, \tag{2.40}$$

then one projects the test functions by Eq. 2.39

$$E_j^{tot} = E_j^{inc} + k_0^2 \sum_{i=1}^{N} \int_{D_i} g(\mathbf{r}, \mathbf{r}') f(\mathbf{r}_j - \mathbf{r}') d\mathbf{r}' \chi_i E_i^{tot}, j = 1, ..., N, \tag{2.41}$$

thus the linear system to be solved is

$$E_j^{inc} = \sum_{i}^{N} [\delta_{ji} - G_{ij}\chi_i] E_i^{tot} \; with \; G_{ij} = k_0^2 \int_{D_i} g(\mathbf{r}_j, \mathbf{r}') d\mathbf{r}' \tag{2.42}$$

$$\begin{bmatrix} E_1^{inc} \\ E_2^{inc} \\ \vdots \\ E_N^{inc} \end{bmatrix} = \begin{bmatrix} 1 - G_{11}\chi_1 & G_{12}\chi_2 & \dots & G_{1N}\chi_N \\ G_{21}\chi_1 & 1 - G_{22}\chi_2 & \dots & G_{2N}\chi_N \\ \vdots & \vdots & \ddots & \vdots \\ G_{N1}\chi_1 & 1 - G_{N2}\chi_2 & \dots & 1 - G_{NN}\chi_N \end{bmatrix} \times \begin{bmatrix} E_1^{tot} \\ E_2^{tot} \\ \vdots \\ E_N^{tot} \end{bmatrix},$$

so the result is

$$\begin{bmatrix} E_1^{tot} \\ E_2^{tot} \\ \vdots \\ E_N^{tot} \end{bmatrix} = \begin{bmatrix} 1 - G_{11}\chi_1 & G_{12}\chi_2 & \dots & G_{1N}\chi_N \\ G_{21}\chi_1 & 1 - G_{22}\chi_2 & \dots & G_{2N}\chi_N \\ \vdots & \vdots & \ddots & \vdots \\ G_{N1}\chi_1 & 1 - G_{N2}\chi_2 & \dots & 1 - G_{NN}\chi_N \end{bmatrix}^{-1} \times \begin{bmatrix} E_1^{inc} \\ E_2^{inc} \\ \vdots \\ E_N^{inc} \end{bmatrix}.$$

Similarly, by applying

$$E^{tot} = \sum_{i=1}^{N} E_i^{tot} f(\mathbf{r}_i - \mathbf{r}), \tag{2.43}$$

$$\chi(\mathbf{r}) = \sum_{i=1}^{N} \chi_i f(\mathbf{r}_i - \mathbf{r}), \tag{2.44}$$

the observation equation for $z-$th receiver,

$$E_z^{sca}(\mathbf{r}) = k_0^2 \sum_{i=1}^{N} \left[\int_{D_i} g(\mathbf{r}, \mathbf{r}') \right] \chi_i E_i^{tot} d\mathbf{r}', \tag{2.45}$$

where $\int_{D_i} g(\mathbf{r}, \mathbf{r}')$ can be calculated easily. For N_r receivers,

$$\begin{bmatrix} E_1^{sca} \\ E_2^{sca} \\ \vdots \\ E_{N_r}^{sca} \end{bmatrix} = \begin{bmatrix} G_{11} & G_{12} & \dots & G_{1N} \\ G_{21} & G_{22} & \dots & G_{2N} \\ \vdots & \vdots & \ddots & \vdots \\ G_{N_r1} & G_{N_r2} & \dots & G_{N_rN} \end{bmatrix} \times \begin{pmatrix} \chi_1 & & & 0 \\ & \chi_2 & & \\ & & \ddots & \\ 0 & & & \chi_N \end{pmatrix} \times \begin{bmatrix} E_1^{tot} \\ E_2^{tot} \\ \vdots \\ E_N^{tot} \end{bmatrix}$$

As demonstrated above, by using MoM, a discrete version of the problem is obtained. The field calculated by MoM is used in the contrast source inversion method and the CNN application, as detailed in next chapters.

2.3 Validation of the modelling

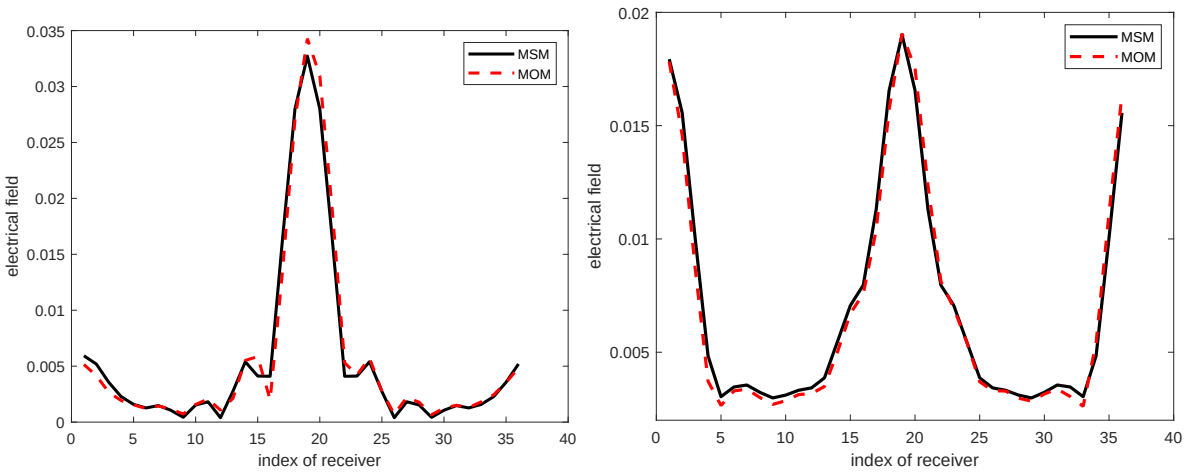

Figure 2.4: Comparison of two methods (MSM, MOM) for $\epsilon_r = 2.5$ (left) and $\epsilon_r = 10$ (right).

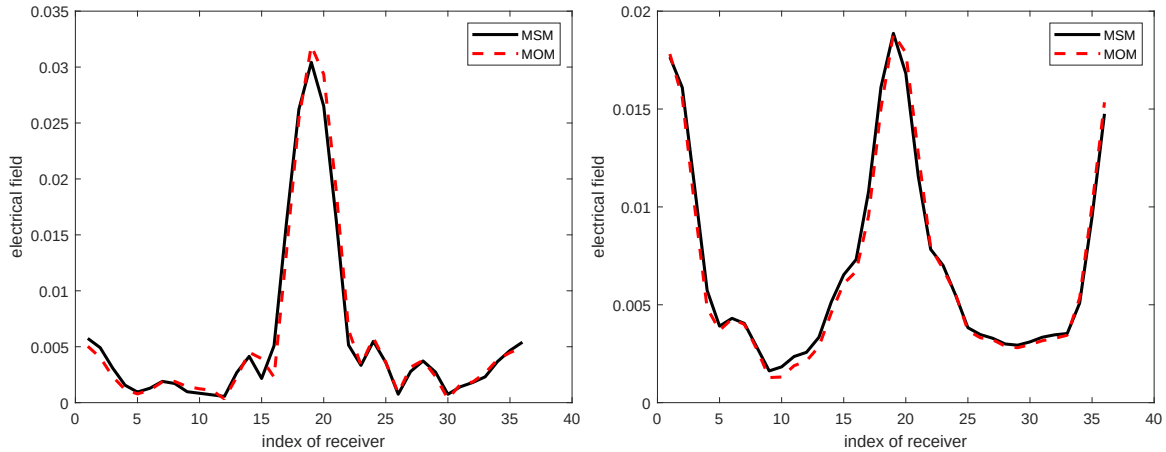

Figure 2.5: Comparison of two methods (MSM, MOM) for $\epsilon_r = 2.5$ (left) and $\epsilon_r = 10$ with three rods missing.

To validate the reliability of the proposed two methods, in Fig. 2.4, the two methods based on Multiple Scattering Method (MSM) and MoM are compared. The parameter of the structure for the comparison are that d equals $\lambda/12$, r equals $\lambda/12$ and D equals 7.2λ,

the source is at the position(7.2λ, 0), and 36 receivers are used to collect the scattered field.

As shown, not only for the case shown here when the dielectric contrast is equal to 2.5, but in effect as observed up to such a contrast reaching of the order of 10, the scattered fields calculated by both methods match; though there still exists a difference at some receivers, which might be caused by the discrimination of MoM, i.e., the number of cells used in it, herein the region of interest in divided into 50×50 cells, and/or the truncation of the cylinder wave expansion (the upper mode number being automatically chosen, and a number of previous references quoted therein) within the MSM.

The calculated fields for the structure which contains missing rods are shown in Fig. 2.5, the two methods still match well. One thing should be mentioned, the MSM takes much less time than the MoM, since the computational time of MoM depends upon the number of cells, for example, using 50×50 cells takes a relative short time compared with the 80×80 cells respecting to achieving the same calculated field accuracy.

Chapter 3

Sparsity constrained inversion and contrast source inversion

3.1 Sparsity constrained method

The imaging performances are expected to be better if more prior information about the probed object is provided. Here, the missing rods can be treated as equivalent (fictitious) sources of unknown location inside the structure. The equivalence theory provides a link between the collected data and the expansion coefficients of equivalent sources, the non-zero elements of which indicate the index of a missing rod. With data from sources and receivers in use, the solution is achieved by sparsity-constrained method hereafter.

The possibility of finding missing rods by analysing its electromagnetic responses relies on the perturbation of the background field due to the missing rods. The evaluation of this perturbation is performed with the Lippman-Schwinger integral formulation:

$$\widetilde{E}(\mathbf{r}) - E(\mathbf{r}) = \sum_{l}^{L} \int_{D_l} G(\mathbf{r}, \mathbf{r}')(k_l^2 - k^2 \epsilon_r) \widetilde{E}(\mathbf{r}') d\mathbf{r}' \tag{3.1}$$

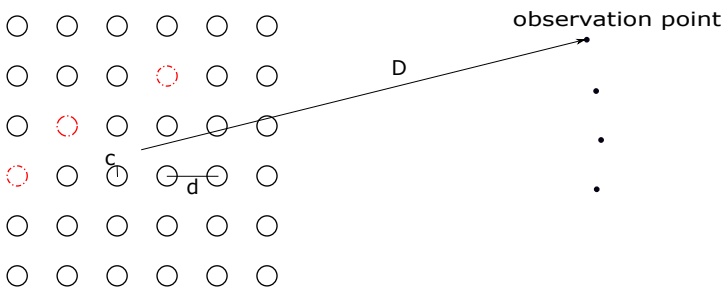

Figure 3.1: Sketch of the missing-rod scattering configuration.

where $\mathbf{E}$ denotes the total field by the well-organized structure and parameters with $\sim$ above are associated with the disorganized structure with missing rods, D_l is the surface area of the l-th missing rod, and $G(\mathbf{r}, \mathbf{r}')$ is the Green's function for the case that the line source is located at $\mathbf{r}'$ when there is no missing rod in the structure. That is

$$G(\mathbf{r}, \mathbf{r}') = \sum_{j=1}^{L} \sum_{m=-\infty}^{\infty} B_m^j(\mathbf{r}') H_m^{(1)}(kr_j) e^{im\theta_j}, \tag{3.2}$$

and

$$\widetilde{E}(\mathbf{r}') = \sum_{m'=-\infty}^{\infty} \widetilde{C}_{m'}^{l} J_{m'}(k_l r_l') e^{im'\theta_l'}, \tag{3.3}$$

within which (r_l', θ_l') are polar coordinates of r' in the local coordinate system with respect to the l-th missing rod. Substituting Eq. 3.2 and Eq. 3.3 into Eq. 3.1,

$$\begin{aligned}
\widetilde{E}(\mathbf{r}) - E(\mathbf{r}) &= \sum_{l}^{L} \int_{D_l} \sum_{j=1}^{L} \sum_{m=-\infty}^{\infty} B_m^j(\mathbf{r}') H_m^{(1)}(kr_j) e^{im\theta_j} (k_l^2 - k^2\epsilon_r) \sum_{m'=-\infty}^{\infty} \widetilde{C}_{m'}^{l} J_{m'}(k_l r_l') e^{im'\theta_l'} d\mathbf{r}' \\
&= \sum_{j=1}^{L} \sum_{m=-\infty}^{\infty} H_m^{(1)}(kr_j) e^{im\theta_j} (k_l^2 - k^2\epsilon_r) \sum_{m'=-\infty}^{\infty} \sum_{l=1}^{L} \widetilde{C}_{m'}^{l} \int_{D_l} B_m^j(\mathbf{r}') J_{m'}(k_l r_l') e^{im'\theta_l'} d\mathbf{r}' \\
&= \sum_{j=1}^{L} \sum_{m=-\infty}^{\infty} H_m^{(1)}(kr_j) e^{im\theta_j} (k_l^2 - k^2\epsilon_r) \sum_{m'=-\infty}^{\infty} \sum_{l=1}^{L} \widetilde{C}_{m'}^{l} \upsilon
\end{aligned} \tag{3.4}$$

where $\upsilon = \int_{D_l} B_m^j(\mathbf{r}') J_{m'}(k_l r_l') e^{im'\theta_l'} d\mathbf{r}'$, in υ, $B_m^j(\mathbf{r}')$ is calculated by Eq. 3.6, since no exterior source in the derivation of the Green's function, $\mathbf{K} = 0$. Then B_m^j can be expressed as

$$\mathbf{B} = (\mathbf{I} - \mathbf{RS})^{-1}\mathbf{TQ}. \tag{3.5}$$

Denoting $\mathbf{W} = (\mathbf{I} - \mathbf{RS})^{-1}\mathbf{T}$, so $\mathbf{B} = \mathbf{WQ}$, since the Green's function is calculated with only a line source located inside the l-th rod, $B_m^j(\mathbf{r}')$ is calculated by

$$B_m^j(\mathbf{r}') = \sum_{n=-\infty}^{\infty} W_{l,n}^{j,m} \frac{1}{4i} J_n(k\sqrt{\epsilon_r} r_l') e^{-in\theta_l'} \tag{3.6}$$

in which $W_{l,n}^{j,m}$ indicates the element corresponding to l-th rod and n-th mode, and j-th rod and m-th mode. So,

$$\begin{aligned}\upsilon &= \int_{D_l} B_m^j(\mathbf{r}') J_{m'}(k_l r_l') e^{im'\theta_l'} d\mathbf{r}' \\ &= \int_0^c \int_0^{2\pi} \sum_{n=-\infty}^{\infty} W_{l,n}^{j,m} \frac{1}{4i} J_n(k\sqrt{\epsilon_r} r_l') e^{-in\theta_l'} J_{m'}(k_l r_l') e^{im'\theta_l'} dr_l' d\theta_l' \\ &= \sum_{n=-\infty}^{\infty} W_{l,n}^{j,m} \frac{1}{4i} \int_0^c J_n(k\sqrt{\epsilon_r} r_l') J_{m'}(k_l r_l') dr_l' \int_0^{2\pi} e^{-in\theta_l'} e^{im'\theta_l'} d\theta_l',\end{aligned} \tag{3.7}$$

two formulas are applied to solve the equation

$$\int_0^{2\pi} e^{-in\theta_l'} e^{im'\theta_l'} d\theta_l' = 2\pi\delta(m'-n), \tag{3.8}$$

and

$$\int x J_p(\alpha x) J_p(\beta x) dx = \begin{cases} \frac{\alpha x J_{p+1}(\alpha x) J_p(\beta x) - \beta x J_p(\alpha x) J_{p+1}(\beta x)}{\alpha^2 - \beta^2}, & \text{for} \alpha \neq \beta \\ \frac{x^2}{2}[(J_p(\alpha x))^2 - J_{p-1}(\alpha x) J_{p+1}(\alpha x)], & \text{for } \alpha = \beta. \end{cases} \tag{3.9}$$

Thus υ becomes

$$\upsilon = \begin{cases} \dfrac{\pi c}{2i(k^2\epsilon_r - k_l^2)} \displaystyle\sum_{n=-\infty}^{\infty} W_{l,n}^{j,m}[k\sqrt{\epsilon_r} J_{n+1}(k\sqrt{\epsilon_r} c) J_n(k_l c) - k_l J_n(k\sqrt{\epsilon_r} c) J_{n+1}(k_l c)]\delta(m-n') \\ \text{for} k_l \neq k\sqrt{\epsilon_r} \\ \dfrac{\pi c^2}{4i} \displaystyle\sum_{n=-\infty}^{\infty} W_{l,n}^{j,m}[(J_n(\sqrt{\epsilon_r} c))^2 - J_{n-1}(k\sqrt{\epsilon_r} c) J_{n+1}(k\sqrt{\epsilon_r} c)]\delta(m-n') \\ \text{for } k_l = k\sqrt{\epsilon_r} \end{cases} \tag{3.10}$$

so Eq. 3.4 becomes as

$$\widetilde{E}(\mathbf{r}) - E(\mathbf{r}) = \sum_{j=1}^{L} \sum_{m=-\infty}^{\infty} H_m^{(1)}(kr_j) e^{im\theta_j} \sum_{l=1}^{L} \sum_{n=-\infty}^{\infty} W_{l,n}^{j,m} q_n^l \tag{3.11}$$

in which

$$q_n^l = \begin{cases} -\frac{\pi c}{2i} \widetilde{C}_n^l [k\sqrt{\epsilon_r} J_{n+1}(k\sqrt{\epsilon_r} c) J_n(k_l c) - k_l J_n(k\sqrt{\epsilon_r} c) J_{n+1}(k_l c)], & \text{for } k_l \neq k\sqrt{\epsilon_r} \\ \frac{\pi c^2 (k_l^2 - k^2\epsilon_r)}{4i} \widetilde{C}_n^l [(J_n(k\sqrt{\epsilon_r} c))^2 - J_{n-1}(k\sqrt{\epsilon_r} c) J_{n+1}(k\sqrt{\epsilon_r} c)], & \text{for } k_l = k\sqrt{\epsilon_r} \end{cases} \tag{3.12}$$

and it can be simplified as

$$q_n^l = \begin{cases} -\frac{\pi c}{2i}\widetilde{C}_n^l[k\sqrt{\epsilon_r}J_{n+1}(k\sqrt{\epsilon_r}c)J_n(k_l c) - k_l J_n(k\sqrt{\epsilon_r}c)J_{n+1}(k_l c)], & \text{for } k_l \neq k\sqrt{\epsilon_r} \\ 0, & \text{for } k_l = k\sqrt{\epsilon_r} \end{cases} \tag{3.13}$$

which means that, if the l-th rod is missing, q_n^l is non-zero, and zero otherwise. Denoting that

$$b_m^j = \sum_{l=1}^{L}\sum_{n=-\infty}^{\infty} W_{l,n}^{j,m} q_n^l, \tag{3.14}$$

then one can get

$$\widetilde{E}(\mathbf{r}) - E(\mathbf{r}) = \sum_{j=1}^{L}\sum_{n=-\infty}^{\infty} b_m^j H_m^{(1)}(kr_j)e^{im\theta_j} \tag{3.15}$$

By comparing the expression of $\widetilde{E}_y(\mathbf{r}) - E_y(\mathbf{r})$ in Eq. 3.15 with the one of the Green function in Eq. 3.2, and comparing the expression of B_m^j in Eq. 2.19 with the one of b_m^j in Eq. 3.14, one interesting fact observed is that the calculation approach of $\widetilde{E}_y(\mathbf{r}) - E_y(\mathbf{r})$ is similar with the calculation of the Green function, but changing $Q_n^l = \frac{1}{4i}J_n(k\sqrt{\epsilon_r}r_l')e^{-in\theta_l'}$ to q_n^l. As Q_n^l are coefficients of field scattered by interior line source, q_n^l can be interpreted as those of the field scattered by cylindrical source.

Considering the general situation of a receiver array with N_r elements and a source array with N_s elements, for the υ-th source, values of $E_y^d(\mathbf{r})$ collected by the receiver array are composed of a column vector $g_\upsilon = [E_y^d(\mathbf{r}^1), E_y^d(\mathbf{r}^2), ..., E_y^d(\mathbf{r}^{N_r})]^T$ with dimension N_r, $\upsilon = 1, 2, .., N_s$, $\mathbf{r}^n$ position of the n-th receiver element, the subscript T being transpose operator, so Eq. 3.15 becomes as

$$g_\upsilon = \mathbf{H}\mathbf{b}_\upsilon \tag{3.16}$$

where $H = \begin{bmatrix} H_{-M}^{(1)}(kr_1^1)e^{i(-M)\theta_1^1} & H_{-M+1}^{(1)}(kr_1^1)e^{i(-M+1)\theta_1^1} & \cdots & H_M^{(1)}(kr_L^1)e^{i(M)\theta_L^1} \\ H_{-M}^{(1)}(kr_1^2)e^{i(-M)\theta_1^2} & H_{-M+1}^{(1)}(kr_1^2)e^{i(-M+1)\theta_1^2} & \cdots & H_M^{(1)}(kr_L^2)e^{i(M)\theta_L^2} \\ \vdots & \vdots & \ddots & \vdots \\ H_{-M}^{(1)}(kr_1^{N_r})e^{i(-M)\theta_1^{N_r}} & H_{-M+1}^{(1)}(kr_1^{N_r})e^{i(-M+1)\theta_1^{N_r}} & \cdots & H_M^{(1)}(kr_L^{N_r})e^{i(M)\theta_L^{N_r}} \end{bmatrix}$,

within which (r_l^n, θ_l^n) are the polar coordinates of $\mathbf{r}^n$ in the local coordinate system with respect to the l-th rod, so

$$\mathbf{b}_\upsilon = \mathbf{W}\mathbf{q}_\upsilon, \tag{3.17}$$

where $\mathbf{q}_\upsilon = [\mathbf{q}^1, \mathbf{q}^2, ..., \mathbf{q}^L]^T$, q^l being coefficient vector associated with the l-th rod, and $q^l = [q_{-M}^l, q_{-M+1}^l, ..., q_M^l]$. As the expression HW is invariant with the sources, taking different g_υ as columns, the data matrix Y is defined as $\mathbf{Y} = [\mathbf{g_1}, \mathbf{g_2}, ..., \mathbf{g_{N_s}}]$, and denoting

$\mathbf{Q} = [\mathbf{q_1}, \mathbf{q_2}, ..., \mathbf{q_{N_s}}]$,

$$\mathbf{Y} = \mathbf{HWQ}, \tag{3.18}$$

Let us define $\mathbf{G} = \mathbf{HW}$, thus, the equation in matrix form linking collected data and locations of missing rods reads as

$$\mathbf{Y} = \mathbf{GQ}, \tag{3.19}$$

without noise corruption. Considering additive noise, assumed to be Gaussian random herein.

$$\mathbf{Y} = \mathbf{GQ} + \mathbf{N}. \tag{3.20}$$

The goal is to get the information about indexes of missing rods from the multi-static response matrix. If there is only a single emitting source, $\mathbf{Q}$ becomes a column vector. If the l-th rod is missing, the corresponding element in $\mathbf{Q}$ is non-zero. In the general situation, only few rods are missing, so most elements in $\mathbf{Q}$ are zero, so $\mathbf{Q}$ is sparse. The imaging performance is expected to be better because there is sparsity prior information available about the structure.

With an incident field of frequency low enough, when the radius of the rod $c < (0.31\lambda/(2\pi\sqrt{\epsilon}))$, $(k\sqrt{\epsilon_r}c)^{1/3} + k\sqrt{\epsilon_r}c$ can be smaller than 1 so that $M = \text{int}((k\sqrt{\epsilon_r}c)^{1/3} + k\sqrt{\epsilon_r}c)$ is reduced to 0 without a security factor [31]; consequently, $\mathbf{G} = \mathbf{G}^0$, $\mathbf{Q} = \mathbf{Q}^0$.

Since sparsity can be accurately evaluated via a l_0 norm which counts the number of non-zero elements, the optimal problem becomes

$$\mathbf{Q} = \arg\min \|\mathbf{Q}\|_0, s.t. \|\mathbf{Y} - \mathbf{GQ}\|_2^2 \leq \tau^2, \tag{3.21}$$

where the parameter τ is decided by the noise variance.

Solving such an equation would call for exhaustive enumeration of all possible locations of non-zero entries in $\mathbf{Q}$, which is NP hard. However, when there are sufficient collected data, ℓ_p norm can provide a good approximation of ℓ_0 norm, the definition of ℓ_p being

$$\|\mathbf{Q}\|_p^p = \sum_{i=1}^{L} |Q_i|^p, 0 < p \leq 1, \tag{3.22}$$

where one uses $p = 0.8$ after numerical trial, so the optimization problem can be rewritten as

$$\mathbf{Q} = \arg\min \|\mathbf{Q}\|_p, s.t. \|\mathbf{Y} - \mathbf{GQ}\|_2^2 \leq \tau^2, \tag{3.23}$$

and expressed using the Lagrangian form

$$\mathbf{Q} = \arg\min J(\mathbf{Q}) = \|\mathbf{Y} - \mathbf{G}\mathbf{Q}\|_2^2 + \gamma\|\mathbf{Q}\|_p, \tag{3.24}$$

where the parameter γ realizes a trade-off between sparsity and quality of the data fit. If γ increases, more weight is put on the sparsity. Using gradient-descent and L-curve methods [32], [33], one can solve the optimization problem. When $\nabla J(\mathbf{Q}) = 0$,

$$\nabla J(\mathbf{Q}) = 2\mathbf{G}^H\mathbf{G}\mathbf{Q} - 2\mathbf{G}^H\mathbf{Y} + 2\beta\Pi(\mathbf{Q})\mathbf{Q} = 0, \tag{3.25}$$

where H is transpose operation and $\beta = p\gamma/2$.

An algorithm is developed based on the methodology sketched above which is shown in the flow chart below. In it, ξ is the threshold to stop the whole algorithm, $\xi = 10^{-8}$, and δ should be small enough not to affect the behavior of the solution, e.g., $\delta = 10^{-3}\max\{Q_i\}$. Based on this algorithm, $\mathbf{Q}^{(k)}$ is the solution at the k-th iteration, the regularization parameter β being updated at each iteration to ensure the trade-off effectively.

Algorithm 1 Optimization algorithm of locating missing rods

1: Initialization: $\mathbf{Q}^{(0)} = 0$ and $k = 0$;
2: Update $\Pi(\mathbf{Q}^{(k)})$ using gradient-descent method, herein $\Pi(\mathbf{Q}) = \mathrm{diag}\{|Q_i^2 + \delta|^{(p/2-1)}\}$;
3: Select optimal parameter using L-curve method;
4: $\mathbf{Q}^{(k+1)} = \left[\mathbf{G}^H\mathbf{G} + \beta^{(k)}\Pi(\mathbf{Q}^{(k)})\right]^{-1}\mathbf{G}^H\mathbf{Y}$;
5: $k = k + 1$;
6: if $\|\mathbf{Q}^{(k)} - \mathbf{Q}^{(k-1)}\|_2 < \xi$, stop, otherwise, repeat the steps from 2 to 6;

3.1.1 Results of sparsity-constrained method

The results shown in Fig. 3.3 correspond to three different cases when SNR = 30dB: missing one rod, missing two rods, missing three rods in the micro-structure, for two rod distributions: 36 rods, 64 rods. Super-localization appears well realized by using the sparsity information.

Some other tests for different values of d and c are also carried out. Fig. 3.4 shows different radii of rod, Fig. 3.5 shows the results of different distances between rods. It turns out that the proposed method still works.

Different ϵ_r values are also used to guarantee the robustness of the sparsity-constrained method. As shown in Fig. 3.6, when the ϵ of rod is 7.5, the sparsity-constrained method succeed in locating the missing rod for the 36 rods case with a higher value of M, while

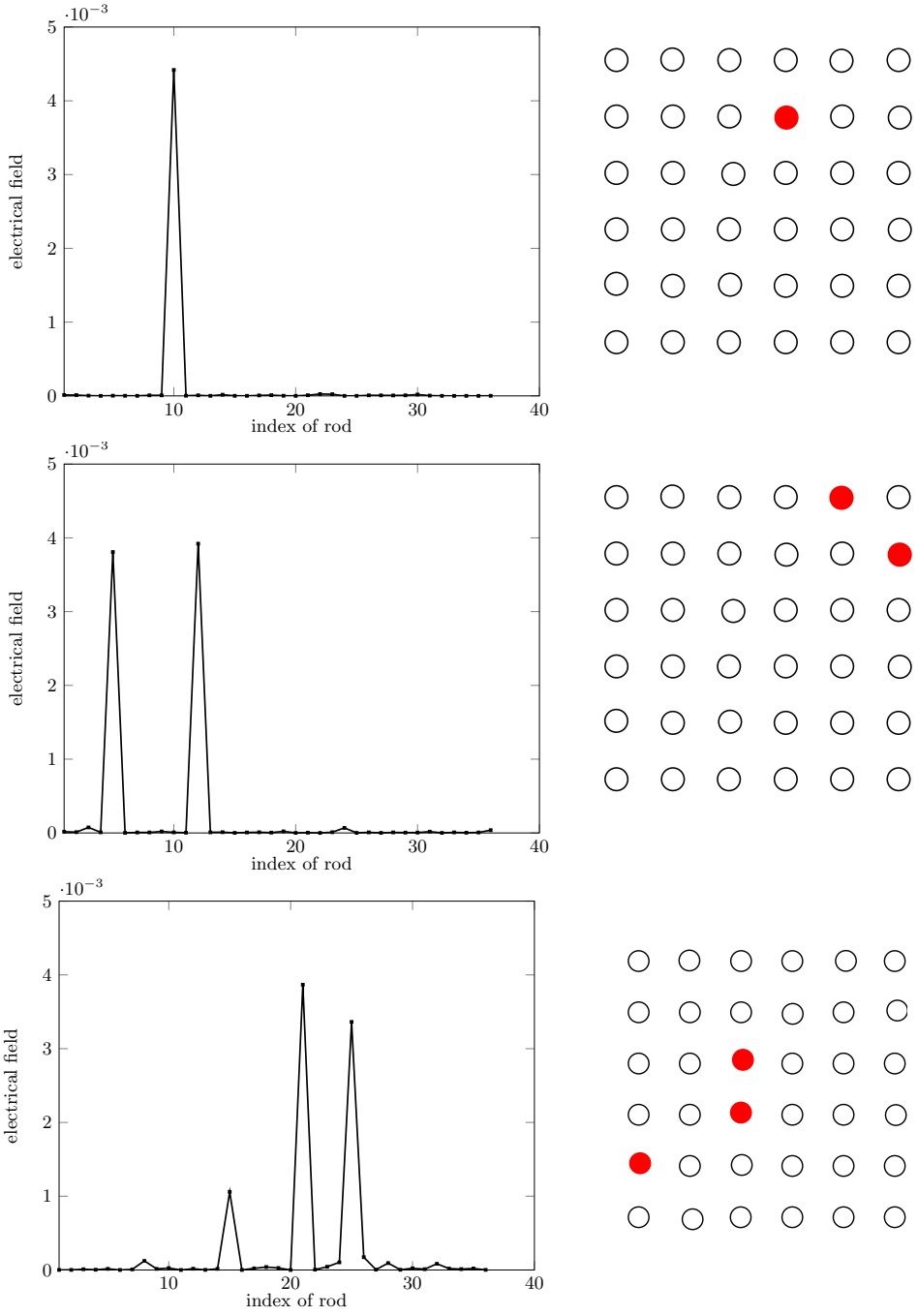

Figure 3.2: Results of localization for three cases: one missing rod, two missing rods, three missing rods, finding missing rods in the micro-structure, here indexed from 1 to 36, left to right, top to bottom, $\epsilon = 2.5$.

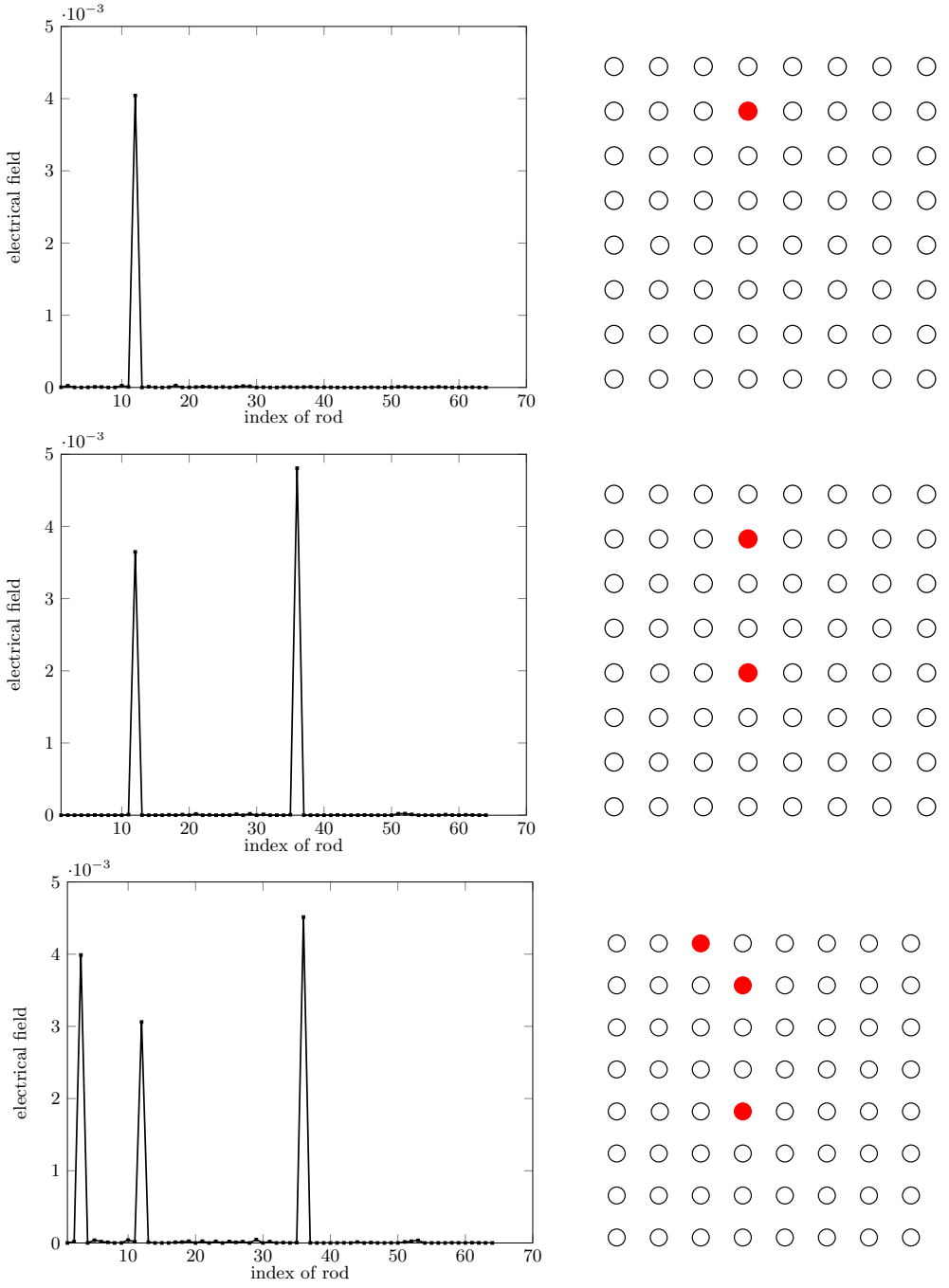

Figure 3.3: Results of localization for three cases: one missing rod, two missing rods, three missing rods, finding missing rods in the micro-structure, here indexed from 1 to 64, left to right, top to bottom, $\epsilon = 2.5$.

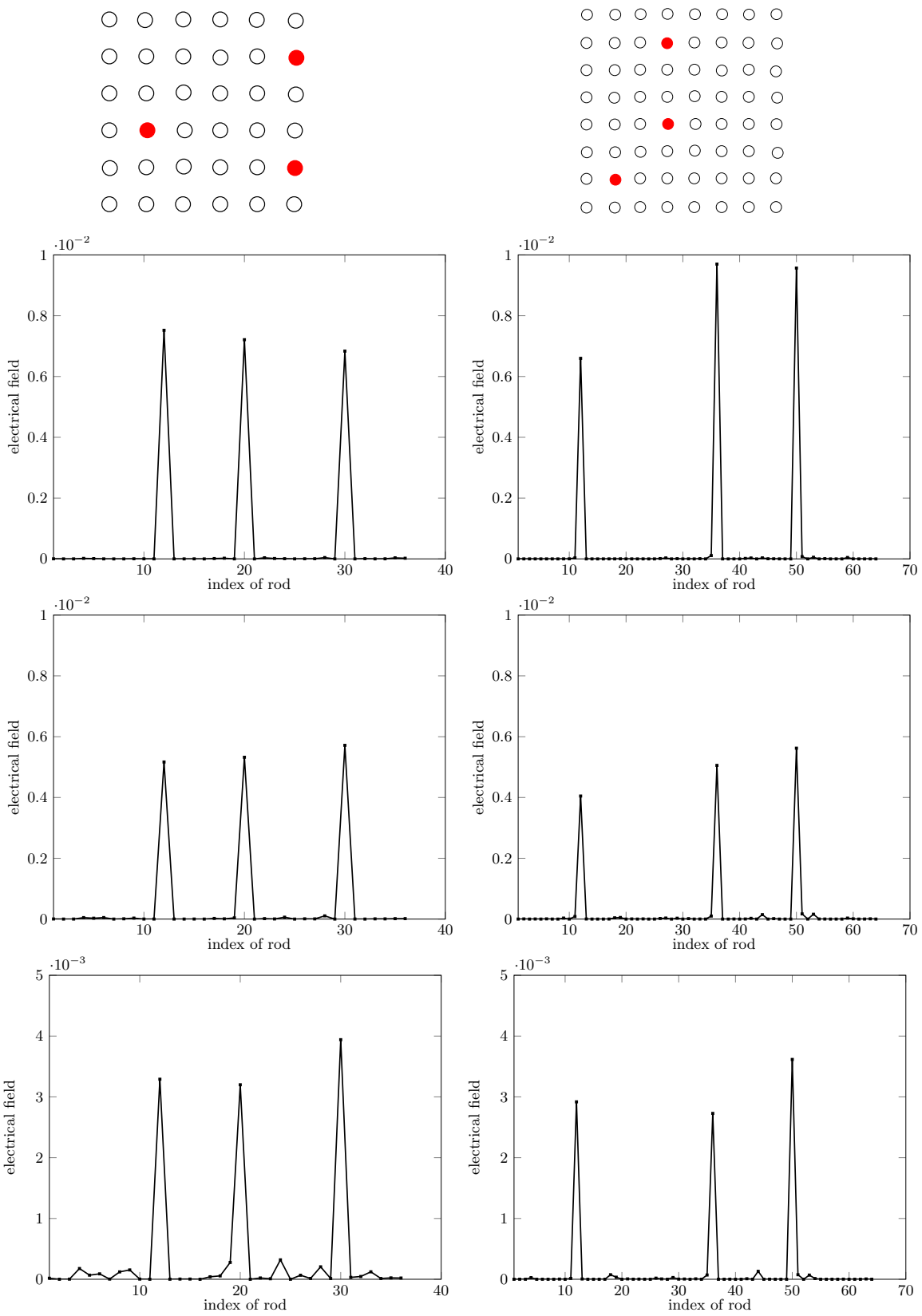

Figure 3.4: left column is the 36-rod case, right column is the 64-rod case, from top to bottom: the radius of the rod c equals $\lambda/10$,$\lambda/12$,$\lambda/14$, the distance between rods d is $\lambda/4$.

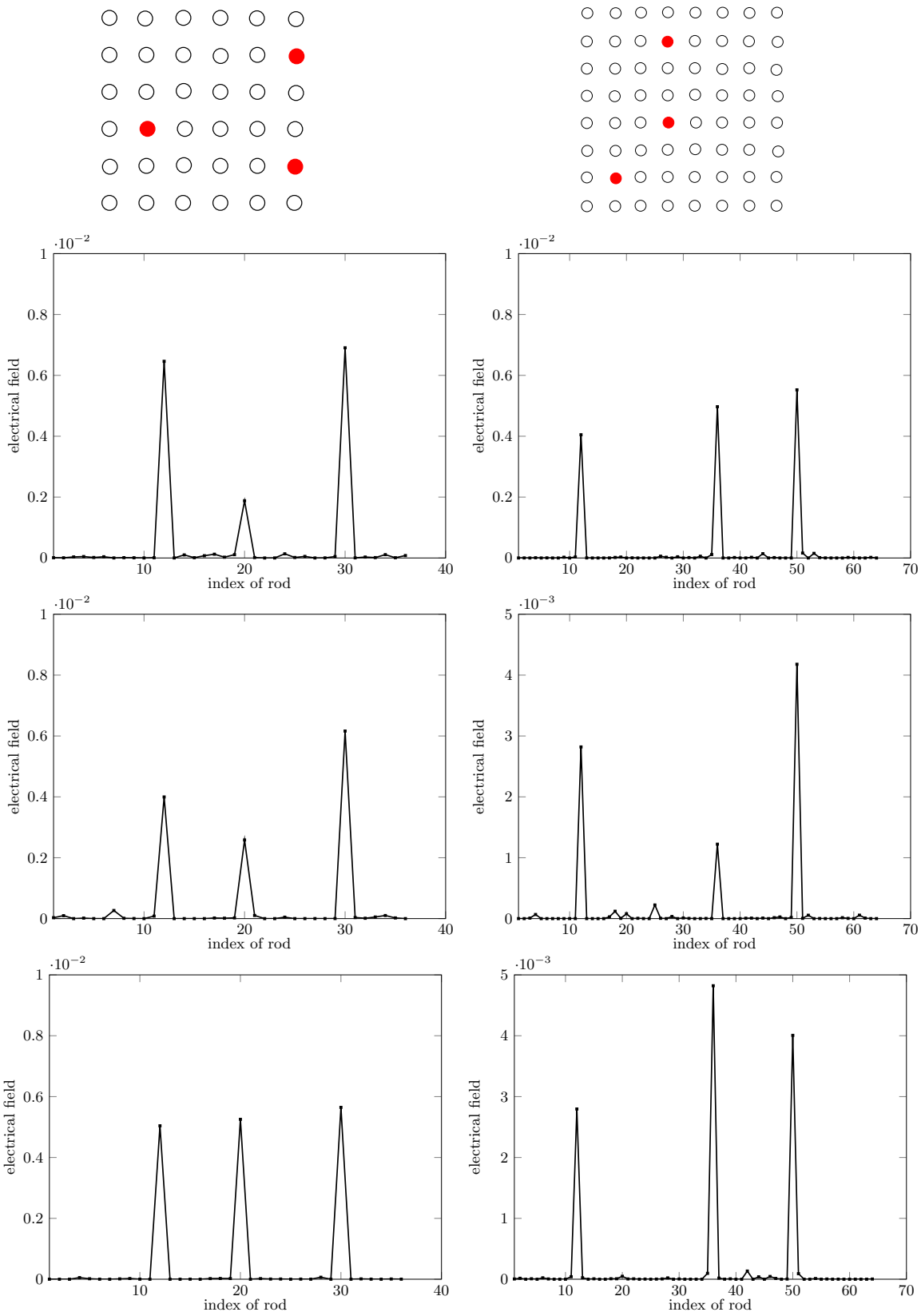

Figure 3.5: left column is the 36-rod case, right column is the 64-rod case, from top to bottom: the distance between rods d equals $\lambda/2$,$\lambda/4$,$\lambda/6$, the radius of rods c is $\lambda/12$.

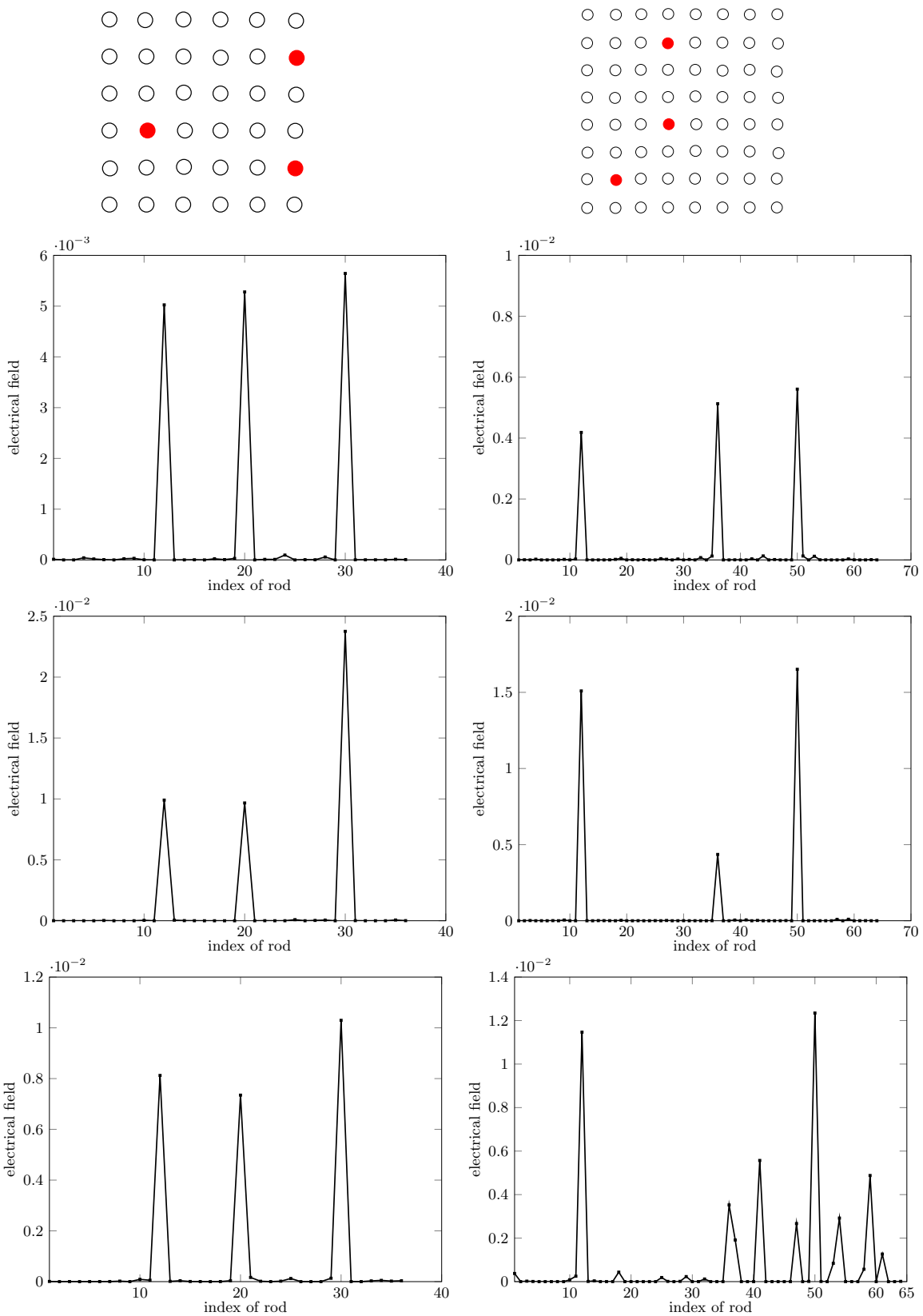

Figure 3.6: left column is the 36-rod case, right column is the 64-rod case, from top to bottom: $\epsilon = 2.5$, 5, 7.5.

it does not succeed for the 64 rods case even with a higher value of M, which shows that the proposed method still has limitations.

3.2 Contrast source inversion

One of the most widely used methods to tackle an inverse scattering problem is the contrast source inversion (CSI) method [34]. Based on the modified gradient method and the source-type integral equation method, the CSI method is proposed, where the unknown contrast sources and the unknown contrast are updated by an iterative minimization of a cost functional. The modified gradient method (MGM) is based on the field-type equations and treat both contrast and electric field as independent unknowns, which are simultaneously updated at each iteration, and the objective function is composed of two types of normalized mismatches, one for the data equation and the other for the state equation. The source-type integral method is also based on the source-type integral equation and it treats the contrast and the contrast current as independent unknowns. As a consequence, with the CSI method, the necessity of a full solution of the forward problem at each iteration is avoided by the simultaneous update of the field and of the contrast.

Since the objects tackled in this research is either normal rods or missing rods, so it can be defined as a binary problem; there already exist analysis of inverse scattering for binary objects, the modified gradient methods (MGM) [35] is the case as pioneering investigation, and the 3-D eddy-current evaluation [36] in a CSI framework. The material properties are also coded on a binary basis in obstacles reconstruction by controlled evolution of level sets as appearing under various guises, refer to, e.g. [37], [38], [39]. For the sake of completeness, the binary-specialized CSI method is described thereafter.

Binary-specialized CSI method

The CSI method is based on source-type integral equations as

$$J_p(\mathbf{r}) = \chi(\mathbf{r}) \left[E_p^{inc}(\mathbf{r}) + G_d(\mathbf{J}_p) \right], \mathbf{r} \in D, \tag{3.26}$$

$$E_p^{sca}(\mathbf{r}) = G_s(\mathbf{J}_p), \mathbf{r} \in S, \tag{3.27}$$

where the contrast source $J_p(\mathbf{r})$ is regarded as an independent parameter.

For the binary case, providing us with a binary-specialized CSI, the contrast value can be set as $\chi = \chi_m f(\tau)$, equating χ_m to $(\epsilon_r - \epsilon_b)/\epsilon_b$, ϵ_r relative permittivity of rods, ϵ_b the one of the background (here valued to 1), and $f(\tau)$ equals $1/(1 + e^{-\frac{\tau}{\theta}})$. The real and strictly positive parameter θ is a tuning parameter which is controlling the slope of $f(\tau)$ between 0 and 1 and it plays the role of a regularization parameter which could be

progressively reduced in magnitude whether necessary. The cost function takes a linear combination of normalized mismatches in the data equation and in the state equation as

$$\begin{aligned} L(\mathbf{J}_1,\ldots,\mathbf{J}_{N_i},\chi,\beta) &= \frac{\sum_{p=1}^{N_i} \parallel \mathbf{E}_p^{sca} - G_s(\mathbf{J}_p) \parallel^2}{\sum_{p=1}^{N_i} \parallel \mathbf{E}_p^{sca} \parallel^2} \\ &+ \beta \frac{\sum_{p=1}^{N_i} \parallel \chi_m f(\tau)\mathbf{E}_p^{inc} + \chi_m f(\tau) G_d(\mathbf{J}_p) - \mathbf{J}_p \parallel^2}{\sum_{p=1}^{N_i} \parallel \chi_m f(\tau)\mathbf{E}_p^{inc} \parallel^2}. \end{aligned} \tag{3.28}$$

where both $\chi_m f(\tau)$ and $\mathbf{E}_p^{inc}$ are vectors, and where the $\chi_m f(\tau)\mathbf{E}_p^{inc}$ means multiplying corresponding elements in these two vectors, same hereafter. From now, one simply sets $\beta = 1$ so as to give the same weight to the two types of errors.

The cost function is minimized by alternately updating contrast source and contrast parameter. A conjugate-gradient method with Polak-Ribière direction is used to optimize the parameters of interest. The optimization method is the same as in [34]. There is no need to solve the forward problem and the optimization procedure becomes more efficient this way. The initial guess for τ is zero, and the initial guess for $\mathbf{J}_p$ is calculated by standard back-propagation as

$$\mathbf{J}_p^{bp} = \frac{\parallel G_s^*(\mathbf{E}_p^{sca}) \parallel^2}{\parallel G_s(G_s^*(\mathbf{E}_p^{sca})) \parallel^2} G_s^*(\mathbf{E}_p^{sca}), \tag{3.29}$$

where $\mathbf{E}_p^{tot} = \mathbf{E}_p^{inc} + G_d(\mathbf{J}_p^{bp})$, $\overline{\mathbf{E}}_p^{tot}$ is the conjugate of $\mathbf{E}_p^{tot}$ and $G_s^*(\cdot)$ is the adjoint operator of $G_s(\cdot)$.

The problem is solved iteratively. At the nth iteration, the object function with respect to $\mathbf{J}$ is written as

$$L(\mathbf{J}_1,\ldots,\mathbf{J}_{N_i}) = \frac{\sum_{p=1}^{N_i} \parallel \mathbf{E}_p^{sca} - G_s(\mathbf{J}_p) \parallel^2}{\eta_s} + \frac{\sum_{p=1}^{N_i} \parallel \chi\mathbf{E}_p^{inc} + \chi G_d(\mathbf{J}_p) - \mathbf{J}_p \parallel^2}{\eta_{d,n-1}}, \tag{3.30}$$

where the two denominators read as $\eta_s = \sum_{p=1}^{N_i} \parallel \mathbf{E}_p^{sca} \parallel^2$ and $\eta_{d,n-1} = \sum_{p=1}^{N_i} \parallel \chi_{n-1}\mathbf{E}_p^{inc} \parallel^2$. One now defines the data error and the object error to be

$$\mathbf{err\_d}_{p,n} = \mathbf{E}_p^{sca} - G_s\mathbf{J}_{p,n-1}, \mathbf{err\_o}_{p,n} = \chi_n\mathbf{E}_{p,n-1}^{tot} - \mathbf{J}_{p,n-1}, \tag{3.31}$$

where $\mathbf{E}_{p,n-1}^{tot} = \mathbf{E}_p^{inc} + G_d\mathbf{J}_{p,n-1}$. The gradient (Fréchet derivative) $\mathbf{g}_{p,n}^J$ evaluated at $\mathbf{J}_{p,n-1}$ and χ_{n-1} is

$$\mathbf{g}_{p,n}^J = -\frac{G_s^*\mathbf{err\_d}_{p,n}}{\eta_s} - \frac{\mathbf{err\_o}_{p,n} - G_d^*\left(\overline{\chi}_{n-1}\mathbf{err\_o}_{p,n}\right)}{\eta_{d,n-1}}. \tag{3.32}$$

The Polak-Ribière conjugate gradient search direction as

$$\begin{aligned}\mathbf{d}_{p,0}^{J} &= -\,\mathbf{g}_{p,0}^{J},\\ \mathbf{d}_{p,n}^{J} &= -\,\mathbf{g}_{p,n}^{J} + \frac{Re\langle \mathbf{g}_{p,n}^{J}, \mathbf{g}_{p,n}^{J} - \mathbf{g}_{p,n-1}^{J}\rangle}{\langle \mathbf{g}_{p,n-1}^{J}, \mathbf{g}_{p,n-1}^{J}\rangle}\mathbf{d}_{p,n-1}^{J},\end{aligned} \tag{3.33}$$

and the step size along this search direction reads as

$$\alpha_{p,n}^{J} = \frac{-\langle \mathbf{g}_{p,n}^{J}, \mathbf{d}_{p,n}^{J}\rangle}{\dfrac{\parallel G_s \mathbf{d}_{p,n}^{J} \parallel^2}{\eta_s} + \dfrac{\parallel \mathbf{d}_{p,n}^{J} - \chi_{n-1} G_d \mathbf{d}_{p,n}^{J} \parallel^2}{\eta_{d,n-1}}}. \tag{3.34}$$

Then, the contrast source is calculated according to $\mathbf{J}_{p,n} = \mathbf{J}_{p,n-1} + \alpha_{p,n}^{J}\mathbf{d}_{p,n}^{J}$. The normalization parameter $\eta_{d,n-1}$ is considered as constant during the update of τ. The object function with respect to the contrast parameter τ is

$$L(\tau) = \frac{\sum_{p=1}^{N_i} \parallel \chi_m f(\tau)\mathbf{E}_{p,n}^{tot} - \mathbf{J}_{p,n} \parallel^2}{\eta_{d,n-1}}, \tag{3.35}$$

and its gradient with respect to τ_n is

$$\mathbf{g}_n^{\tau} = \sum_{p=1}^{N_i} \frac{\chi_m Re\langle \mathbf{E}_{p,n}^{tot}, \chi_m \mathbf{E}_{p,n}^{tot} f(\tau_{n-1}) - \mathbf{J}_{p,n}\rangle}{\eta_{d,n-1}} \cdot \frac{f(\tau_{n-1})(1 - f(\tau_{n-1}))}{\theta}, \tag{3.36}$$

where χ_m is real-valued in the case under investigation. The search directions are

$$\mathbf{d}_0^{\tau} = -\,\mathbf{g}_0^{\tau}, \tag{3.37}$$

$$\mathbf{d}_n^{\tau} = -\,\mathbf{g}_n^{\tau} + \frac{Re\langle \mathbf{g}_n^{\tau}, \mathbf{g}_n^{\tau} - \mathbf{g}_{n-1}^{\tau}\rangle}{\langle \mathbf{g}_{n-1}^{\tau}, \mathbf{g}_{n-1}^{\tau}\rangle}\mathbf{d}_{n-1}^{\tau}. \tag{3.38}$$

The contrast parameter is updated as

$$\tau_n = \tau_{n-1} + \alpha_n \mathbf{d}_n^{\tau}, \tag{3.39}$$

wherein the value of α is calculated using line search. As a consequence, the value of τ is updated when one gets the value of α, then $\mathbf{J}$ and τ are iteratively updated.

3.2.1 Results of binary-specialized contrast source inversion

In the present section, the binary-specialized CSI is tested for different cases of interest, wherein the radius r and the distance d that characterize the micro-structure are kept constant, as $\lambda/12$ and $\lambda/4$ respectively, λ wavelength in air. The size of the region of interest (the ROI) is set at $1.75\lambda \times 1.75\lambda$, and is discretized into 60×60 cells in the direct problem, and into 50×50 cells in the inverse problem. 36 receivers and 36 sources are placed in a regular fashion on a circle of radius 7.2 λ. The single operating frequency is in practice fixed at 3 GHz ($\lambda = 0.1$ m). The collected fields are used to reconstruct the contrast map of the damaged micro-structure by the binary-specialized CSI method. The micro-structure is involving 4×4 or 6×6 rods.

Two cases are considered: one with no prior information on the positions of the rods, the other with that prior position information, the signal to noise ratios being taken as 30dB. From Fig.3.7, without the prior position information, the binary-specialized CSI method cannot realize the reconstruction of the contrast map for both 16 and 36 rods, the distance between two rods d equals $\lambda/4$, which is smaller than $\lambda/2$, may lead to this failure. From Fig. 3.8 and Fig. 3.9, one concludes that the binary-specialized CSI can realize the reconstruction with the prior position information.

Though no systematic studies of divergence of CSI methods when dielectric contrasts get higher and higher seem to exist, examples in [40] appear fitted to rather low contrasts, while in [41], now using subspace-based optimization methods, expected to be more effective, the same holds true, high contrast domains being not retrieved (some interesting yet limited improvement is observed if the coupling equation is transformed, this type of transform being beyond the scope of the present work).

The binary-specialized CSI method as considered here failed the reconstruction of the contrast map when the contrast value is 3 or above because of high no-linearity. In short, it works well for some range of contrasts, but has limitations, so one turns to the convolutional neural networks to devise another solution for this problem.

3.3 CSI for reconstruction of random contrast distribution

The contents described earlier in this chapter are about the binary case of the structure. While, the contrast of rods can be different, so, deleting the binary prior, the traditional CSI method is used to reconstruct the distribution of ROI whose contrast value is random.

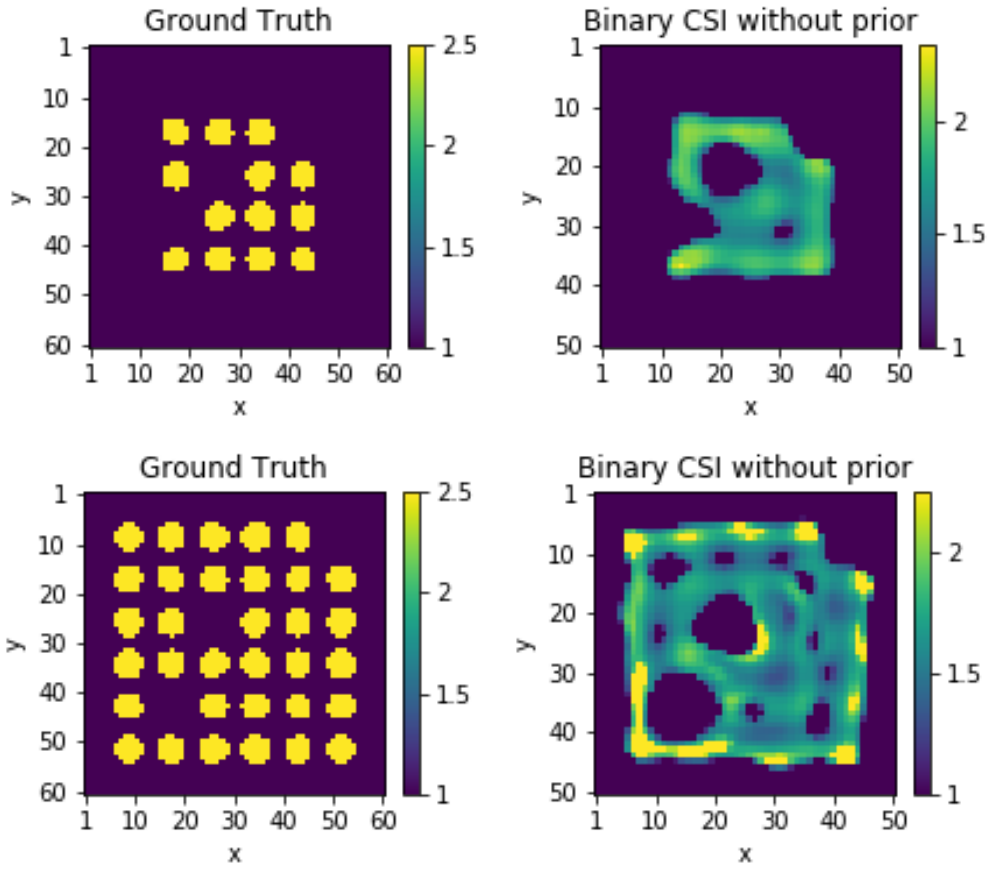

Figure 3.7: Results of the binary-specialized CSI without prior position information.

Illustrative results of application of traditional CSI to the micro-structure are shown in Fig. 3.10. About the test, two choices have been made: (i) using the CSI method without any information on the positions of rods, (ii) using the CSI method with information on those. Without prior position information, one cannot really reconstruct the contrast map, while helped by prior positions, it works slightly better but still cannot achieve precise retrieval.

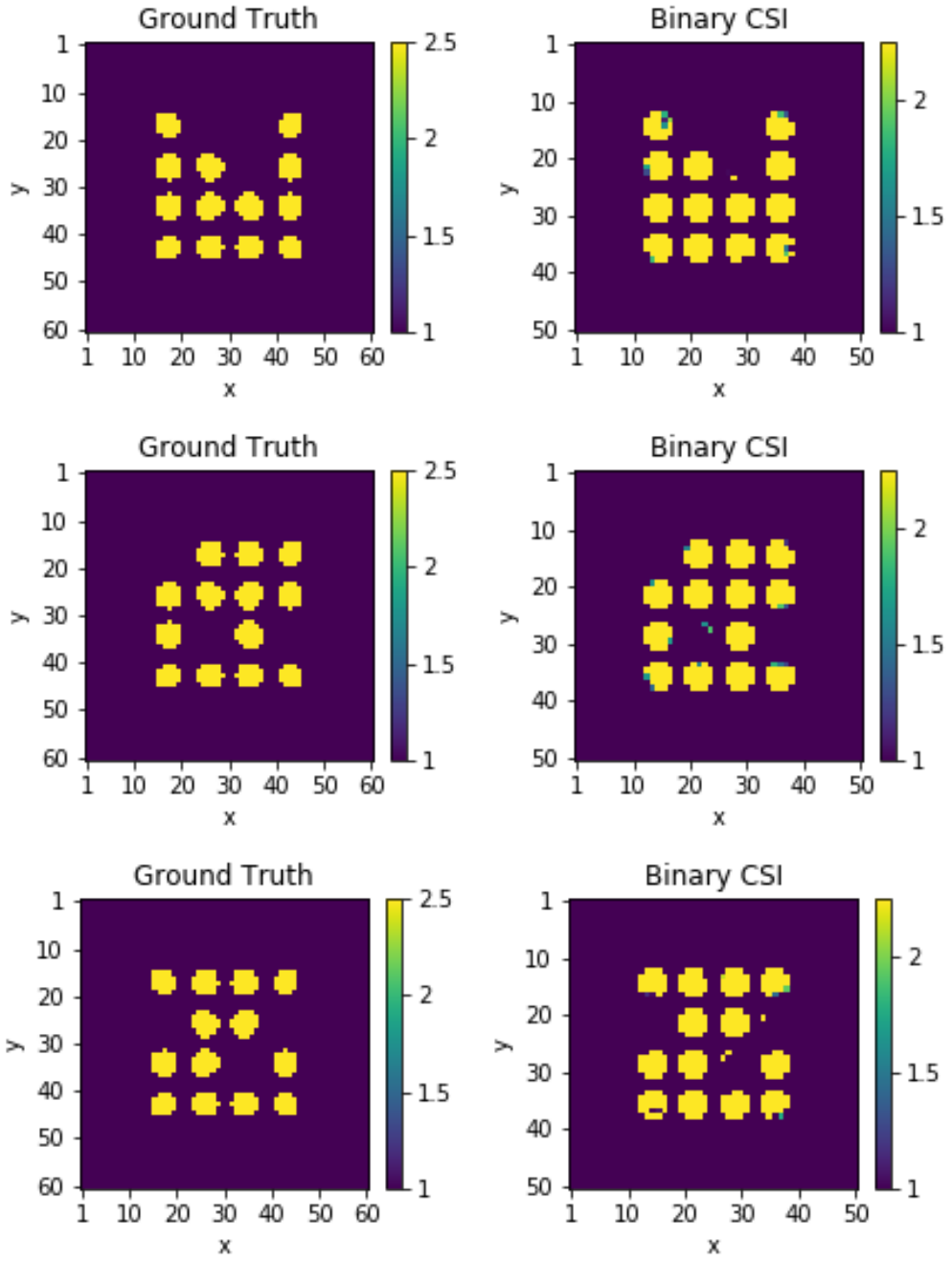

Figure 3.8: Results of the binary-specialized CSI for three examples of damages in the 16 rods case; left column is the ground truth, right column is the binary-specialized CSI result.

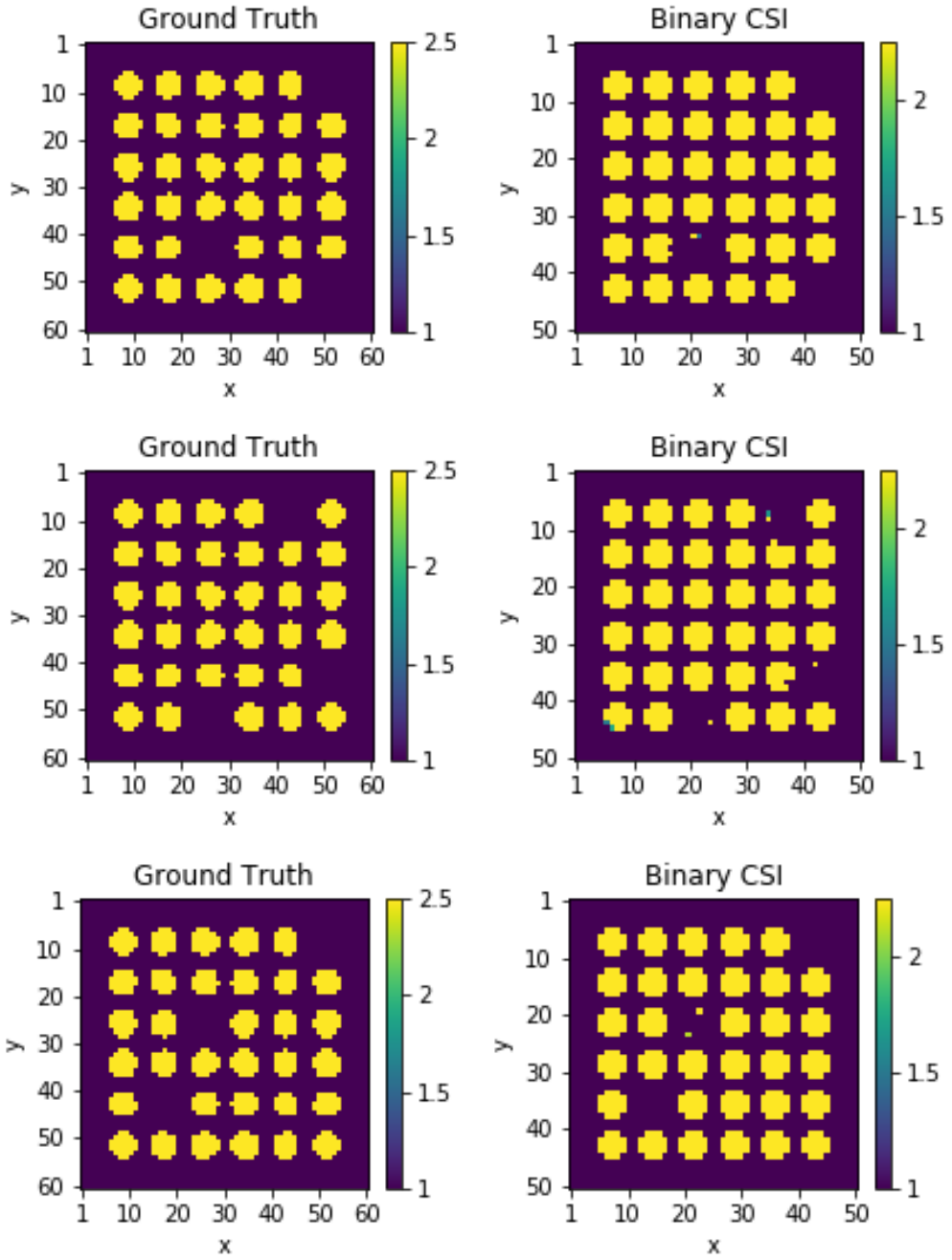

Figure 3.9: Results of the binary-specialized CSI for three examples of damages in the 36 rods case; left column is the ground truth, right column the binary-specialized CSI result.

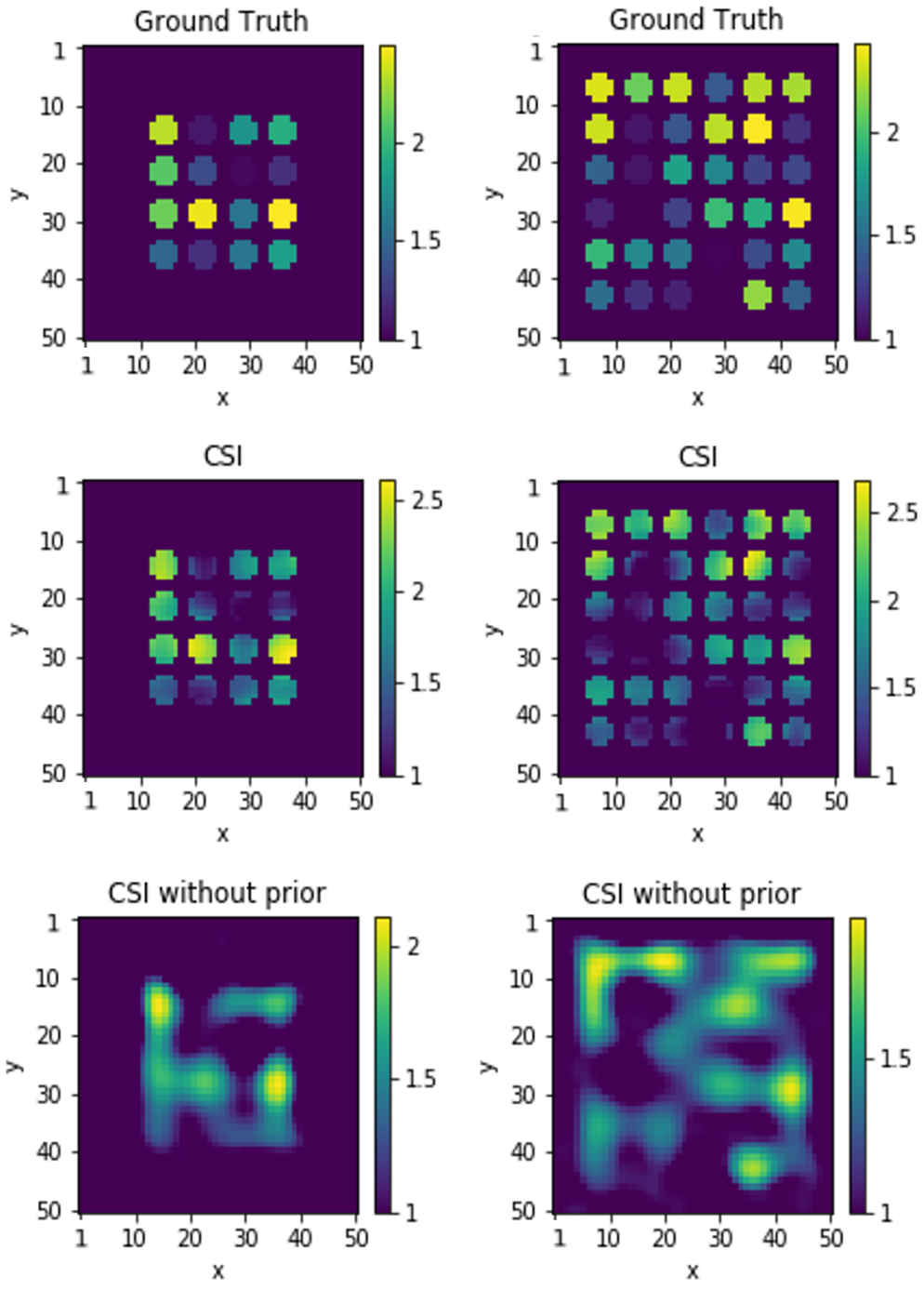

Figure 3.10: Maps provided by CSI. Top to bottom: ground truth, CSI with prior information, CSI without it. Left: 16 rods case, right: 36 rods case.

Chapter 4

Imaging by convolutional neural networks in frequency domain

Inverse scattering problem can be not only solved by traditional objective function approaches but also learning methods. As shown in previous chapter, the traditional objective function needs iterative computation. Neural networks learning as providing powerful tools has achieved several results already in the inverse scattering problem, and the potential mathematical link between deep learning and inverse problem is discussed in some research [26]. In this chapter, the CNN based method is introduced to tackle the inverse scattering problem that one is faced with, and the design of the structure is based on the regression between the collected field and the contrast distribution of the ROI, so it should be considered as a supervised learning.

4.1 CNN architecture

Fig. 4.1 shows the designed architecture. The input of the network is the collected field, the output is the reconstructed ROI. The built network realizes the construction of a map from the scattered field to the distribution of contrast. It is composed of three main components as follows. The first component contains several repeated blocks, each block contains one convolutional layer with kernel size [5, 5], one batch normalization layer, one ReLU function, and one max-pooling layer, which is a typical block in convolutional neural networks. The second component is the fully-connected layer, which combines all the feature information gotten from previous layers. The third component is the deconvolutional layer, which can help retrieve the contrast map. Here the details of each part are introduced:

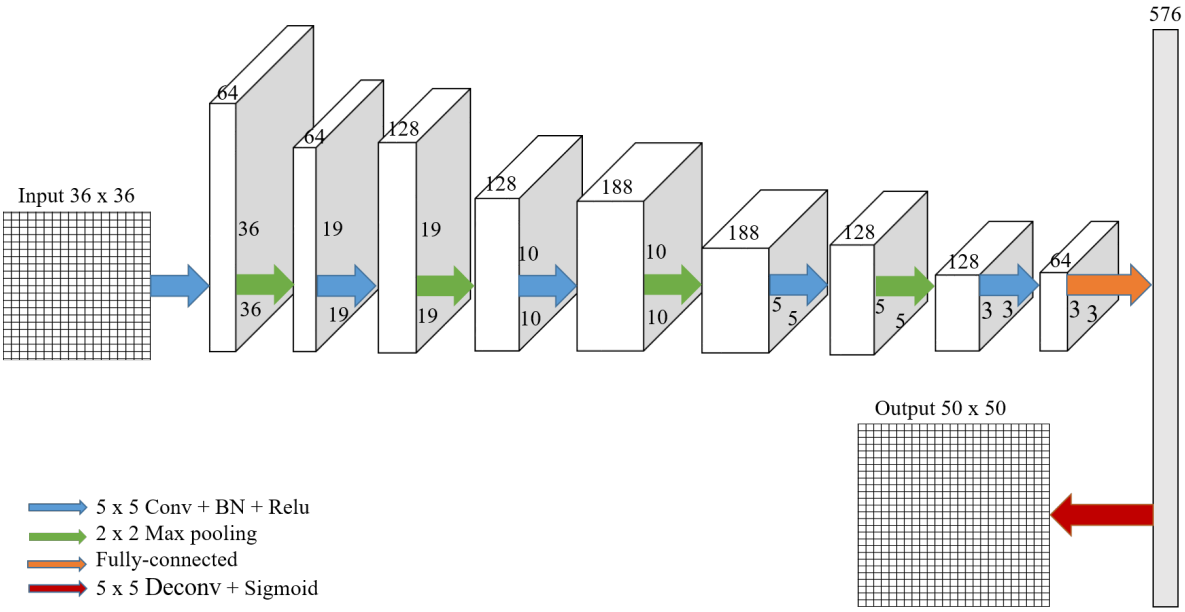

Figure 4.1: CNN architecture

1) The convolutional layer has strong local modelling capabilities with a small number of parameters, and it has the ability to extract local features. The detail of the convolutional layer is shown in Fig 4.2, the convolutional layer uses the kernel of size [5, 5], and pad zeros outside the edges using a stride of 1, so the layer's outputs have the same spatial dimensions as its inputs. Convolutional operation contributes to the learning system from three aspects: sparse interactions, parameter sharing, equivariant representation. Sparse interactions, or called sparse weights, is realized by the fact that the kernel size is much smaller than the size of input, compared with the traditional neural network, which builds the full connection between input and output by matrix multiplication. So, sparse weights can improve the efficiency of the calculation; parameter sharing is the sharing of a set of weights by all neurons within a particular map, which helps to reduce the number of parameters in the whole system and renders the computation more efficient, and the speciality of sharing parameters makes the neural networks to have the property of translation equivariance.

2) ReLU, a non-saturated function, is chosen as activation function in neural networks, written as $g(z) = \max(0, z)$. Applying this function to the output of a linear transformation can produce a non-linear transformation. The ReLU function is composed of two linear parts, it is very close to a linear function, so it contains plenty of properties that help the model to use the optimization method based on gradient. Thus, using the

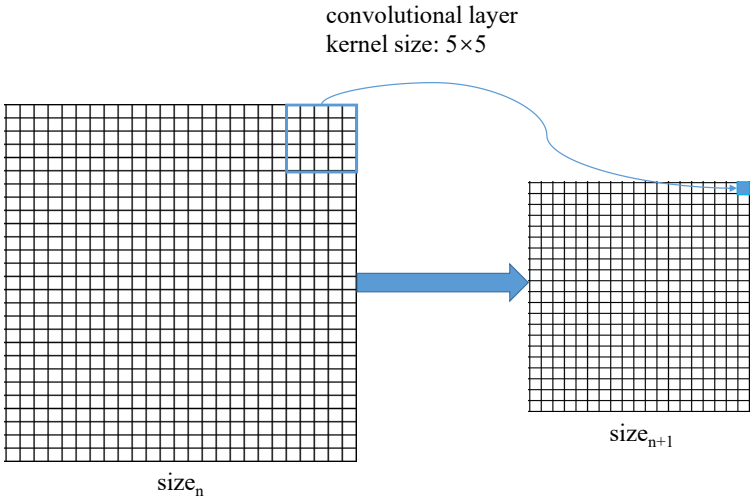

Figure 4.2: convolutional layer

Relu function can avoid vanishing gradients and accelerate the convergence speed. As for the last layer in the structure, the sigmoid function $\delta(z) = \frac{1}{1+e^{-z}}$ is used as activation function, since it can produce results close to either 0, when z has a quite small negative value, or 1, when z has a quite large positive value. The sigmoid function is a saturated function, it is not sensitive to the input except for the value around 0, which makes the method based on gradient descent hard to carry out, so normally it is not used in the hidden layer.

3) The fact that the distribution of each layer's input changes during training, as the parameters of the previous layers change, makes the training procedure difficult, and it slows it down by requiring lower learning rates and careful parameter initialization; this phenomenon is called as internal covariate shift. Batch normalization normalizes input and hidden layers by scaling the activations to alleviate the internal covariate shift [42], as shown in Eq. 4.1, Eq. 4.2, Eq. 4.3, and normalization is a part of the model architecture and performs that said normalization for each training mini-batch. Batch normalization enables us to use much higher learning rates and in a way to be less careful about initialization, which can consequently speed up the learning.

$$\mathbf{H}' = \frac{\mathbf{H} - \upsilon}{\sigma} \tag{4.1}$$

where

$$\upsilon = \frac{1}{m}\sum_i \mathbf{H} \tag{4.2}$$

and

$$\sigma = \sqrt{\delta + \frac{1}{m}\sum_i (\mathbf{H} - \upsilon)_i^2} \tag{4.3}$$

where δ is a quite small value, like 10^{-8} to avoid the situation that gradient of $\sqrt{z}$ is not defined at $z = 0$.

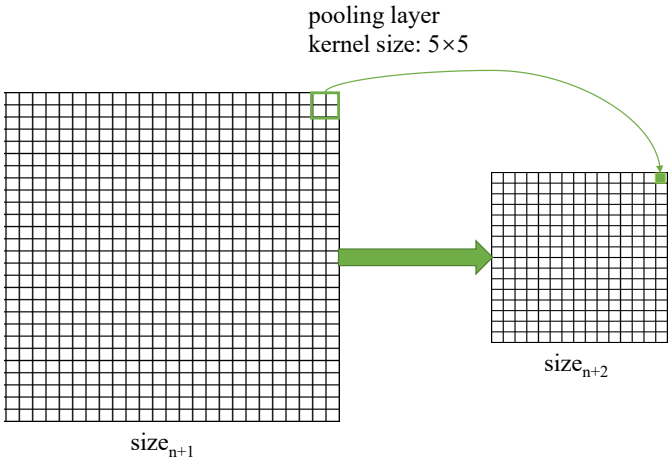

Figure 4.3: max pooling layer

4) Each convolutional layer is followed by a pooling layer; the pooling function uses a global statistical characteristic of the neighbouring outputs of a location instead of the network's output at that position, and the pooling of space contributes to the translation invariance of the representation of input. Max-pooling is a commonly used pooling method, and the invariance property can be extended to different transformation invariance by pooling on the output of convolution which is used for separation parameters. Pooling has important influence on the processing of inputs of different size, since the pooling can change the data dimension, and reduce the computational burden. The detail of max-pooling is shown in Fig. 4.3, the max pooling layer uses the kernel of size

[2, 2], and pads zeros outside the edges using a stride of 2, so the layer's outputs have the half spatial dimensions of its inputs.

4.2 Loss function

The loss function combines the misfit between predictions and the ideal output of the network and a regularization term of the weights. For the binary case, inspired by the idea of binary classification [43], the loss function for logistic regression is employed. The binary reconstruction problem resembles the binary classification, and when the number of classes is equal to 2, cross-entropy can be calculated as

$$\begin{aligned} LOSS = &- \frac{1}{N}\sum_{i=1}^{N} l^i log(h(\hat{\boldsymbol{\epsilon}}_r^i)) + (1-l^i) log(1-h(\hat{\boldsymbol{\epsilon}}_r^i)) \\ &+ \alpha \sum_{j=1}^{P} \mathbf{W}_j^2. \end{aligned} \tag{4.4}$$

within which N is the number of samples and P is the number of layers. For the ith sample, $\hat{\boldsymbol{\epsilon}}_r^i$ and $\boldsymbol{\epsilon}_{\boldsymbol{r}}^i$ are the prediction values generated from the CNN and the ground truth, respectively. $\mathbf{W}_j$ are the weights of the jth layer, and α is a hyper-parameter introduced to balance the trade-off. The $h(x)$ function here is the sigmoid function, and l is the binary label, which equals 1 for normal rods and 0 for missing rods or background.

4.3 Training method

The learning algorithm chosen is the Adam algorithm [44], which is an adaptive learning rate optimization algorithm, an algorithm for first-order gradient-based optimization of stochastic objective functions, based on adaptive estimates of lower-order moments. It derives from the optimization methods AdaGrad [45] and RMSProp [46]. It leverages the power of adaptive learning rates methods to find individual learning rates for each parameter. The Adam algorithm was designed to combine the advantages of AdaGrad, which works well with sparse gradients, and RMSprop, which works well in on-line and non-stationary settings. Having both of these enables us to use Adam for a broader range of tasks. It uses the squared gradients to scale the learning rate like RMSProp and it takes advantage of momentum by using moving average of the gradient instead of gradient. Its name is derived from adaptive moment estimation, and the Adam method uses estimations of first and second moments of gradient to adapt the learning rate for

each weight of the neural network. The method is straightforward to implement, is computationally efficient, has little memory requirements, the hyper-parameters have intuitive interpretations, and is well suited for large scale problems in terms of data and/or parameters. For completeness, it is described next.

Algorithm 2 ADAM optimization method

1: Initialize the biased first moment estimate and biased second raw moment estimate $\mathbf{m}_t = 0$, $\mathbf{v}_t = 0$;
2: Initialize the hyper-parameter $\beta_1 = 0.9$, $\beta_2 = 0.999$, $\delta = 10^{-8}$, β_1, β_2 are exponential decay rates;
3: Update $t = t + 1$; $\mathbf{m}_t = \beta_1 \mathbf{m}_{t-1} + (1 - \beta_1)\mathbf{g}_t$, $\mathbf{g}_t$ is the gradient of loss function with respect to $\mathbf{W}$;
4: Update $\mathbf{v}_t = \beta_2 \mathbf{v}_{t-1} + (1 - \beta_2)\mathbf{g}_t^2$;
5: Compute bias-corrected moment estimates, $\widehat{\mathbf{m}}_t = \mathbf{m}_t/(1 - \beta_1^t)$, $\widehat{\mathbf{v}}_t = \mathbf{v}_t/(1 - \beta_2^t)$;
6: Update the parameters $\mathbf{W}_t = \mathbf{W}_{t-1} - \alpha \mathbf{m}_t/(\sqrt{\widehat{\mathbf{v}}_t} + \delta)$, α is exponential decaying step size;
7: $\|\mathbf{W}_t - \mathbf{W}_{t-1}\|^2 < \xi$, stop, otherwise, repeat steps from 3 to 6.

4.4 Training dataset

The approach is evaluated on a dataset of a binary 36-rod case. The configuration to collect the data is consistent with the binary-specialized CSI method. Radius c and distance d are the same as mentioned before, in particular, c equals $\lambda/12$ and d equals $\lambda/4$. The dataset involves 3000 samples for the training of the network, each sample containing the real part of the scattered fields collected by 36 receivers when illuminated by 36 sources set at the same position along the circle of radius 7.2 λ at 3 GHz, and the corresponding contrast map of the micro-structure. Another 100 samples are used to validate the performance of the trained network. Signal to noise ratios equal 30dB. In Fig. 4.4, one example of the training set is given:

4.5 Implementation

The implementation is based on TensorFlow, the batch size is set to 100, and the learning is stopped after 6000 iterations (200 epochs). The GPU employed is Nvidia Geforce Gtx 1080, which takes about 10 minutes for the training of the network. With a well-trained network, it then takes less than 1 second to get the evaluation of the contrast map, which means that real-time diagnostic could be achieved. Fig. 4.5 shows how the average

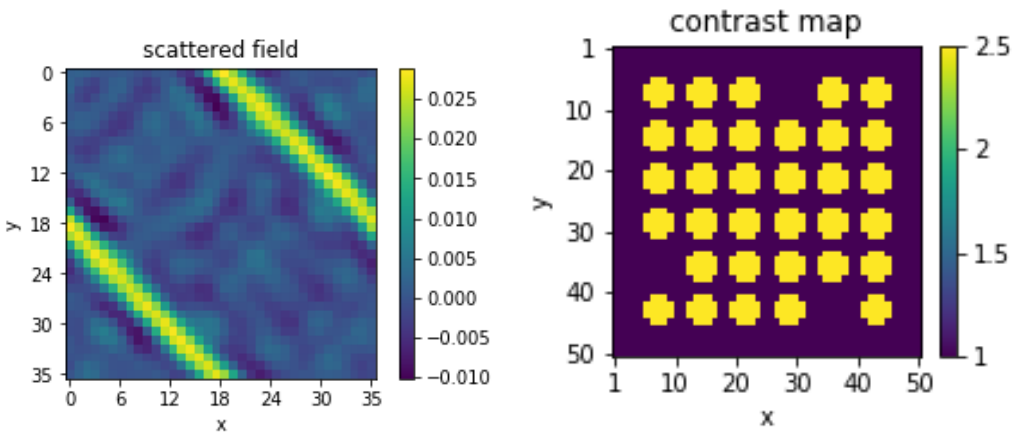

Figure 4.4: Example of training set, left: the real part of scattered field, right: the corresponding contrast map of the micro-structure

standard error between the updated ROI map and the true ROI map changes during each iteration of optimisation. Obviously, the error descends gradually, and when the cost function converges, the error is small enough.

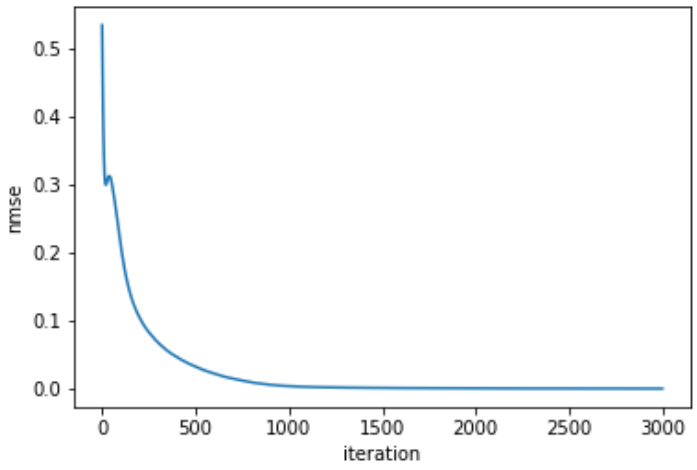

Figure 4.5: The error variation as a function of the iteration number.

4.6 The binary-specialized CNN: a reference example

Fig. 4.6 shows the results of the binary-specialized CNN for the 36-rod case. From the retrieved map, the positions of missing rods can easily be recognized. From the top to

the bottom in the figure, one displays the test results of the well-trained network for three different contrast cases, 2.5, 4, and 5. When the contrast value is as high as 5, the retrieval of the contrast map is still realized, so that one can localize the missing rods.

4.6.1 Different configurations for the test

One important consideration for an inverse scattering problem is the configuration of transmitters and receivers; the number and the position of transmitters and receivers should be well designed, or better said, such as results do not overly depend on this decision. Here one is testing three different configurations, the relative error being computed as

$$ERR = \frac{1}{N}\sum_{i=1}^{N}\frac{\|\boldsymbol{\epsilon}_r^i - \hat{\boldsymbol{\epsilon}}_r^i\|^2}{\|\boldsymbol{\epsilon}_r^i\|^2}, \tag{4.5}$$

where N is the number of test samples.

1) The monostatic configuration is constituted by a single antenna which is operated on the S circle both as transmitter and as receiver, for which the relative error is equal to 0.00021.

2) The bistatic configuration involves two antennas on S, separated by an angle of 60 degrees: one works as transmitter and receiver, the other as receiver; in this case, the relative error is equal to 0.00018.

3) The multistatic configuration comprises four antennas on S, distributed over a sector of 90 degrees, each one separated by 30 degrees: one antenna works as transmitter and receiver, the other three work as receivers; the relative error is equal to 0.00016 for this case.

One observes that (results are not illustrated for sake of brevity) upon increasing the number of antennas, which means that the dataset contains increasing information (up to an extent as is well known), the result of the trained network improves.

4.6.2 Single frequency vs. multiple frequencies of operation

The results of the binary-specialized CNN when using data at a single frequency and at multiple frequencies are to be compared. Indeed, in any experimental condition, using different frequencies to generate the training data is expected to be much easier to be performed than changing the geometrical configuration of the micro-structure, so one compares the difference between using a single frequency as 3 GHz for 3000 different configurations of the micro-structure and using 10 of them from 1 to 10 GHz with a 1 GHz step for 300 different configurations of the micro-structure (evidently one keeps the

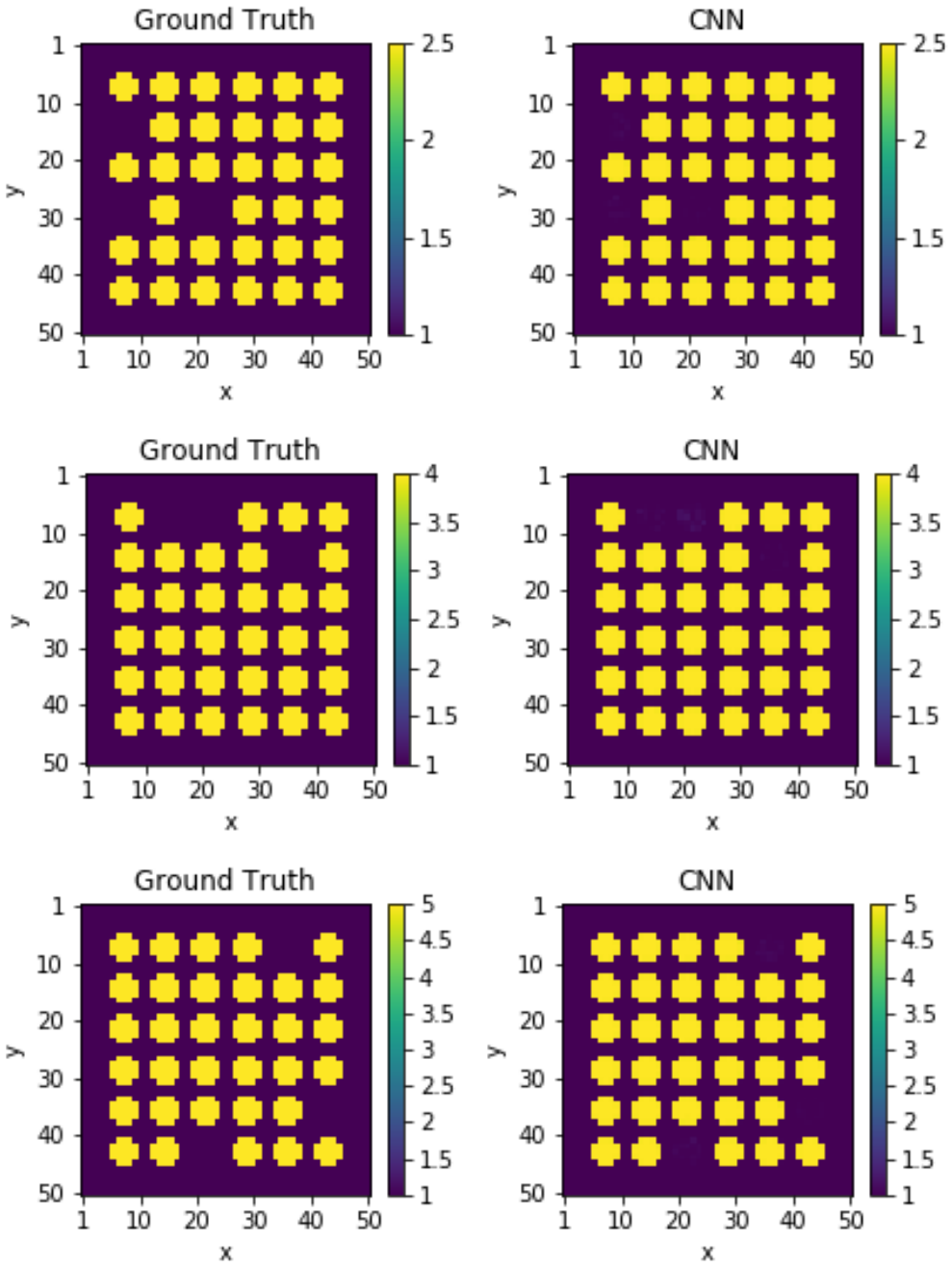

Figure 4.6: Results of the binary-specialized CNN for 36 rods, left column is the ground truth, right column is the CNN reconstruction result, from top to bottom the contrast values are 2.5, 4 and 5.

geometrical dimensions of the micro-structure the same throughout the frequency band of operation). According to the results observed, as long as one has a similar size of the data, the results are similar, but the weight of frequency and configuration deserves more investigation, here one performs simple tests, without further mathematical inspection.

4.6.3 Different data noise ratios

In this work, three different signal to noise ratios have been used to test the performance of the trained network. Three results are proposed in Table 4.1. From those, one observes that when the SNR is equal to 30dB, the performance of the trained network is quite good, while when the SNR is equal to 10dB, the performance of the trained network remains fair, yet errors are larger than 4%.

Table 4.1: Errors of reconstruction for different noise levels.

SNR(dB)	**30**	**20**	**10**
Example of 36 rods	0.00021	0.01172	0.04502

4.6.4 Different values of contrast

As shown in Fig. 4.6 introduced before, the binary-specialized CNN can achieve reconstructions of the contrast map for contrast values 2.5, 4, and 5. As one knows, for the CSI method, the contrast value should be small, so the purpose of this test is to make sure of the performance of binary-specialized CNN for the higher contrast case. As one has investigated, for a relative contrast up to 4, the CNN method works well, while for a contrast value equal to 5, the result turns out less good, though it can still be seen as acceptable. Table 4.2 provides the relative error ERR of CNN for the 36-rod-case, when the contrast value is set at the aforementioned contrsats of 2.5, 4, and 5.

Table 4.2: Errors ERR of reconstruction using binary-specialized CNN.

relative permittivity	**2.5**	**4**	**5**
Example of 36 rods	0.00021	0.02363	0.04320

4.6.5 Additional results for different numbers of missing rods and different shapes using binary-specialized CNN

Extending the application of the binary-specialized CNN method to different numbers of missing rods, i.e., not limited to three missing rods, is of interest. A training set that contains 6000 examples with missing rod number that is going from 2 to 5 is used to train the network as built. Illustrative results of application of the binary-specialized CNN to cases with different numbers of missing rods are displayed in Fig. 4.7. Two cases: missing 1 rod and missing 6 rods, which are not included in the training set of missing-rod cases, have been tested to further evaluate the performance of the trained network, typical results being displayed in Fig. 4.8. The test result on the missing 1 rod case appears quite good, and all the test cases can achieve accurate reconstruction, and for the 6 rods missing case, most results are good, though a few of the test results may not, which is also shown in the proposed figure.

Another extension of the binary-specialized CNN method is for different shapes of the micro-structure. Another training set that contains 6000 examples of different shapes is used to train the built network. Results for three different shapes are shown in Fig. 4.9. In brief, when the training set contains more different shapes, the trained network can be more adaptive for more different cases.

Overall, the binary-specialized CNN method achieves accurate contrast map reconstruction in all cases studied, pending the problem that it encounters with truly high contrasts, both in terms of localization of rods and retrieval of their contrasts with respect to the embedding medium and to one another, even if noisy data are input. Ground truth and the retrieved map are almost indistinguishable, as epitomized by the small values of the square-norm errors which are correspondingly achieved in most examples.

4.6.6 Extension to random contrast distribution

The binary case of ROI is for the localization of missing rods, while in the inverse scattering problem, there are several situations that the task is about the reconstruction of ROI with different permittivities. After some modification, the built network can be used to reconstruct the distribution of random contrast. Firstly, the loss function can be redefined as:

$$LOSS = \frac{1}{N}\sum_{i=1}^{N} \|\boldsymbol{\epsilon}_r^i - \hat{\boldsymbol{\epsilon}}_r^i\|^2 + \alpha \sum_{j=1}^{P} \mathbf{W}_j^2, \tag{4.6}$$

within which N is the number of samples and P is the number of layers. For the ith sample, $\hat{\boldsymbol{\epsilon}}_r^i$ and $\boldsymbol{\epsilon}_r^i$ are the prediction values generated from the CNN and the ground

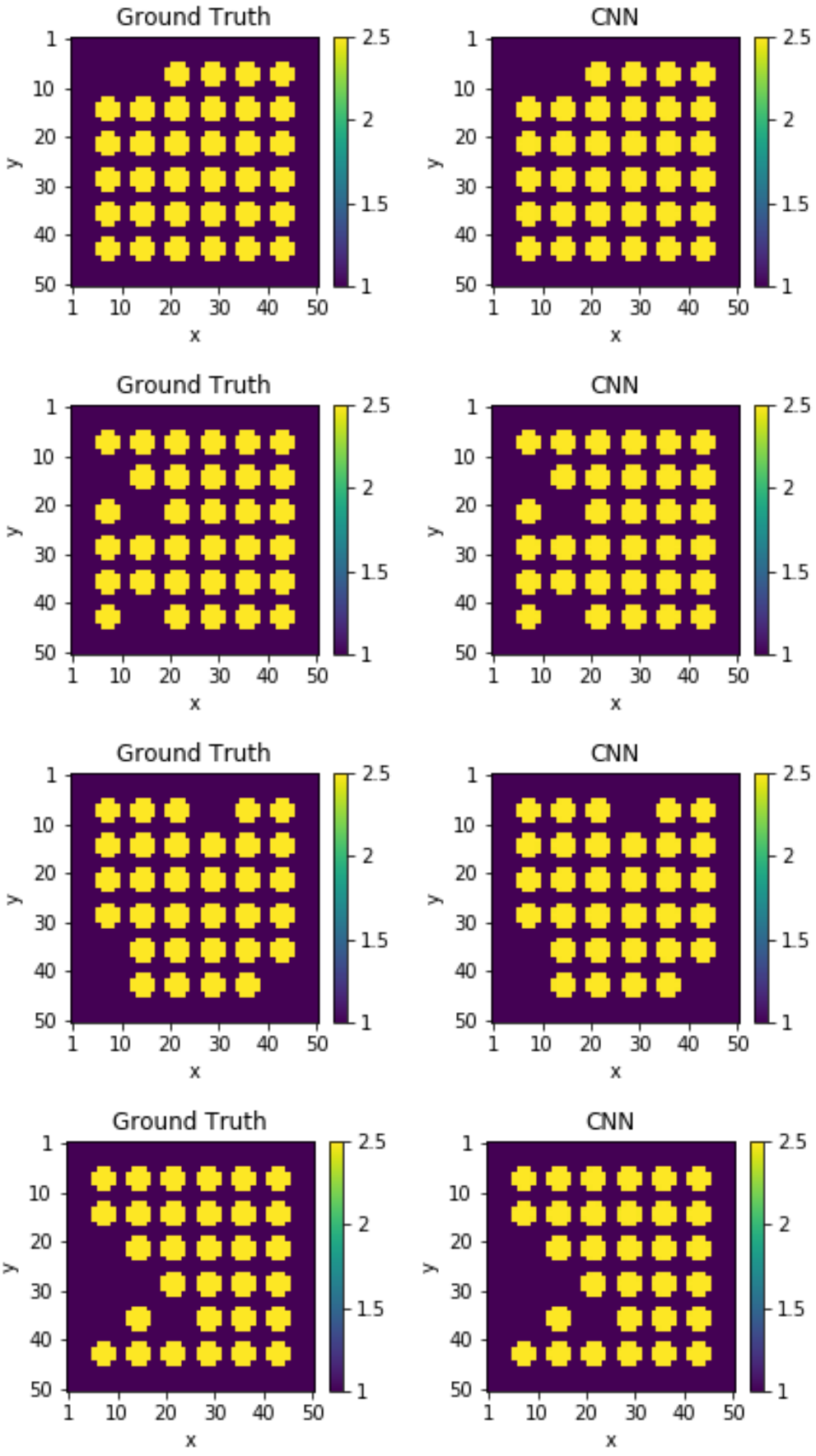

Figure 4.7: Maps provided by CNN trained by different missing rods cases. Top to bottom: missing 2 rods cases, missing 3 rods cases, missing 4 rods cases, missing 5 rods cases. Left: ground truth, right: binary-specialized CNN reconstruction result.

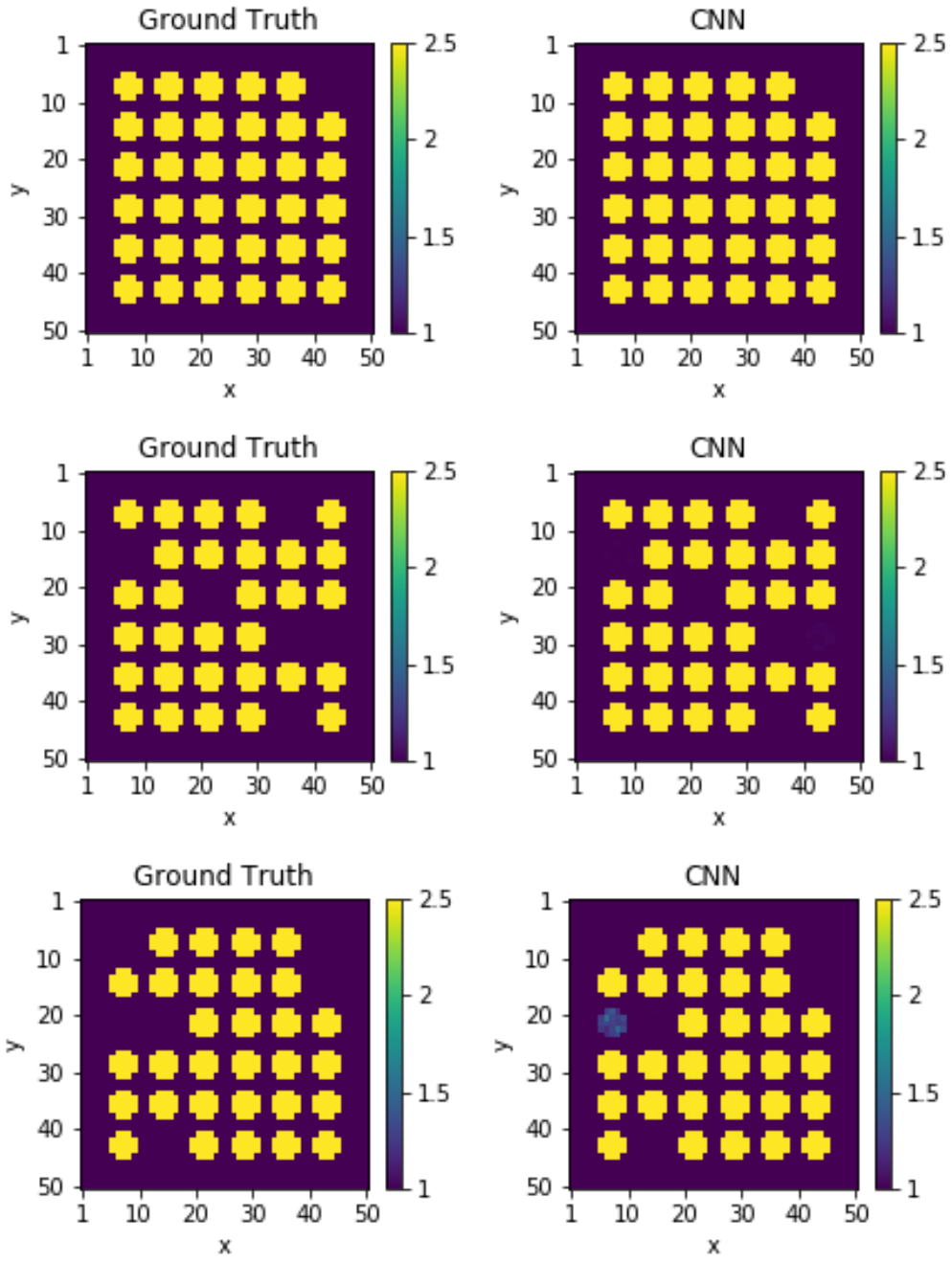

Figure 4.8: Test examples for different missing numbers: first row is missing 1 rod case, second and third rows are two missing 6 rods cases: one is a good reconstruction result, another one is an imperfect reconstruction result.

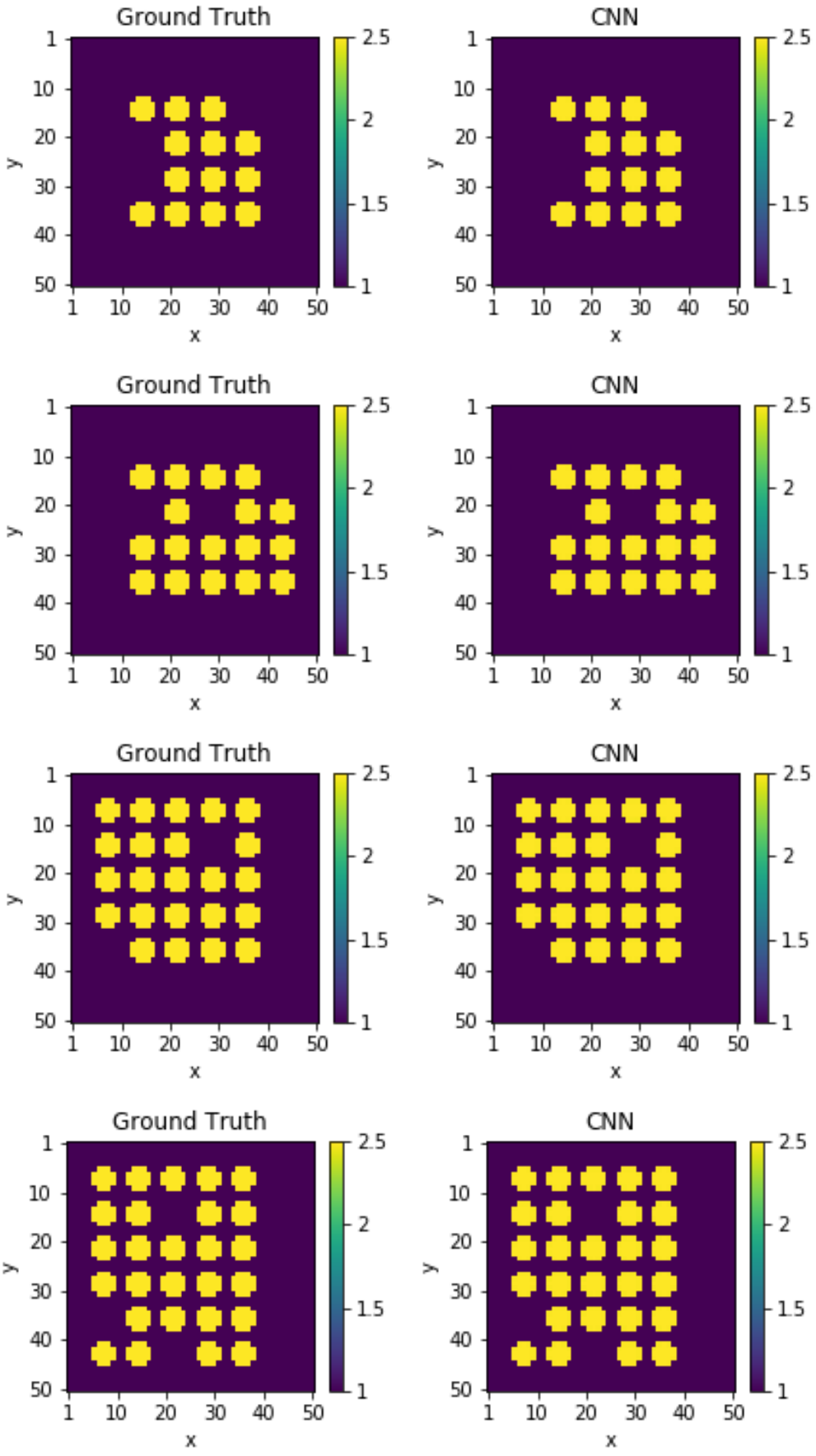

Figure 4.9: Test examples for different shapes: from top to bottom: 16 rods, 20 rods, 25 rods, 30 rods

truth, respectively. $\mathbf{W}_j$ are the weights of the jth layer, and α is a hyper-parameter introduced to balance the trade-off. As for the CNN structure, there is no modification. While the training set and test set are changed to random contrast value distribution and the related collected field.

CNN reconstruction results for the random contrast case are shown in Fig. 4.10 and Fig. 4.11. The contrast value is random in [1, 3], and the trained network can realize the mapping from scattered field to contrast distribution for the two different structures with a number of rods equal to 16 and to 36.

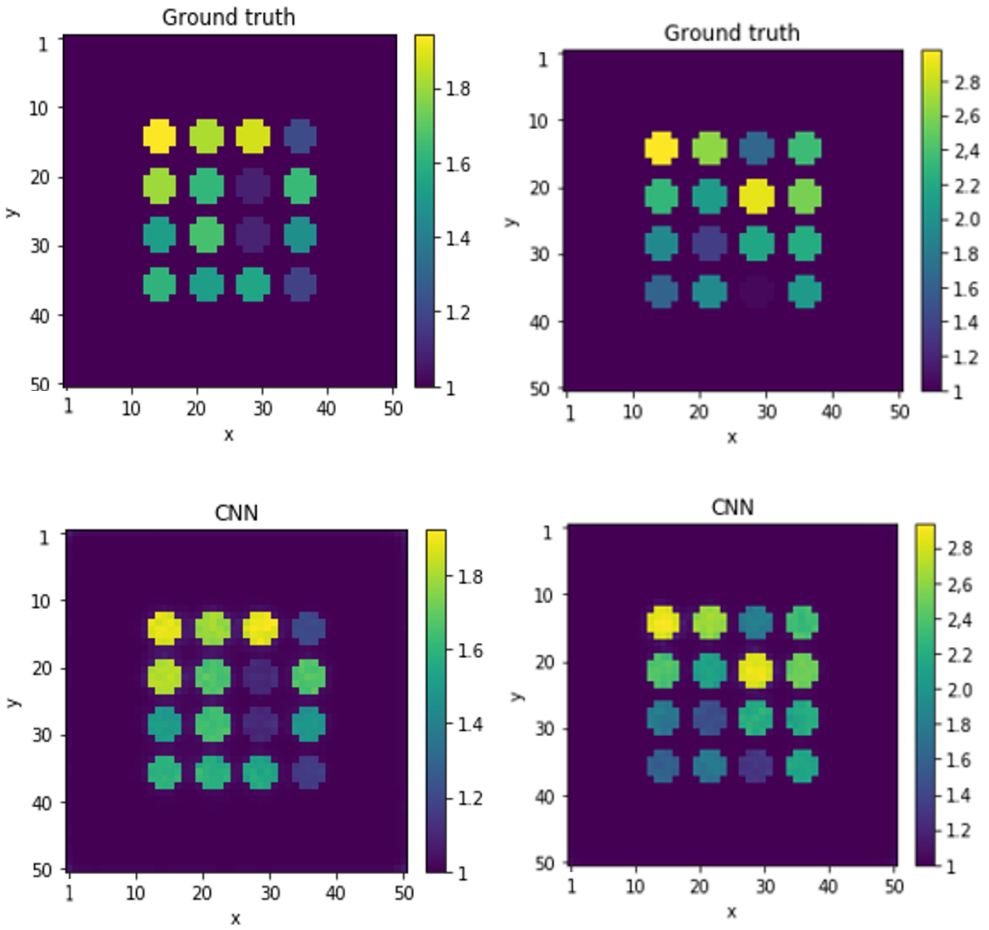

Figure 4.10: Maps provided by CNN for examples involving 16 rods. Top to bottom: ground truth, CNN result. Left column: example 1 with lower permittivity. Right column: example 2 with higher permittivity.

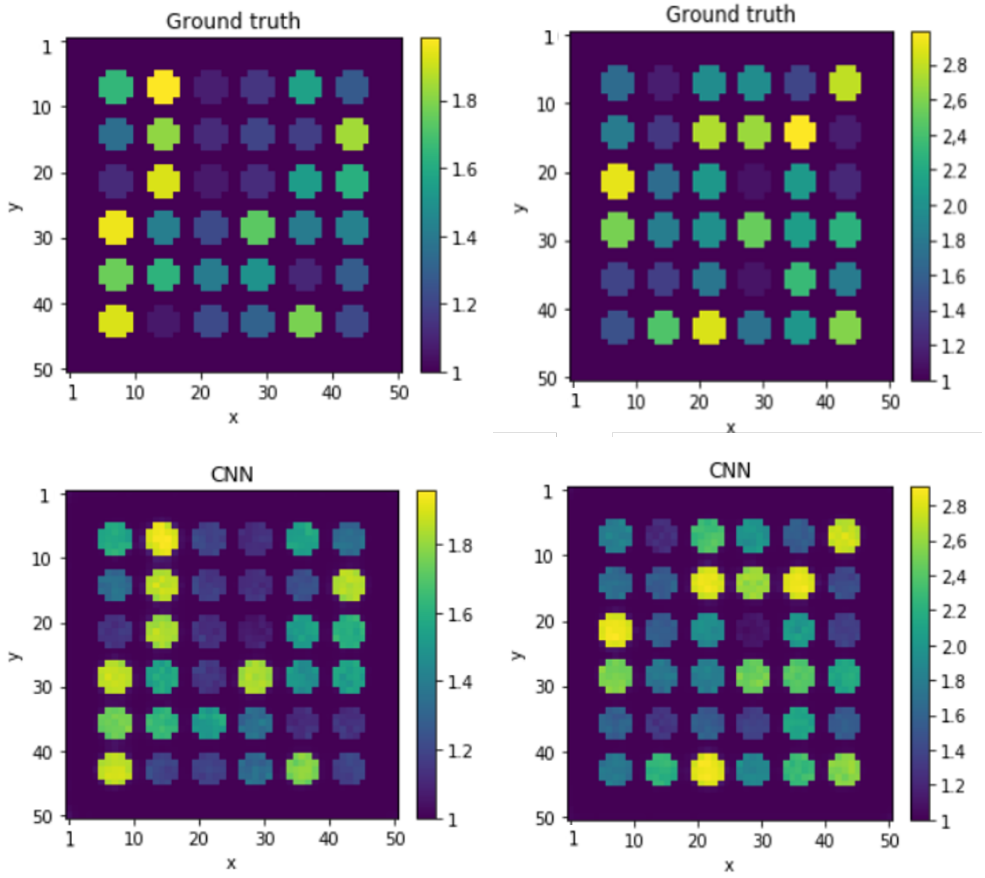

Figure 4.11: Maps provided by CNN for examples involving 36 rods. Top to bottom: ground truth, CNN result. Left column: example 1 with lower permittivity. Right column: example 2 with higher permittivity.

Chapter 5

Imaging by recurrent neural networks in time domain

Compared with the work in last chapter, all the work herein is carried in the time domain, i.e., data are due to transient illuminations. RNN are introduced to solve the inverse scattering problem at hand, long short-term memory (LSTM) as a gated RNN being used, as such kind can make use of the sequential information. CNN method is also used, considering that it has already shown good performances for dealing the inverse scattering problem.

In addition, according to a carefully designed protocol, several experiments are carried out in a microwave anechoic chamber on a prototype of dielectric micro-structure using wide-band ridged horn antennas operated in a forward scattering configuration, and the collected laboratory-controlled measurement data further validate the performance of the proposed methods, now in a truly non-ideal context.

5.1 Motivation of using RNN

In the previous chapter, the CNN method has been applied to tackle the inverse scattering problem under different guises. In the present chapter, another important deep learning model-RNN is introduced and the hidden association between the RNN and electromagnetic wave is discussed, and from that on, RNN is used to solve the problem. As we know that most problems in electromagnetics can be described by the wave equation, the dynamics of a scalar wave field distribution $u(x, y, z)$ are governed by the second-order partial differential equation.

$$\frac{\partial^2 u}{\partial t^2} - c^2 \cdot \nabla^2 u = f, \tag{5.1}$$

where ∇^2 is the Laplace operator, c is the wave speed, and f is the source term, and the discretization version is written as,

$$\frac{u_{t+1} - 2u_t + u_{t-1}}{\Delta t^2} - c^2 \cdot \nabla^2 u_t = f_t, \tag{5.2}$$

where Δ is a time step size. Define $\mathbf{h}_t = [u_t, u_{t-1}]^T$, where u_t or u_{t-1} is the field vector. The updated wave equation can be represented in the following matrix form [28]:

$$\begin{bmatrix} u_{t+1} \\ u_t \end{bmatrix} = \begin{bmatrix} 2 + \Delta t^2 \cdot c^2 \cdot \nabla^2 & -1 \\ 1 & 0 \end{bmatrix} \cdot \begin{bmatrix} u_t \\ u_{t-1} \end{bmatrix} + \Delta t^2 \cdot \begin{bmatrix} f_t \\ 0 \end{bmatrix}, \tag{5.3}$$

So the matrix form is

$$\mathbf{h}_t = \mathbf{A}(h_{t-1}) \cdot \mathbf{h}_{t-1} + \mathbf{P} \cdot \mathbf{x_t}, \tag{5.4}$$

where $\mathbf{P}$ is a linear operator. In Fig. 5.1, the architecture of RNN is detailed; RNN is a network that maintains some kind of state [16], its output could be used as part of the next input, so the information can propagate along as the network passes over the sequence. Compare the wave equation with the RNN update equation:

$$\mathbf{h}_t = \delta(\mathbf{W}_{ih}\mathbf{x}_t + \mathbf{b}_{ih} + \mathbf{W}_{hh}h_{(t-1)} + \mathbf{b}_{hh}), \tag{5.5}$$

ignoring the $\mathbf{b}_{ih}$ and $\mathbf{b}_{hh}$, the wave equation can be approximated by RNN, which is the inspiration of using RNN to solve the inverse scattering problem at hand here.

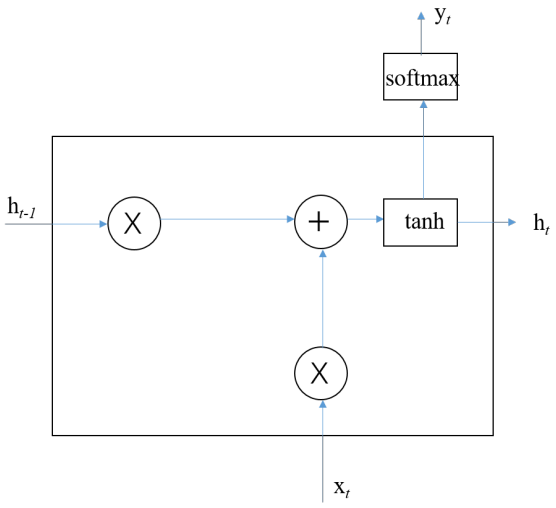

Figure 5.1: RNN cell.

Actually the simple RNN has gradient exploration and gradient vanishing problems because of the long-term dependencies, it is rather hard for training and it cannot process very long sequences if using tanh or ReLU as an activation function. To avoid the gradient vanishing problem in simple RNN, gated RNN employs a gate function, which selectively let part of the information passes. The gate is composed of a sigmoid unit and a point-wise product operation. The sigmoid unit outputs 1 or 0 to determine whether to pass or to block, and then train the combination of these gates. Therefore, when the gate is open (the gradient is close to 1), the gradient will not be vanishing. As the sigmoid does not exceed 1, then the gradient will not explode. The long short-term memory (LSTM) [47] is a typical gated RNN, it is used in our work, since compared with simple RNN, LSTM has a better performance on longer sequences. It has two transmission states: hidden state and cell state, LSTM have 3 gates: forget gate, input gate and

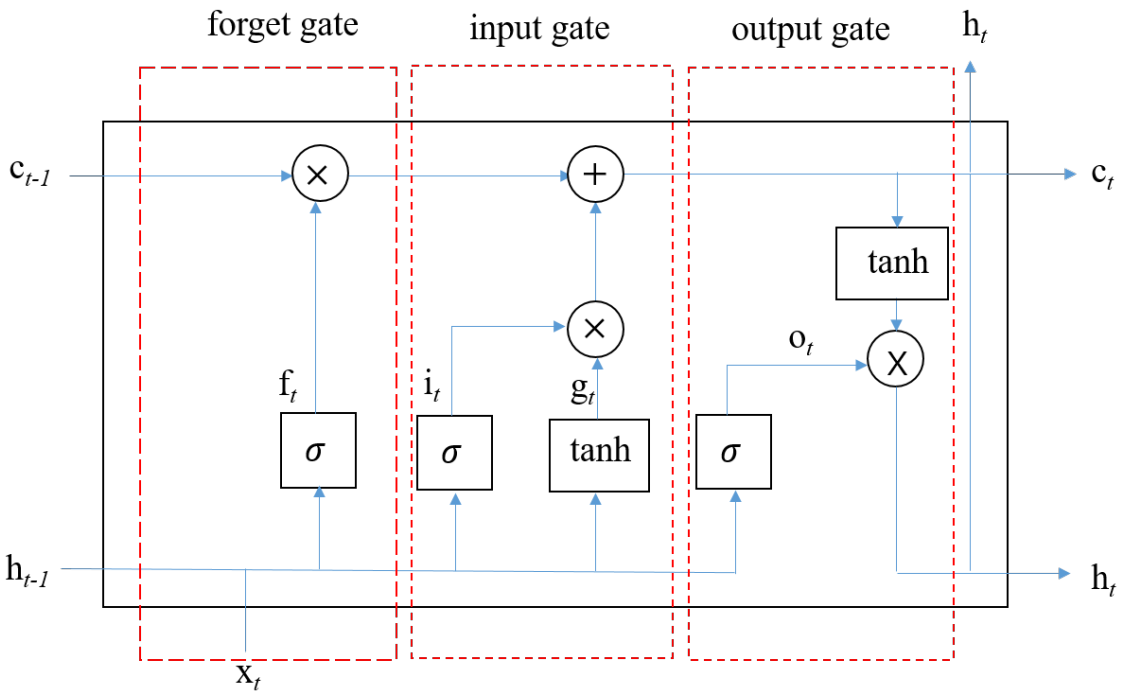

Figure 5.2: LSTM cell.

output gate; the forget gate decides how much information can be omitted from the previous cell, as shown in the Eq. 5.6, it takes the previous state h_{t-1} and the input x_t and outputs a number between 0 and 1 for the cell state $c_t - 1$ by a sigmoid function, where 0 means "omitting" and 1 means "keeping". Similarly, the input gate decides how much of this unit is added to the current state, the sigmoid function is used to decide

the mount of passing value, the tanh function gives weight from -1 to 1. The output gate determines which part of the current cell enters into the output. The detailed relations are

$$f_t = \sigma(W_{if}x_t + b_{if} + W_{hf}h_{t-1} + b_{hf}), \tag{5.6}$$

$$i_t = \sigma(W_{ii}x_t + b_{ii} + W_{hi}h_{t-1} + b_{hi}), \tag{5.7}$$

$$g_t = tanh(W_{ig}x_t + b_{ig} + W_{hg}h_{t-1} + b_{hg}), \tag{5.8}$$

$$o_t = \sigma(W_{io}x_t + b_{io} + W_{ho}h_{t-1} + b_{ho}), \tag{5.9}$$

$$c_t = f_t \odot c_{t-1} + i_t \odot g_t, \tag{5.10}$$

$$h_t = o_t \odot tanh(c_t), \tag{5.11}$$

where h_t is the hidden state at time t, c_t is the cell state at time t, x_t is the input at time t, h_{t-1} is the hidden state of the layer at time $t-1$, and i_t, f_t, g_t, o_t are the input, forget, cell, and output gates, respectively, $\odot$ is the Hadamard product.

To compare different types of RNN cell, the GRU [48] is represented in Fig. 5.3. GRU also uses the gate function, and it can be regarded as a simplified version of LSTM. The functional details of GRU are listed below:

$$r_t = \sigma(W_{ir}x_t + b_{ir} + W_{hr}h_{t-1} + b_{hr}), \tag{5.12}$$

$$z_t = \sigma(W_{iz}x_t + b_{iz} + W_{hz}h_{t-1} + b_{hz}), \tag{5.13}$$

$$n_t = tanh(W_{in}x_t + b_{in} + r_t \odot (W_{hn}h_{t-1} + b_{hn})), \tag{5.14}$$

$$h_t = (1 - z_t) * n_t + z_t \odot h_{(t-1)}. \tag{5.15}$$

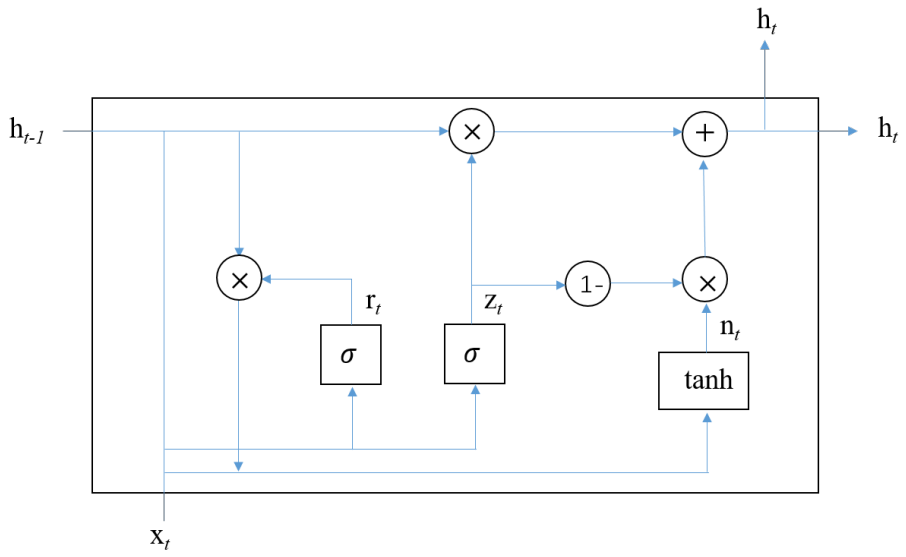

Figure 5.3: GRU cell.

5.2 LSTM structure

As shown in Fig. 5.4, the proposed LSTM structure contains two blocks, the first LSTM block has 128 features in the hidden state h, and the second one has 64 features in the hidden state, then a full-connected layer combines the outputs from two blocks. After the linear transform, the batch normalization is used before a ReLU function to avoid gradient vanishing. The $x_0 ... x_n$ is the field time sequence.

To design the architecture, in order to avoid augmenting the complexity too much, one LSTM block contains 128 features in the hidden state h, is used at the beginning, but the modelling capability is not satisfied, thus another block with 64 features in the hidden state is added, thus it meets the need of modelling, and with the help of batch normalization and the ReLU function, the speed of convergence is increased.

As said, the input of the structure is the collected field thus the size of one input is $[N_t, N_r, t]$, N_t number of transmitters, N_r number of receivers, t time steps in one signal. Meanwhile the output is the index of the rods, i.e., a list of data contains only two values, for example $[1, 1, 1, 0..., 0, 1, 0, ...]$, the size of which is the number of rods, wherein 1 represents a normal (present) rod, and 0 represents a missing rod. 1500 examples in total are used to train the network here. One example of dataset is shown in Fig. 5.5, the collected field being the input and the index of rod being the output of the network.

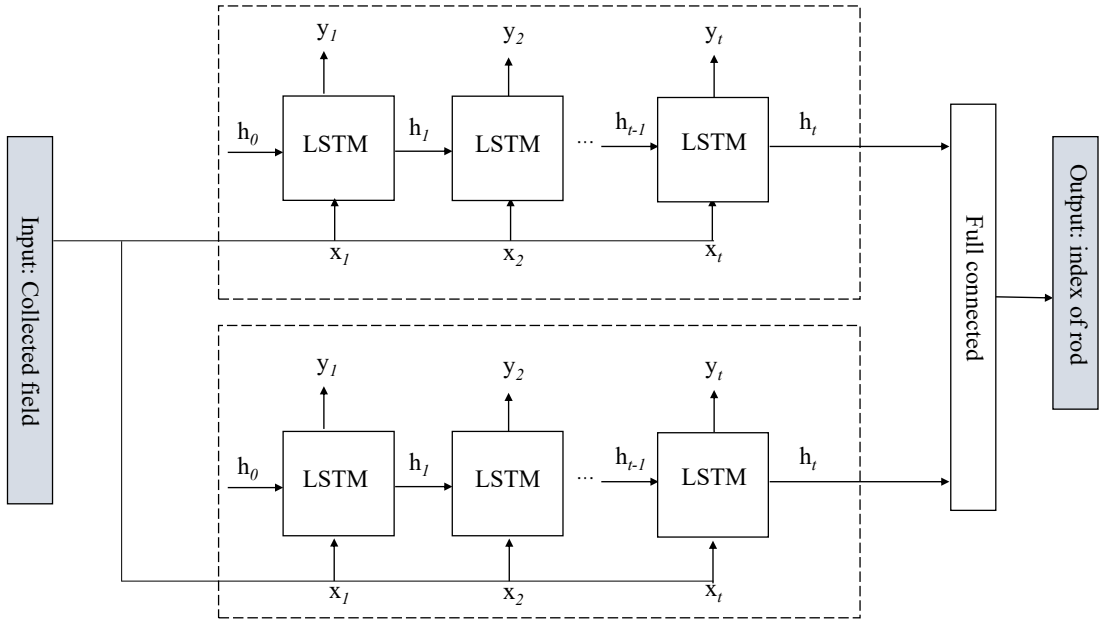

Figure 5.4: Architecture of the proposed LSTM structure, input: collected field, output: index of rods.

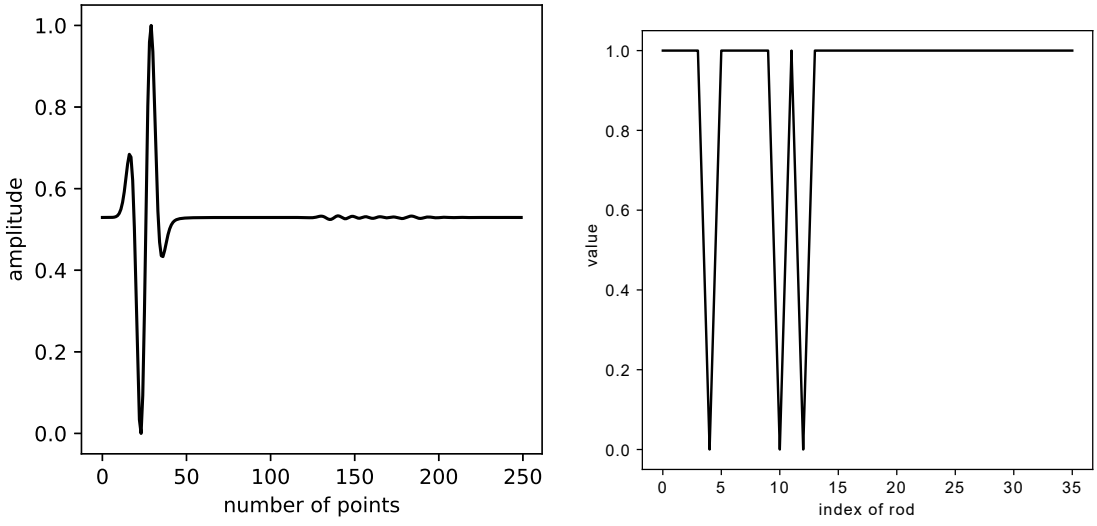

Figure 5.5: Example of dataset for LSTM, the left part is an example of input, the normalized received field at one receiver for one transmitter, each input should have 18 received signals with 18 transmitters, the right part is an example of rod's index.

5.2.1 Dataset

The dataset contains the field in time sequence form is generated by gprMax, it is an open source that uses the FDTD algorithm to solve the Maxwell equations, the core of FDTD method is that the time-dependent Maxwell equations are discretized using central-difference approximations to the space and time partial derivatives, providing at the end a model of interactions between given impulses and the material structure of interest. Suitable absorbing (PML) boundary conditions around a virtual box of proper size complete the model. Ideal line-like transmitters are assumed to generate transverse-magnetic-polarized fields which are impinging upon the micro-structure, and the corresponding scattered scalar electric fields are collected by ideal point-like receivers. The excitation signal used here in the gprMax simulation is a Ricker. Its central frequency from now on is 3 GHz —central wave-length λ in air as of 0.1 m. A multi-static configuration composed of coincident transmitters and receivers at a fixed distance of 0.36 m from the center of the micro-structure is to generate and collect the transient E-field. The computational region with side 0.8 m is meshed with a step of 0.002 m into each direction for the simulation chosen in order to yield reliable numerical results, the distance between closest rods d being equal to 0.02 m and the radius of any present rod being equal to 0.005 m. Notice that rods (present or not) are counted from top left to bottom right, row after row, from top to bottom.

So a dataset containing the field in the time domain is generated by gprMax when 18 transmitters and receivers are used. Considering the data limitation, the training set contains 1500 experiments, and in each E-field data only the first 1000 time steps are kept, since significant information appears to reside within this interval (non zero field), so the size of the input is $[1500, 18, 18, 1000]$. Another 100 examples are used to test the performance. With the performance limitation of GPU, an under-sampling procedure is adopted to reduce the dataset, 1000 time steps are under-sampled by a factor 4 (the Nyquist criterion is respected), so the real size of the input is $[1500, 18, 18, 250]$.

5.2.2 Training process

The loss function henceforth used is

$$LOSS = \frac{1}{N} \sum_{i=1}^{N} \|\boldsymbol{y}^i - \hat{\boldsymbol{y}}^i\|^2, \tag{5.16}$$

in which N is the number of samples at each iteration. For the ith sample, $\hat{\boldsymbol{y}}^i$ and $\boldsymbol{y}^i$ are the prediction index value generated from the LSTM method and the ground truth, respectively.

The learning algorithm chosen is still the ADAM one, choosing a initial learning rate of 0.001 and a decay of 0.9 at every 20 epochs. All the code is realized on the platform Pytorch. Fig. 6.4 shows the iteration curve during training. A GPU NVIDIA Geforce Gtx 1080 is used, which overall takes about 15 minutes.

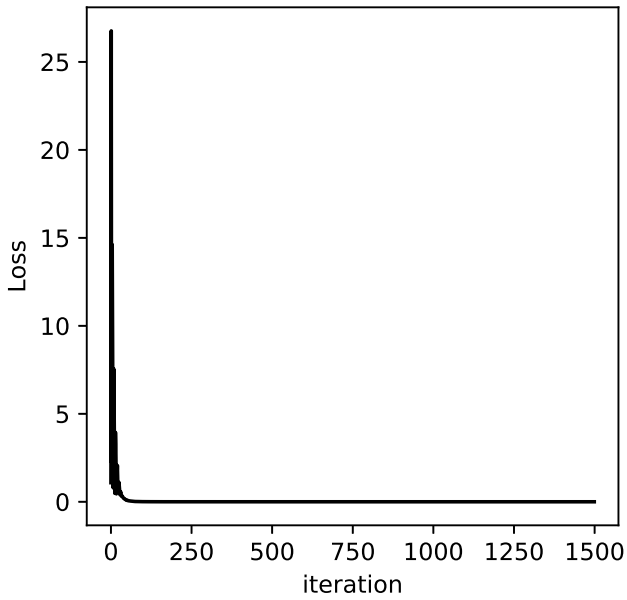

Figure 5.6: Iteration curve during the training.

5.2.3 LSTM Results

Different tests from various configurations of the micro-structure have been carried out in order to validate the performance of the proposed network. The results are shown in Fig. 6.5 for three different missing rod numbers. The mean square error between the ground truth and the predicted value is as small as 0.009.

More missing rods cases are also tested, 300 samples for 4 or 5 missing rods cases replace 300 samples of 3 missing rods cases in the original dataset to increase the diversity of the dataset. The result by using the new dataset is shown in Fig. 5.8, the localization of more missing rods is seen as successful.

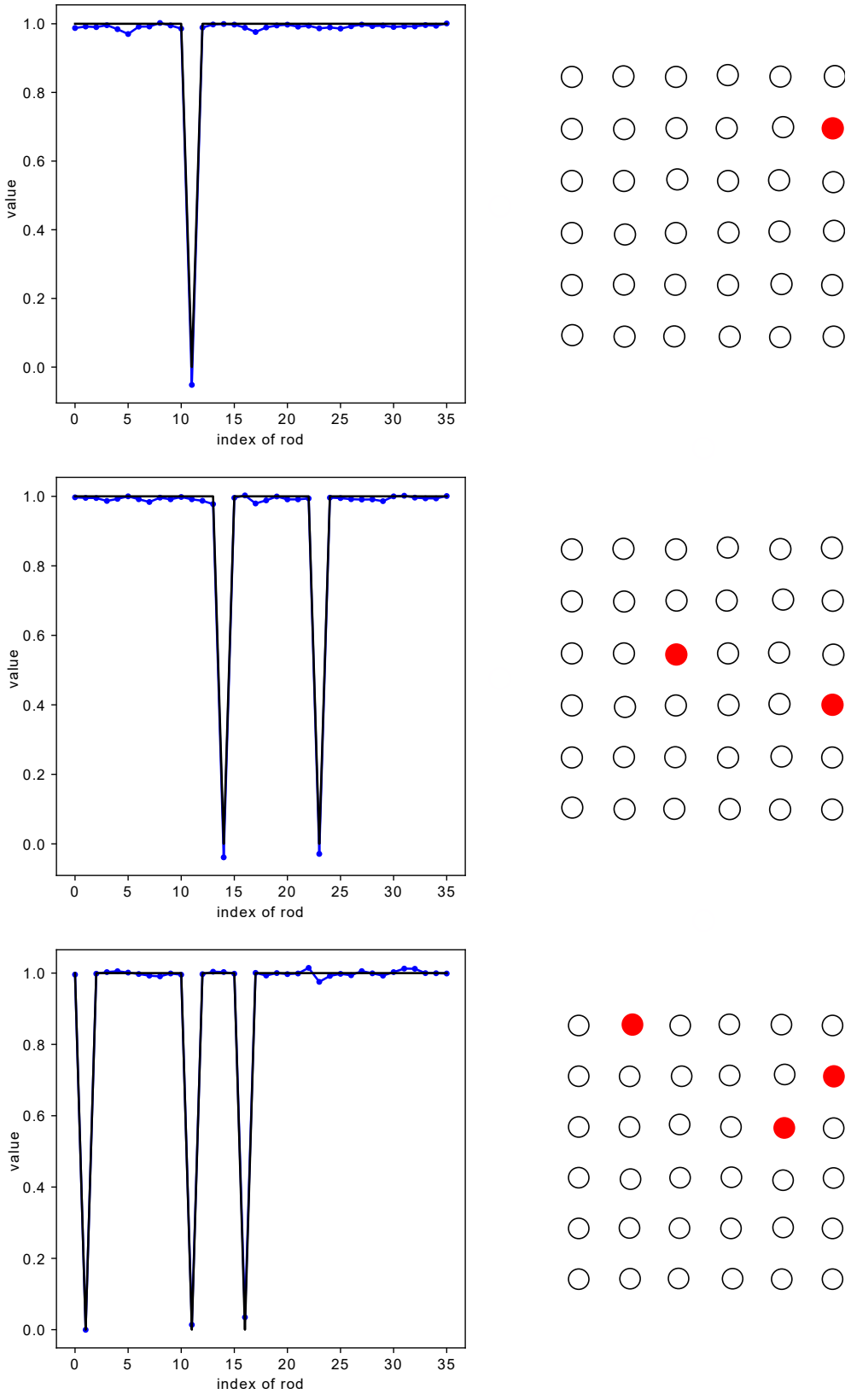

Figure 5.7: LSTM retrievals, from top to bottom: 1, 2, and 3 missing rods, the blue line represents the predicted index, the black line represents the true index.

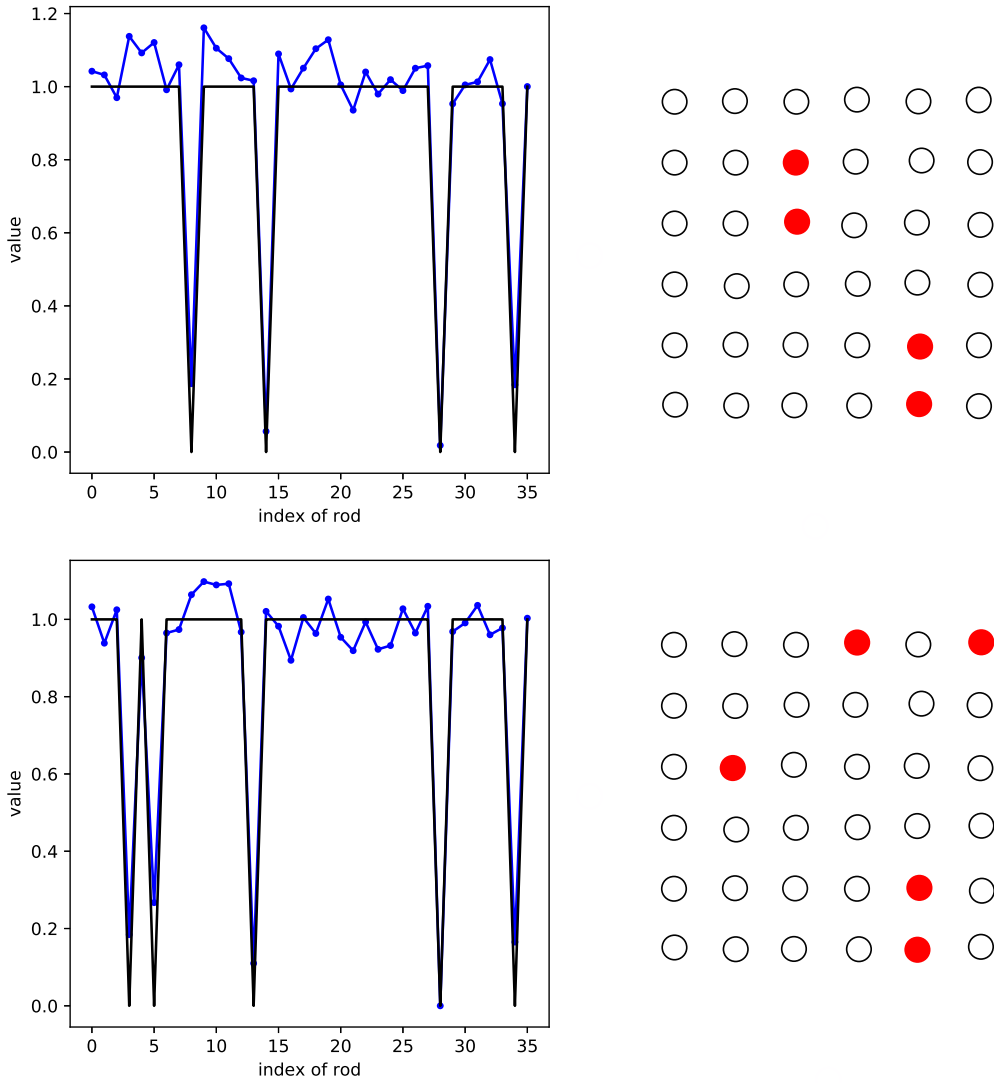

Figure 5.8: LSTM retrievals for 4 and 5 missing rods, the blue line represents the predicted index, the black line represents the true index.

5.3 Comparison with imaging by convolutional neural networks

5.3.1 CNN architecture

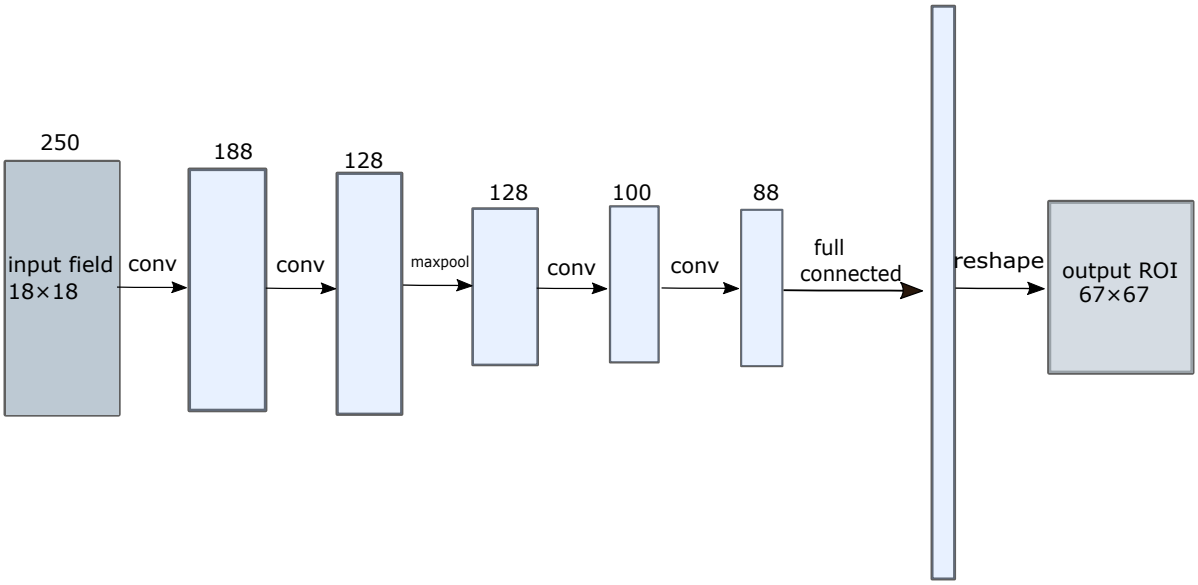

Figure 5.9: Proposed CNN structure, input: the collected field, output: the map of RoI.

CNN has strong modelling capability, and has achieved great success to solve different regression problems. So a structure based on CNN has also been designed for the time domain data, the architecture of which is shown in Fig. 5.9. It has six layers, containing four convolutional layers, one max pooling layer and a full connected layer. The convolutional layer has strong local modelling capabilities with a small number of parameters, and it has the ability to extract local features. the convolutional layer uses a kernel of size $[5, 5]$, and pad zeros outside the edges using a stride of 1, so the layer's outputs have the same spatial dimensions as its inputs. The max pooling layer uses a kernel of size $[2, 2]$, and pads zeros outside the edges using a stride of 2, so the layer's outputs have the half spatial dimensions of its inputs. The full-connected layer gathers the extracted features.

At the start, the CNN structure is designed for dealing with the same dataset as the one of the LSTM structure, but a good regression from the collected field to the index of rod was not achieved. So, instead of using index of rod locations, the map of RoI, which includes more information of the micro-structure, is used as the output of the network.

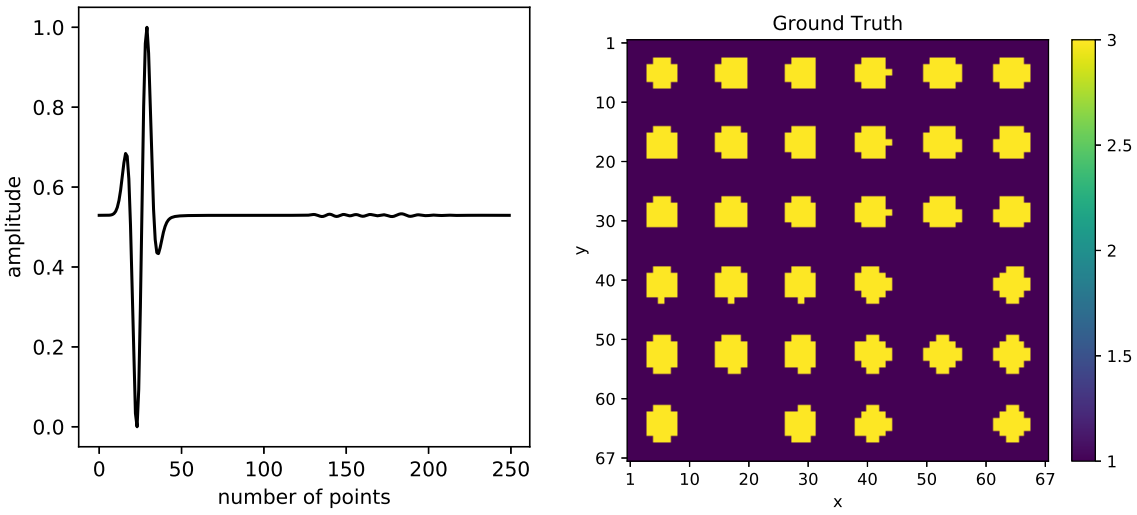

Figure 5.10: Example of dataset for CNN, the left part displays the normalized signal collected at the first receiver when the structure is illuminated by the first transmitter, the right part is the corresponding map of the RoI.

Fig. 5.10 shows one example, the input field remains the same as for the LSTM structure, while the map of the RoI is divided into 67×67 pixels. Correspondingly, the loss function becomes as

$$LOSS = \frac{1}{N}\sum_{i=1}^{N} \|\boldsymbol{\epsilon}^i - \hat{\boldsymbol{\epsilon}}^i\|^2, \tag{5.17}$$

for the ith sample, $\hat{\boldsymbol{\epsilon}}^i$ and $\boldsymbol{\epsilon}^i$ are the prediction value generated from CNN and the ground truth, respectively.

5.3.2 CNN results

As shown in Fig. 5.11, the results for three different missing rod numbers turn out to be clear enough to tell the location of the missing rod, the mean square error between the reconstructed map and the ground truth being 0.00137. The results for more missing rod cases are shown in Fig. 5.12.

5.3.3 Comparison between CNN and RNN

The proposed two learning methods both achieve the localization of the missing rods with different forms of output representation. The difference of performance between two structures can be inferred however. The proposed RNN structure (namely the LSTM), is more like wave propagation from the working principle, RNN is recurrent in nature, it is

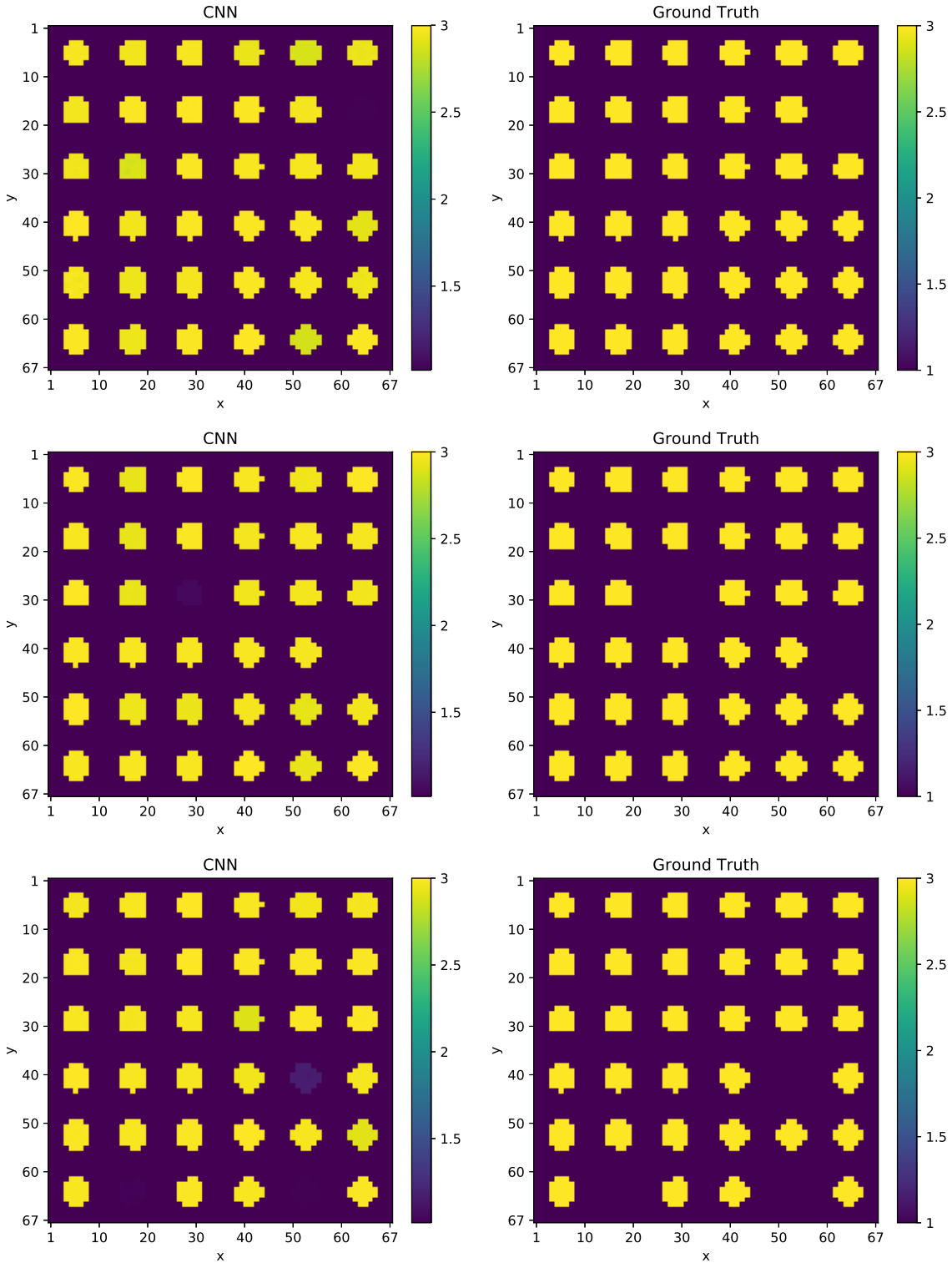

Figure 5.11: CNN retrievals, from top to bottom: 1, 2 and 3 missing rods, the left column shows the CNN retrieved results, the right column shows the ground truth.

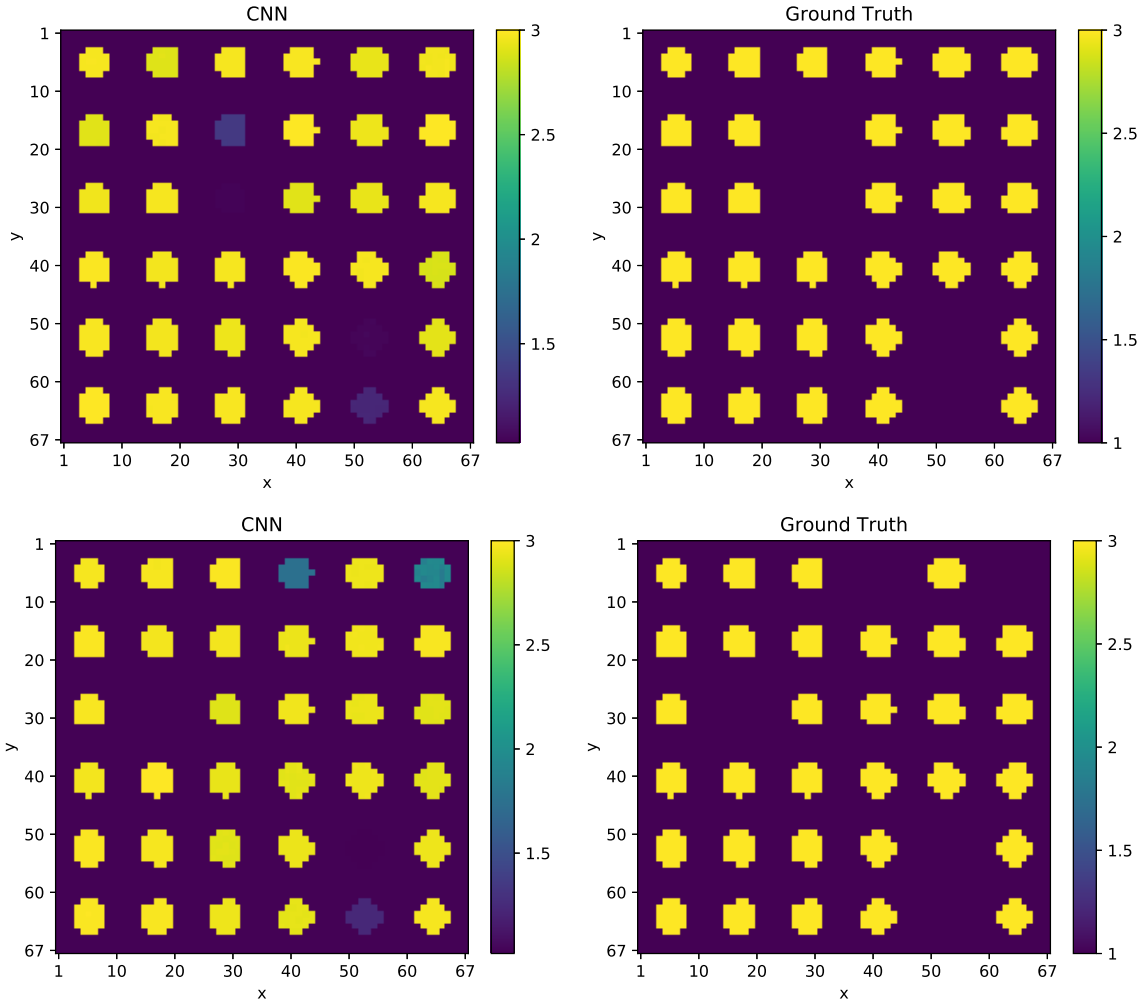

Figure 5.12: CNN retrievals for 4 and 5 missing rods, the left column shows the CNN retrieved results, the right column shows the ground truth.

a network that maintains some kind of states, its output could be used as the part of the next input, so the information can be propagated along as the network passes over the sequence. Yet, to our knowledge, CNN exhibits better performance on processing images.

5.4 Validation on laboratory-controlled data

5.4.1 The configuration of experiments

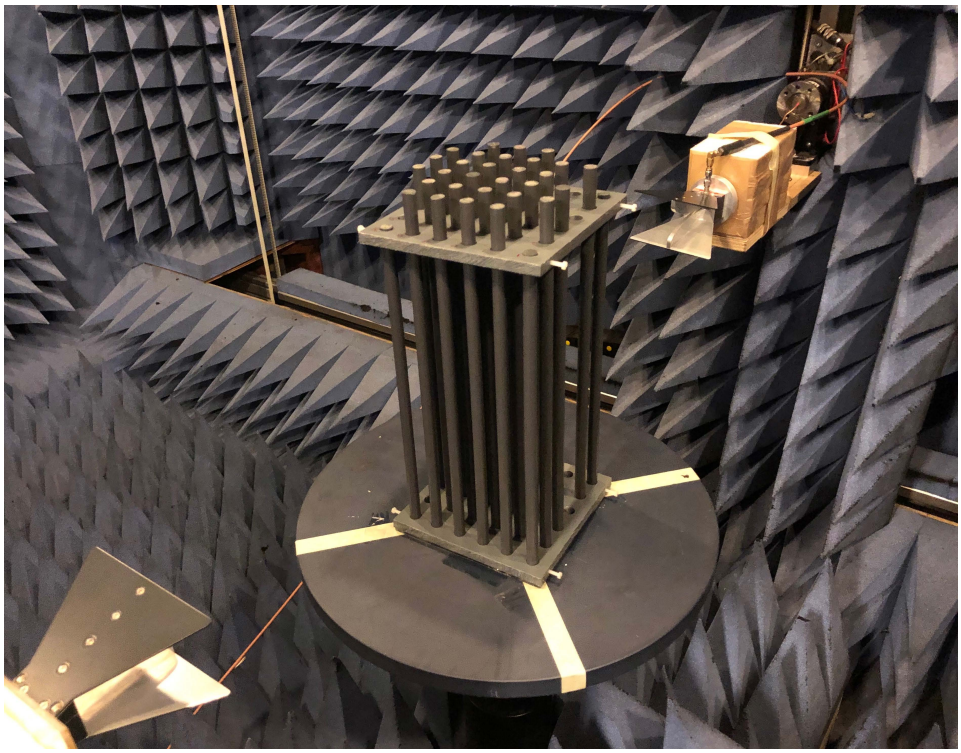

Figure 5.13: Configuration of the laboratory-controlled experiment.

Fig. 5.13 is the photography of a dielectric micro-structure as considered in a laboratory-controlled experiment in a microwave anechoic chamber. 36 of rather long (30 cm) circular cylindrical rods, quite thin (nominal diameter of 1.5 cm) and close to one another (nominal distance center to center of 2.5 cm) with respect to the wavelength of operation (one takes as central value a 3 GHz frequency —10 cm-wavelength— but experiments are carried out in a broad band, typically 2 to 6 GHz) are placed within an air RoI. Each rod is homogeneous, isotropic and non-magnetic in practice, and it has been cut from a lossless plexiglass material, with relative permittivity measured at about 3 ± 0.1.

Two identical microwave ridged horn antennas are set outside the region of interest wherein the micro-structure is centred, one is acting as emitter and one is acting as receiver, centred within the central cross-section of the set, in present practice in a forward scattering configuration (transmitting and receiving antennas simply face each other).

The set of rods can be rotated around from 0 to 360 degrees, in a step-by-step fashion, and signals thereupon collected for each position using a vector network analyser in the frequency domain over 301 points between 2 and 6 GHz. The network analyser has been calibrated to cancel the effect of the cables losses and the measurement data are filtered with a Hamming window centred at the frequency 3 GHz with a bandwidth of 2 GHz. Then the filtered data are inverse Fourier transformed to get the time domain field that can be used in the validation procedure of the proposed methods.

5.4.2 Results on experimental data

The proposed LSTM structure is applied using the collected experimental data. There are 815 experimental data in total, 765 of them are used to do the training, the remaining 50 are used as the test set. One example of the field is shown in Fig 5.14, which contains 601 time samples for each signal, so the input size of the training dataset is $[765, 36, 1, 601]$.

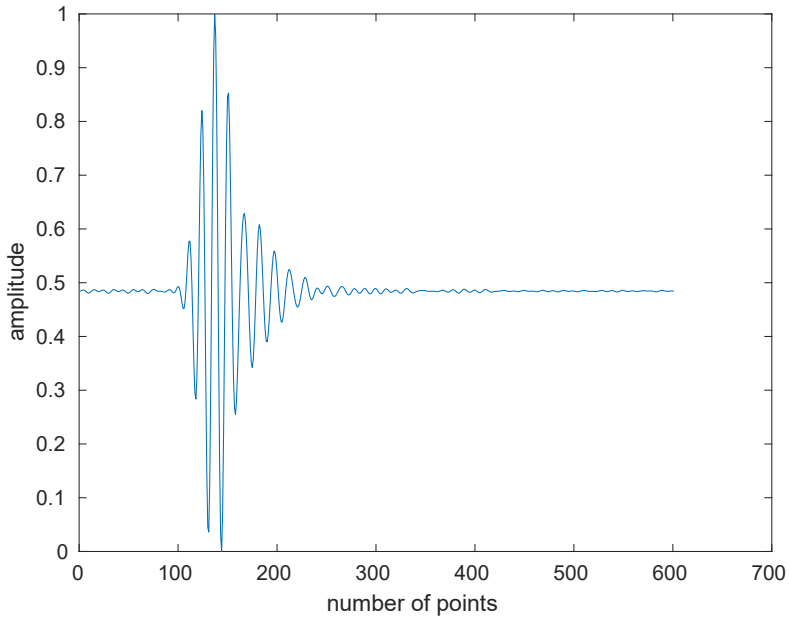

Figure 5.14: Example of collected experimental data.

The result is shown in Fig. 5.15, the mean square error between the retrieved results and the ground truth being equal to 0.024. From the LSTM result, for most cases, the location of a missing rod can be found, even though with some fluctuation. Yet, sometimes the fluctuation looks somewhat erratic, which makes the identification not so clear, as exemplified in the bottom figure in Fig. 5.15.

The proposed CNN method is also applied on the laboratory-controlled experimental data. That turns out to be doable, the structure remaining the same, the mean square error being now equal to 0.0128, yet it needs more epochs (2000) to achieve a stable result. Not all of the testing cases can be well retrieved however, refer to Fig. 5.16; one example that CNN can be not successful is shown at its bottom, for the three missing rods, only two can indeed be identified.

In brief, both the proposed RNN method and CNN method exhibit good performance on the experimental data. The RNN method works better than the CNN one with counting the number of well retrieved cases in the test set, which is agreeing with the results on simulated data.

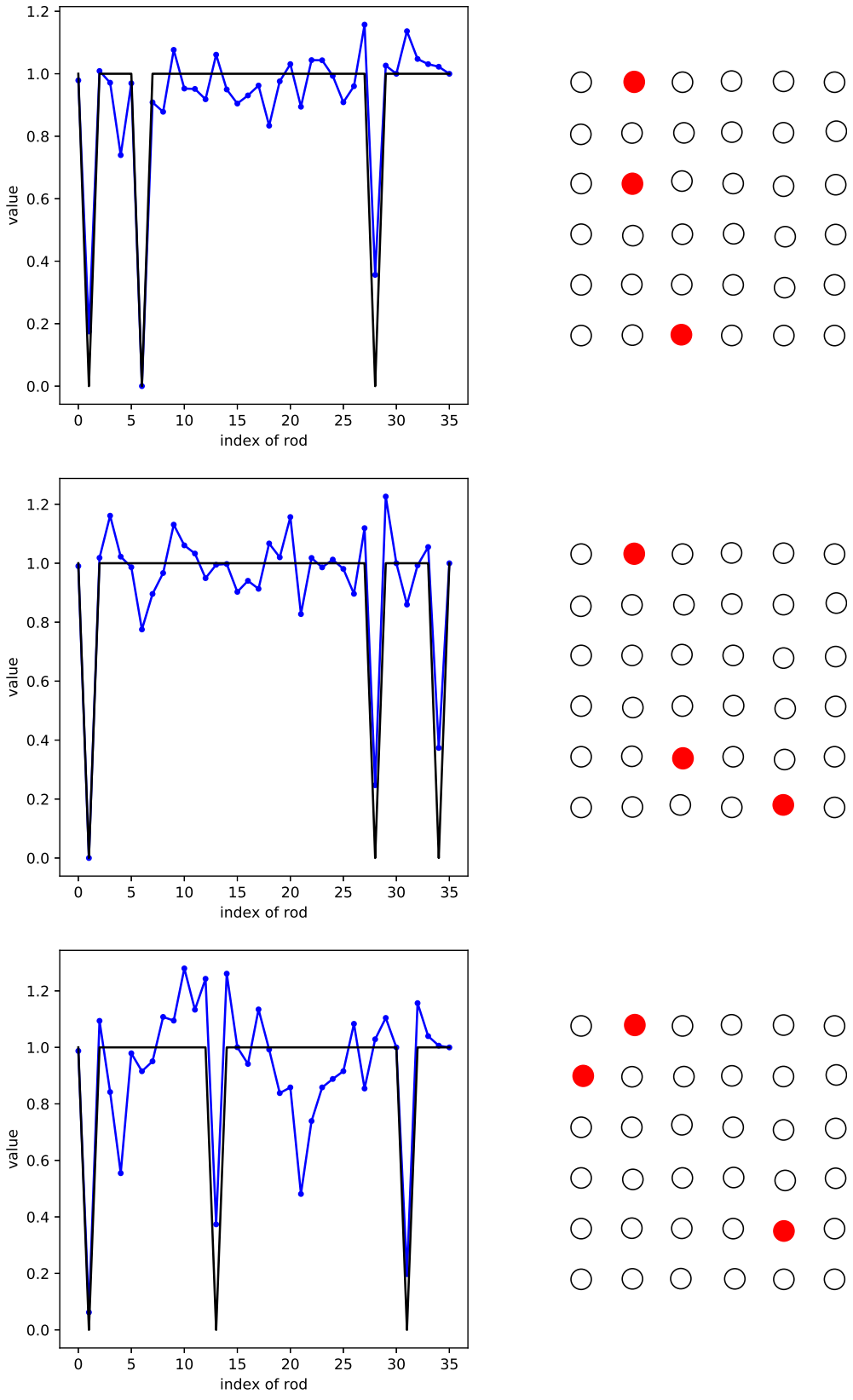

Figure 5.15: LSTM retrievals with experimental data, the black line is the ground truth, the blue line shows the RNN results.

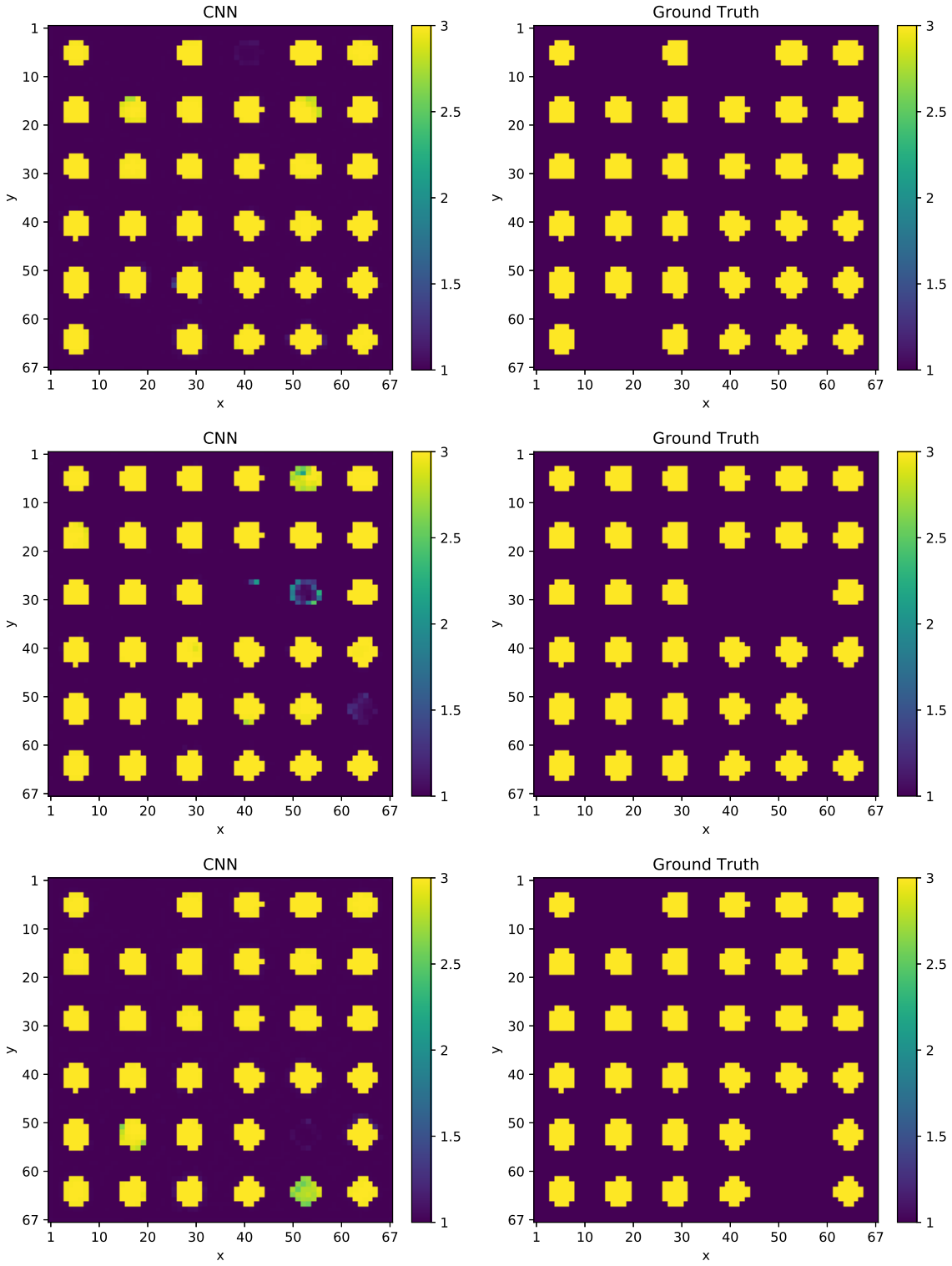

Figure 5.16: CNN retrievals with experimental data, the left part is the ground truth, the right part shows the RNN results, the two upper ones appear as good retrievals, the bottom one as a failed retrieval.

Chapter 6

Imaging by convolutional-recurrent neural networks

As already shown in previous chapters, CNN has strong local modelling capabilities and can extract the features of interest. The idea behind RNN is to make use of sequential information, RNN is recurrent in nature as it performs the same function for every input of data while the output of the current input depends on the past one computation. This proposed approach combines CNN and RNN to take advantage of both of them, and the validation is on the frequency domain data.

6.1 Architecture of proposed CRNN

Fig. 6.1 sketches the proposed frame, denoted from now as CRNN. CNN processes the initial collected field and recognizes the features, RNN uses the known features to make sense of the field and put together a cohesive description, the reconstruction information being shared across the multiple iterations of the said process.

As shown, the input of the structure is the field collected by the 36 receivers when the ROI is illuminated by 36 transmitters at the same distance 7.2λ, and the distance between rod d equals $\lambda/4$ and the radius of rod equals to $\lambda/12$, thus the size of the input is $[36, 36]$. Meanwhile the output is the index of the rods $[2.5, 2.5, 2.5, 1..., 1, 2.5, 1, ...]$, wherein 2.5 represents a normal rod, and 1 represents a missing rod. 3000 examples in total are used to train the network. One example of dataset is shown in Fig. 6.3, the real part of the collected field being the input and the index of rod being the output of the network.

In this structure, four parallel blocks compose the main body, each block containing two convolutional components and one recurrent neural network layer; in each convolutional

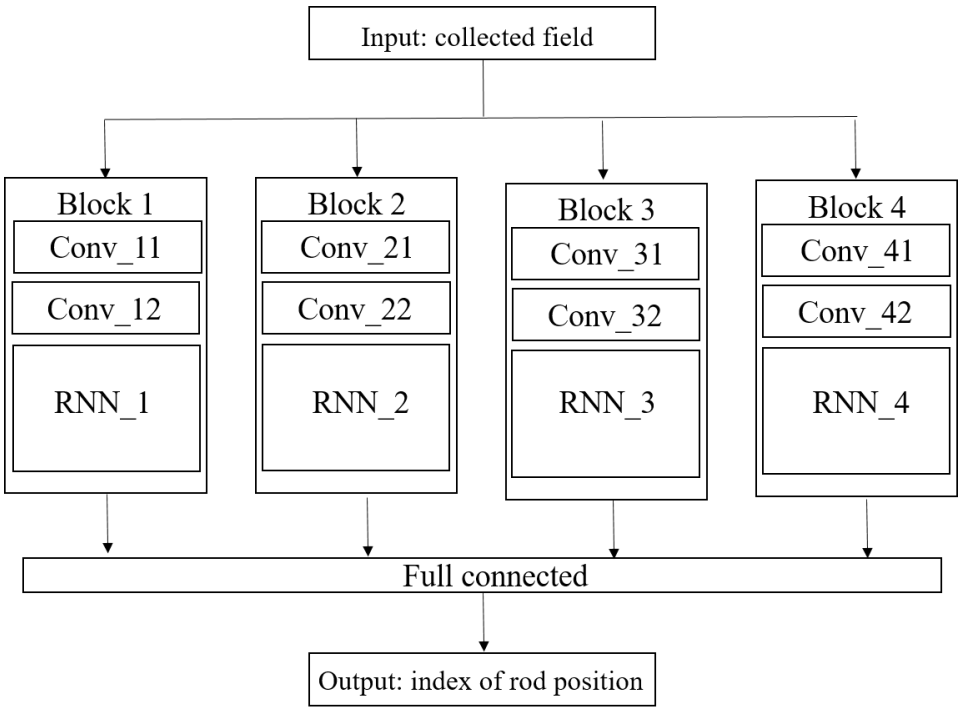

Figure 6.1: Architecture of proposed CRNN structure.

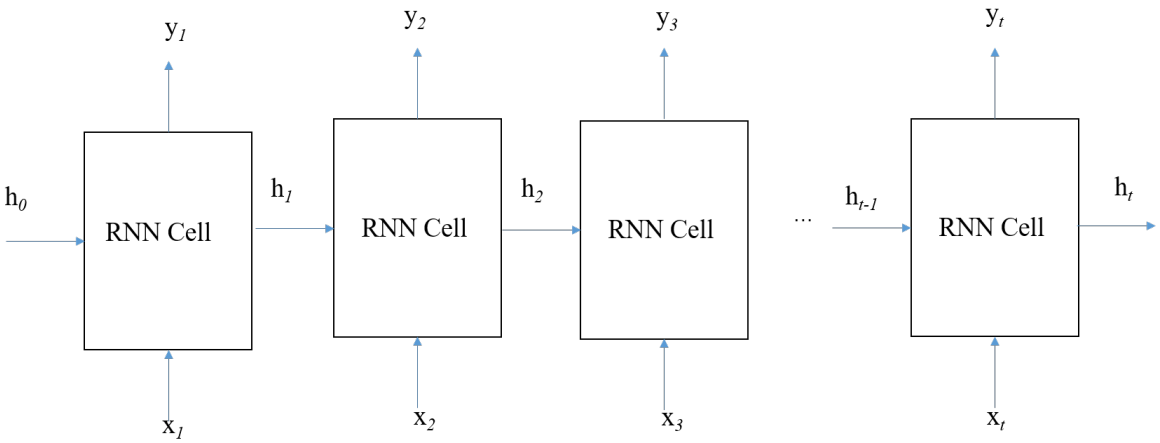

Figure 6.2: Details of RNN layer.

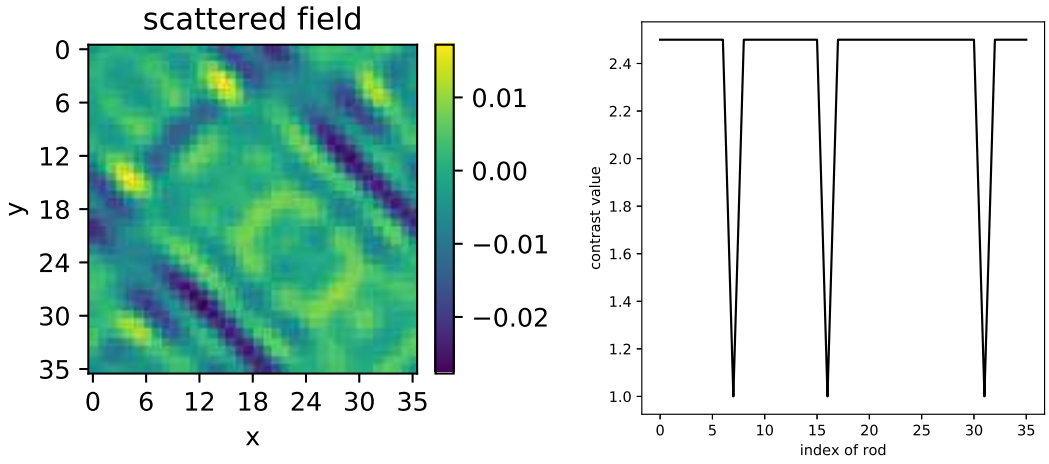

Figure 6.3: Example of dataset.

component, one convolutional layer with batch normalization and ReLU function is applied to achieve feature extraction. Convolutional layer with well chosen kernel size in each block has the ability to extract local features. ReLU, a non-saturated function, is chosen as activation function, applying it to the output of a linear transformation can produce a non-linear transformation. Batch normalization normalizes input and hidden layers by scaling the activations to alleviate the internal covariate shift.

Details of the RNN layer are shown in Fig. 6.2, each RNN layer having 64 cells with the same structure. The input of the RNN is made of the extracted features coming from the convolutional components, and the output is combined with another three outputs from another three blocks. After a linear transform, the output of the structure is the corresponding index of the rod position. As for the choice of the RNN cell, two types are considered: the LSTM and the gated recurrent units (GRU) [48]. The detail of the RNN layer is shown in Fig. 6.2, the t-th cell receives both x_t and the state from last cell h_{t-1}, then produces the h_t for the next cell. The result of the two types yet having been shown of similar performance.

6.2 Training process

The loss function that one henceforth uses is

$$LOSS = \frac{1}{N}\sum_{i=1}^{N} \|\boldsymbol{\epsilon}^i - \hat{\boldsymbol{\epsilon}}^i\|^2, \tag{6.1}$$

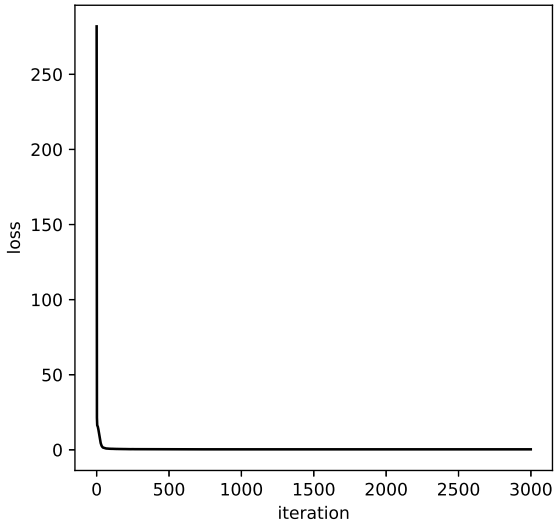

Figure 6.4: Iteration curve during the training.

in which N is the number of samples at each iteration. For the ith sample, $\hat{\boldsymbol{\epsilon}}^i$ and $\boldsymbol{\epsilon}^i$ are the prediction value generated from the RNN and the ground truth, respectively.

The learning algorithm chosen is the ADAM algorithm as the same as for the training in the previous chapters. All the code is realized on the platform Pytorch. Fig. 6.4 shows the iteration curve during training. The GPU NVIDIA Quadro M620 is used, which takes about 35 minutes to perform a training.

6.3 Results of CRNN

Different tests from various configurations of the micro-structure, including the rod shape, to the method of observation, including the frequency and the number of observations, have been carried out in order to validate the performance of the proposed CRNN network.

Two different frequencies: 3 GHz vs 1 GHz

3000 datasets collected at 3 GHz are used to train the network, and 100 examples which are not included in the training set are used to test the performance of the designed network. In Fig. 6.5, three different examples are displayed: 1 missing rod, 2 missing rods and 3 missing rod. The error is 0.0029, where it is defined as mean squared error. For 1 GHz, with the same configuration as for 3 GHz, the error equals 0.0036, which is

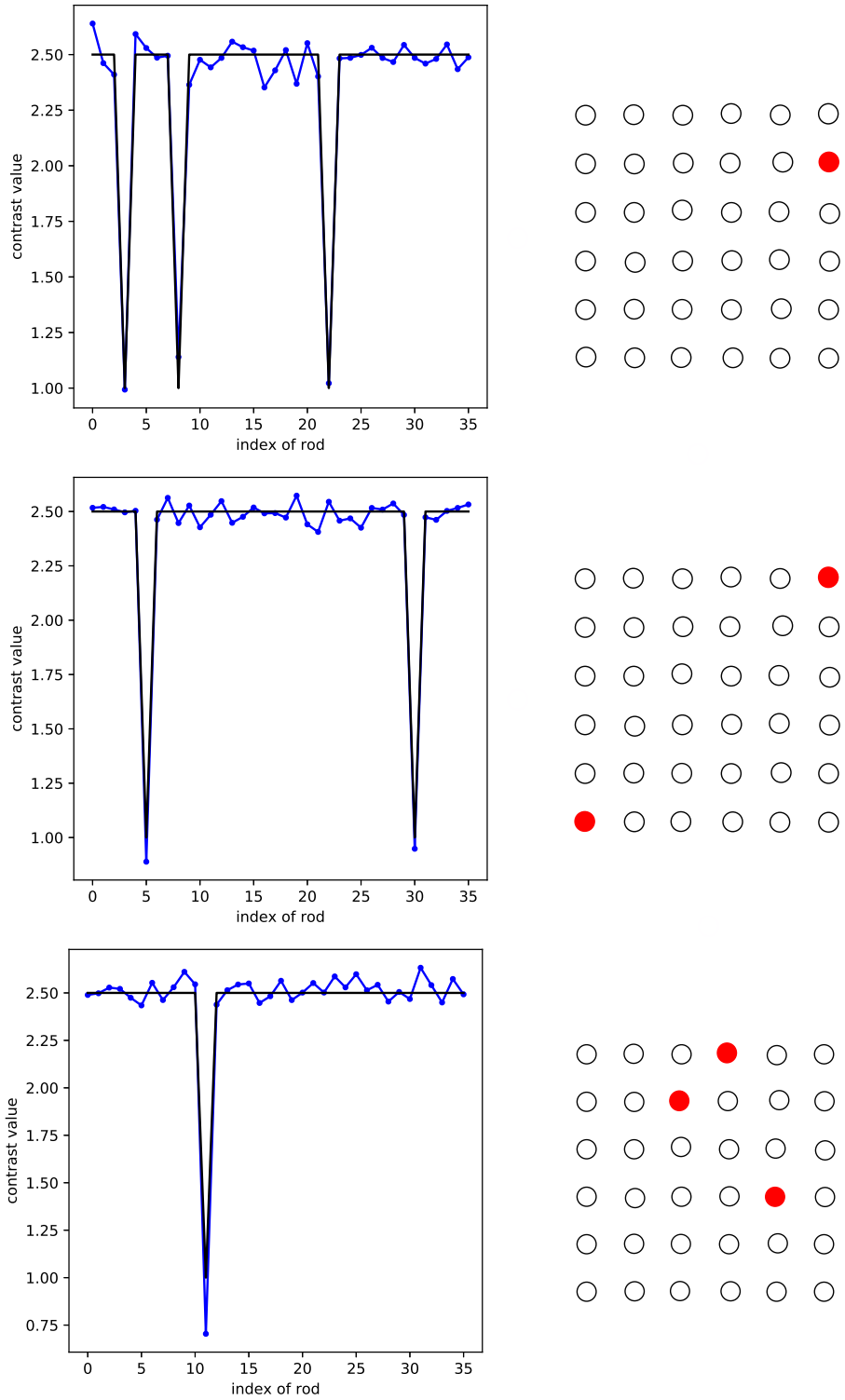

Figure 6.5: CRNN retrievals when 3 GHz, from top to bottom: 1 missing rod, 2 missing rods, 3 missing rods, blue line represents predicted index, black line represents truth index.

larger, compared with 0.0029 when the frequency is 3 GHz, but the CRNN still achieve the correct localization of missing rods.

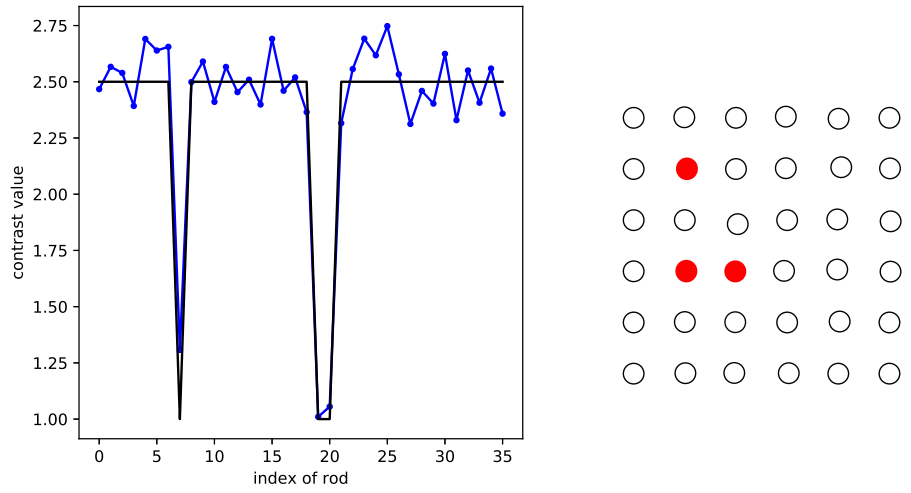

Figure 6.6: CRNN retrieval with less data, blue line represents predicted index, black line represents truth index.

Less transmitters and receivers information

To be in accord with the experiment, one only takes the data that when one transmitter radiates, and that there is only a single receiver that can collect the scattered field, this receiver being directly faced with the transmitter (180 degrees). As a result, in this forward-scattering case, the number of collected field data is quite reduced, from $[36, 36]$ to $[36, 1]$ for each sample. As one can see in the figure, there are larger fluctuations, and the error is increased, yet the index of the missing rods can still be recognized.

Different shape of rod

To illustrate the influence of shape, another training set for a rod with a square shape is used to test the performance, the side length of the square being equated to $\lambda/6$ and the distance between rod still being $\lambda/4$. In Fig. 6.7, identification of missing rod index succeeds well.

Increasing number of missing rods

For now, the maximum missing rod number is limited to 3, to extend the validation, a complementary analysis where the maximum number of missing rods is 5 has been

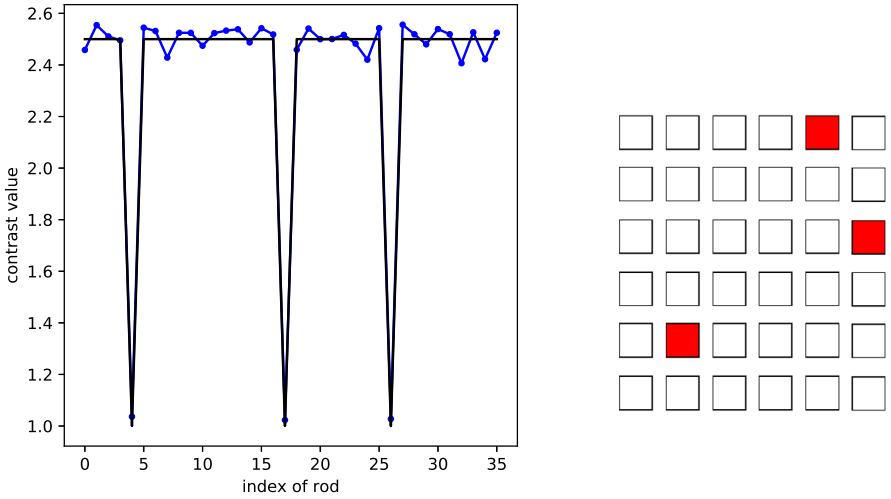

Figure 6.7: CRNN retrieval for square shape rod distribution, blue line represents predicted index, black line represents truth index.

carried out. The condition is the same as before, 3000 examples as training set, another 100 examples as test set, the localization results for different missing rod number is shown in Fig. 6.8, which is still acceptable.

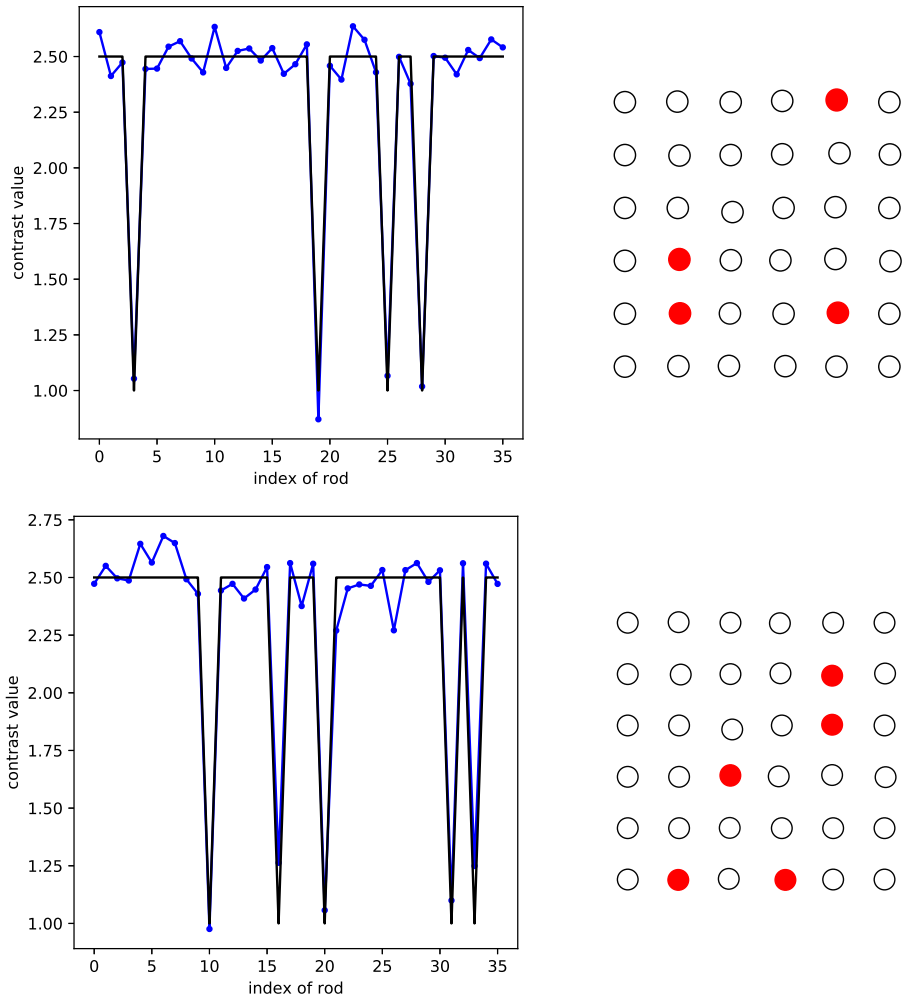

Figure 6.8: CRNN retrieval for 4 (top) and 5 (bottom) missing rods, blue line represents predicted index, black line represents truth index.

Chapter 7

Direct imaging method: time reversal

The imaging methods from CSI, sparsity constrained-method to neural networks learning methods introduced in the previous chapters are developed from the concept of inverse scattering problem, that is, the reconstruction of the ROI from the collected field. In this chapter a direct imaging method is introduced to tackle the problem of refocusing of a source, and localization of a missing rod in the micro-structure. Time reversal (TR) is realized by time reversal mirror (TMR), which records an incoming wave and then re-transmits its time-reversed version, the field distribution in the ROI illuminated by the reversed signal should indicate the location of the source or of the missing rods. The basic principle of time-reversal is from geometrical optics, as the functionality of mirror, the received signal is sent back along the original path to yield an image at the position of the original object. TR can be carried out in time domain and in frequency domain, the localization of active source by TR is implemented in the frequency domain, and the localization of missing rods by TR is carried out in the time domain, the constraint of sub-wavelength is maintained.

7.1 Time reversal for localization of source

The procedure of time reversal is shown in Fig. 7.1, e.g., [29], the signal received by the TRM is inverted in the time domain and re-emitted again [49]. TR invariance means that result of equation remains unchanged under a TR transformation $T : t \mapsto -t$ [40]. For a scalar wave

$$\bigtriangledown^2 u(r,t) - \frac{1}{v^2(r)} \frac{\partial^2 u(r,t)}{\partial t^2} = 0, \tag{7.1}$$

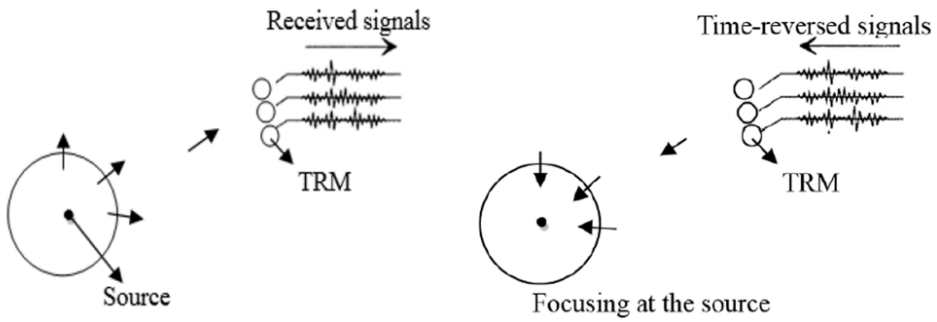

Figure 7.1: Procedure of time reversal.

$u(r,t)$ is even under TR transformation $Tu(r,t) = u(r,-t)$ since the wave equation only contains an even order time-derivative operator, the Fourier transform of the real-valued signal $u(r,t)$ is

$$u(r,w) = \frac{1}{2\pi}\int_{-\infty}^{\infty} u(r,t)e^{-iwt}dt, \tag{7.2}$$

implies $u(r,-w) = u^*(r,w)$, where superscript $*$ denotes complex conjugation. So TR is simply equivalent to phase conjugation of every frequency component $Tu(r,w) = u^*(r,w)$.

In the simulation proposed here as illustration, 36 TRM are regularly set around the structure at a distance D, $D = 100d$, different D are tried, more details can be found in Appendix D. TR imaging is implemented according to two mains steps. First, the TRM receives the outgoing fields radiated from the source inside or outside the structure. Second, it carries out the phase conjugation of the obtained fields in the frequency domain, then re-transmits its time-reversed version. The re-transmitted wave propagates back through the same structure and is expected, as already indicated, to refocus at the location of the original source.

2-D and 3-D maps of TR are shown in Fig. 7.2. There are three different cases being considered, from top to bottom: the source is at the center of structure, at position $(-3d,-3d)$, and at position $(-10d,0)$, which in this latter case means that the source is outside of structure. One sees that TR can achieve a good solution no matter where the sought-after source is located.

Although refocalization is realized in both TM and TE cases, considering for the enhancement of resolution, Fig. 7.3 illustrates that as the relative rod permittivity is increased, the resolution is enhanced in the TM case, yet there is no enhancement whatsoever in the TE case. The difference of resolution enhancement between TE and TM cases can be explained by homogenization formulas (without elaborating further,

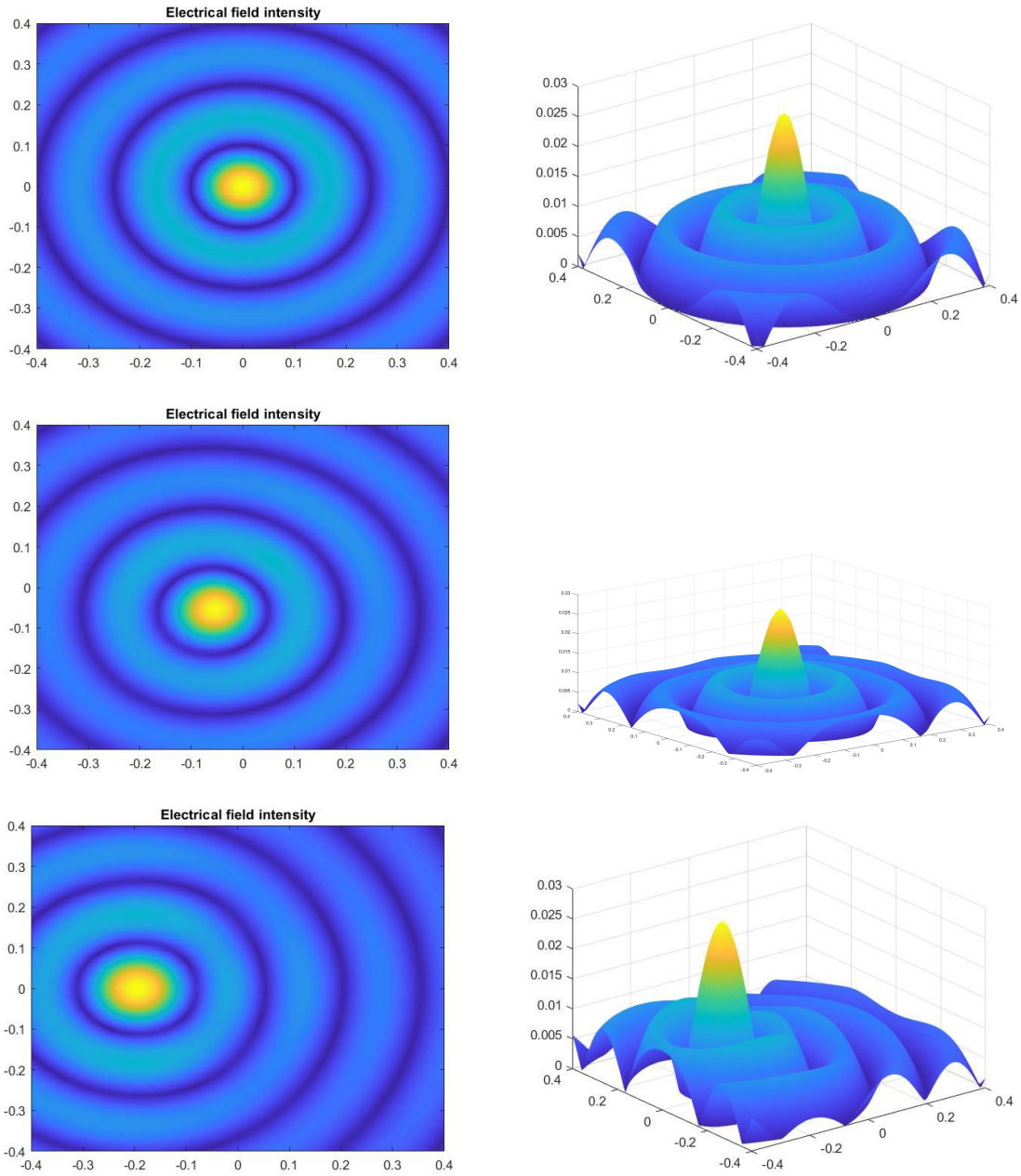

Figure 7.2: 2D and 3D representations of the time-reversed field for three different source locations within a $20d \times 20d$ box.

this holds if one has a large number of small enough rods of not too high contrast within the structured system, and no resonances occurring inside) [50].

Those read as

$$\bar{\epsilon}_{TM} = \frac{\epsilon_1 S_1 + \epsilon_2 S_2}{S_1 + S_2}, \quad \bar{\epsilon}_{TE} = \frac{S_1 + S_2}{S_1/\epsilon_1 + S_2/\epsilon_2}, \tag{7.3}$$

$\bar{\epsilon}_{TM}$, $\bar{\epsilon}_{TE}$ effective permittivities, S_1 cross-sectional rod area, S_2 elementary cell area, which is shown in Fig. 7.4, ϵ_1 and ϵ_2 permittivities in S_1 and S_2.

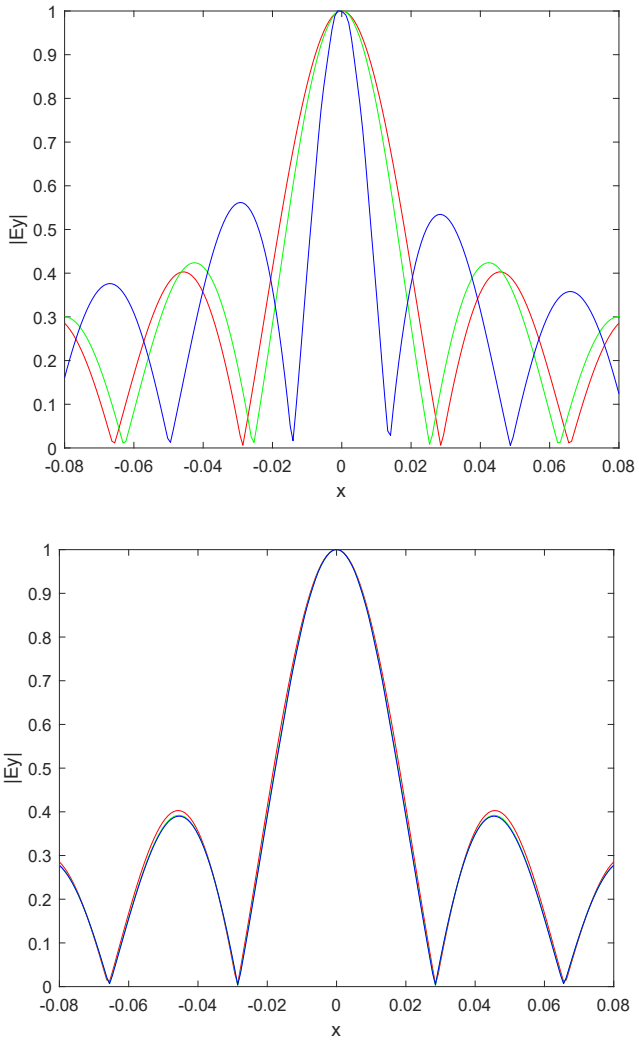

Figure 7.3: Enhancement of resolution, source at center, cross-section along the horizontal axis passing by it, as function of rod permittivity $\epsilon_r = 1$ (no rod) (red), 10 (green) and 100 (blue), Top: TM case, bottom: TE case.

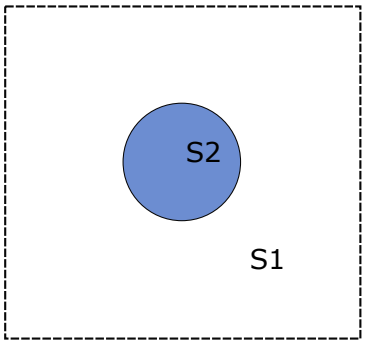

Figure 7.4: Elementary cell of the system, illustration of areas S_1 and S_2.

7.2 Time Reversal for localization of missing rods

Unlike the refocalization of source, the localization of missing rods in structure by TR is carried in time domain. The missing rod is regarded as the passive source, since scattered fields generated by the passive source can be considered as the radiated field by an equivalent source.

The collected field is also computed by using gprMax as was the case in the previous section, a ROI with length 0.8 m along X axis, length 0.8 m along Y axis, is meshed with step of 0.002 into each direction for simulation. The procedure of time reversal in the time domain is sketched in Fig. 7.5: transmitters send out a signal one by one, receivers collect the field reflected by the micro-structure, the collected field is reversed as shown in Fig. 7.6, then the reversed signal is re-emitted onto the ROI, and from the field distribution, the position of missing rod is easy to tell. In Fig. 7.6, the left part is

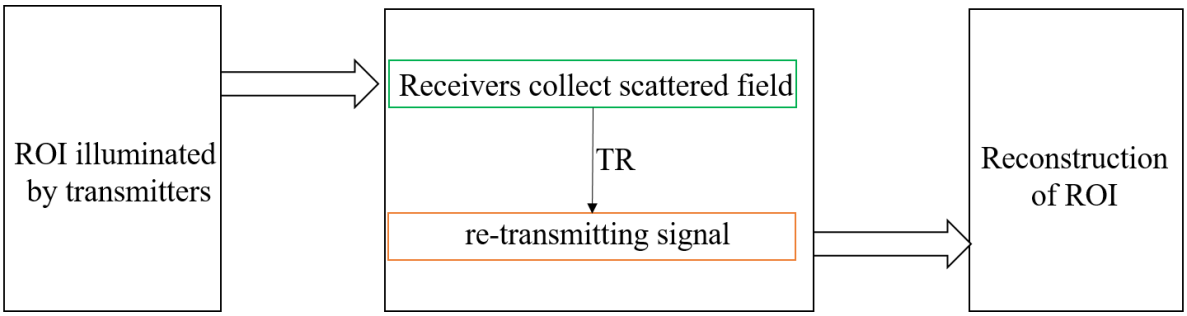

Figure 7.5: Illustration of Time Reversal procedure

the signal received by one receiver, and the right part is the signal already reversed and ready to be sent out. There are 3181 time steps in each signal.

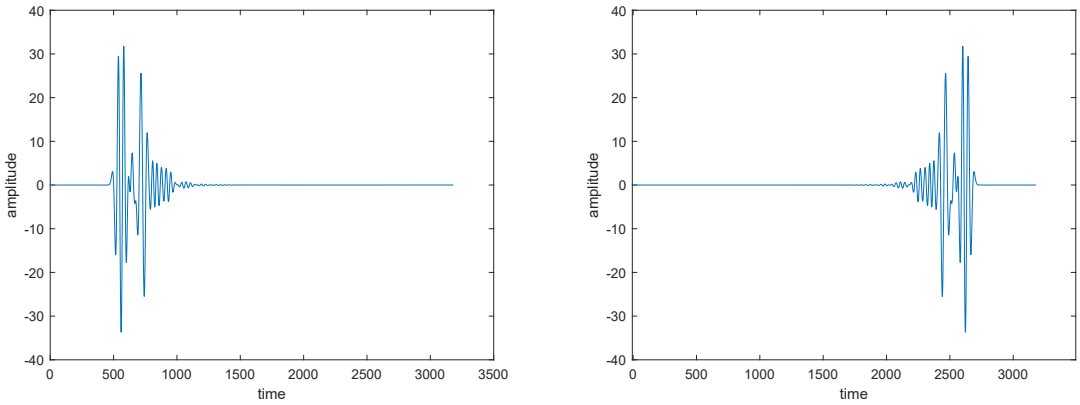

Figure 7.6: Illustration of Time Reversal of one position

As seen in Fig. 7.7, time reversal can realize the localization of missing rods indeed. From the results, the index of missing rods in first one is $[11, 27, 35]$, the second one is $[13, 15, 20]$, the third one is $[7, 11, 30]$, the last one is $[8, 15, 20]$. While there is one fact that one needs to admit, from the left bottom image, it is hard to tell if the exact localization is 11 or 12, which should be improved in further.

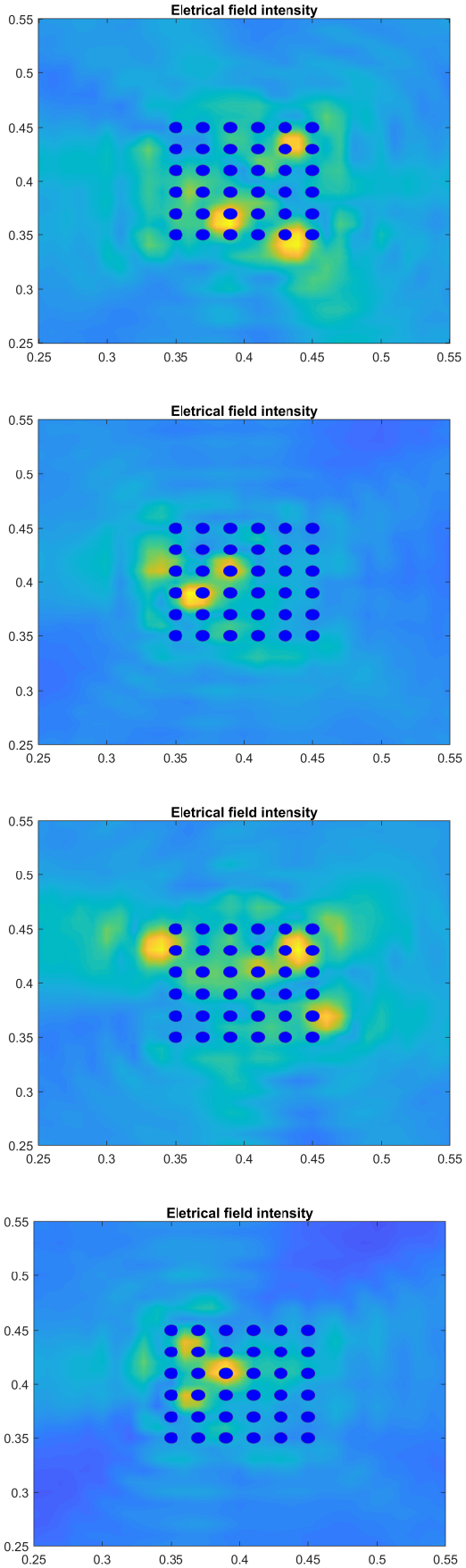

Figure 7.7: Examples of time reversal result

Chapter 8

Conclusion

8.1 Summary of the work as completed

The investigation of a damaged or missing-rod distribution of circular cylindrical dielectric rods which exhibit sub-wavelength-sized diameters and inter-element distances has been conducted according to different situations. To probe the micro-structure, the work is mainly divided into two parts, the forward problem and the inverse problem. For the forward one, methods from method of moments to multiple scattering method to FDTD, are used to carry out the mathematical modelling of the problem, while the inverse problem is solved from analytical methods, contrast source inversion to joint-sparsity to learning method, including CNN, RNN and so on.

From another point of view, the problem can also be divided by the processing domain: frequency domain and time domain, the analysis of signal in different spaces indeed could explore specialized features. The multiple scattering method and the method of moments are constructed in the frequency domain, and the corresponding joint-sparsity method and the CSI method are developed in the same frequency domain. In contrast, the FDTD method carries out the modelling in the time domain, and the RNN is tailored to the processing of time sequence data. As for time reversal, it is an imaging method directly used in time domain, yet it involves also, from conjugation, frequency domain data. To be mentioned, the transformation of signal between time domain and frequency domain is obvious a way to go, and it can be carried out if in need. The Table shown below attempts to clarify the aforementioned methods.

The performance of different methods cannot be judged according to a simple criterion, they are advantages and disadvantages considering the standing issue. The closed form methods need a good knowledge of physics and maths, they are hard to understand if that knowledge is not available. On the other side, large amounts of data are the premise

Direct Modelling methods	Imaging methods
Method of moments (frequency domain)	Contrast source inversion (closed-form method)
	Convolutional neural networks (learning method)
FDTD (time domain)	Time reversal (closed-form method)
	Recurrent neural networks (learning method)
Multiple scattering method(frequency domain)	Joint-sparsity method (closed-form method)

Figure 8.1: Table of used methods.

of the usage of learning methods, yet the performance cannot be guaranteed. The deep learning method is to a good extent like a black box, many people try to get further explanation of deep learning [26]; as with the high no-linearity of modelling capability of CNN, the RNN is a good approximation of time sequence. As for the method that one could say as being experimental physics, time reversal exhibits a good performance not only for the inverse source problem but also for the inverse scattering problem, being underlined that the only issue of time reversal is that the resolution of the result is not high enough, as expected from previous work.

In another side, the applicability of the methods is a matter of concern. The joint-sparsity method cannot be transferred easily in order to deal with other problems because of the specialized mathematical analysis of the modelling. In contrast, the learning methods suffer less from this kind of limitation, to say, the CNN or RNN methods have a higher prospect to apply to similar problems. To be more specific, with a well-trained network, only tasks like tuning parameters or modifications of some layers are required to adapt them to other different micro-structures in terms of contrast, number, size and inter-distance of the rods, and different measurement configurations as well.

The binary case and the random case are both analysed in the present research, the binary case is for the localization of missing rods, and the random contrast case can be extended to the general cases for object reconstruction to get the exact physical parameters, like permittivity here. Different values and different shapes are also developed in this research to this kind of extension.

8.2 Potential work

Although the sub-wavelength micro-structure has been analysed by various methods from the modelling to the imaging and diagnostic problem, further explorations are of good interest.

First of all, the research so far as proposed is still limited to two-dimensional and quasi two-dimensional situations, to go to full three dimensions is still something to investigate, once noted that the three-dimensional problem is more difficult both in terms of the mathematical modelling and of the inverse problem itself.

Other remaining works are about the experimental part, the correction between the simulation and experiment data, using a method like Generative Adversarial Network (GAN) [51], or further WGAN [52], to generate the simulated data in order to avoid the time-consuming manual experiments. GAN consists of two models: A discriminator D estimates the probability of a given sample coming from the real dataset. It works as a critic and is optimized to discriminate the fake samples from the real ones. A generator G outputs synthetic samples given a noise variable input z (z brings in potential output diversity). It is trained to capture the real data distribution so that its generative samples can be as real as possible, or in other words, can trick the discriminator to offer a high probability. Otherwise, using the proposed analytical and learning methods to process the experimental data directly is another possible solution. GAN has been applied to solve the electromagnetic scattering problem in some pioneer researcher's work [53].

Except for directly applying the neural networks to process the data, the combination of physics and neural networks is a path ahead. Much work has been done by others, for example, for the similar inverse scattering problem, a back-propagation method is used first to transfer the electrical field into a rough contrast map, then the contrast map instead of the scattered field is used as the input of the U-net architecture. In [54], the DNN is integrated into the CSI to achieve further improvement. As insisted upon already, [28] explains the relationship between wave equation and RNN, which provides a quite sharp idea for the research based on a wave equation. It turns out that the combination of closed-form method and learning method can benefit from the physical background and the potential of big data. A deep image prior is analysed to solve the inverse problem [55], the deep image prior approach in combination with classical regularization can overcome the problem of the lack of generalization after training with insufficient data [56].

The fusion of data from different imaging methods can take advantage of different behaviours. Fusion of ultrasound and microwave could provide a new sort of solution [57], which may not apply to micro-structures as in this research, but in many cases of inverse

scattering it remains a good option. For example, ultrasound imaging yielding a contour of the object, which would be further used as the prior information for the microwave imaging. In [58], microwave breast imaging is investigated with a priori information on tissue boundaries yielded from ultrasound reflection data. Fusion methods are various, the Bayesian method benefits from a good reputation and surely has achieved fruitful accomplishments since a long time. The learning method gathers the data from different models in multiple channels of the dataset, so that the neural networks can learn the data to realize different purposes from the information of these channels.

Appendix A

Graf's addition theorem

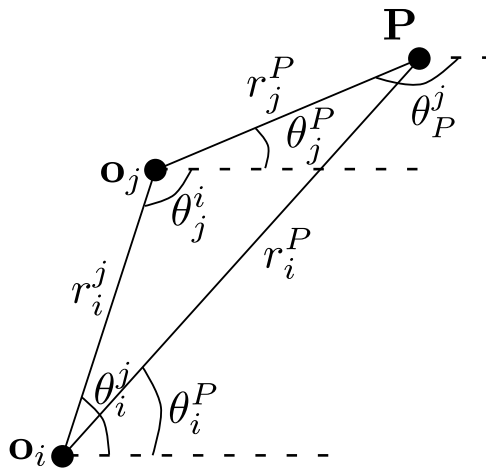

Figure A.1: Application of the Graf's addition theorem.

Fields near a rod are expanded into cylindrical waves and the resulting expression is based on the local coordinate system originated at the rod center. However, in the analysis of rod array, expressing the field in the local coordinate system of another rod is often required. The Graf's addition theorem is used to make this transformation.

As sketched in Fig. A.1, $\mathbf{o}_i$ and $\mathbf{o}_j$ are centers of two rods and $\mathbf{P}$ is the observation position. The distances between them satisfy $r_j^P < r_i^j < r_i^P$.

Assume the field value at $\mathbf{P}$ is with expression

$$V(\mathbf{P}) = H_m^{(1)}(kr_i^P)e^{im\theta_i^P}, \tag{A.1}$$

where (r_i^P, θ_i^P) are polar coordinates of $\mathbf{P}$ in the local coordinate system originated at $\mathbf{o}_i$. With condition $r_j^P < r_i^j$, (A.1) can be transformed into an equation expressed in the

coordinate system associated with $\mathbf{o}_j$, as

$$V(\mathbf{P}) = \sum_{n\in\mathbb{Z}} H_{m-n}(kr_i^j)e^{i(m-n)\theta_i^j} J_n(kr_j^P)e^{in\theta_j^P}. \tag{A.2}$$

Another form of (A.2) using θ_j^i, instead of θ_i^j, is given as

$$V(\mathbf{P}) = \sum_{n\in\mathbb{Z}} H_{n-m}(kr_i^j)e^{i(m-n)\theta_j^i} J_n(kr_j^P)e^{in\theta_j^P}. \tag{A.3}$$

We assume the field value at $\mathbf{P}$ is with expression

$$V(\mathbf{P}) = H_m^{(1)}(kr_j^P)e^{im\theta_j^P}, \tag{A.4}$$

and are trying to transform the expression into the one in the coordinate system originated at $\mathbf{o}_i$. Since $r_i^P > r_i^j$, the above procedures cannot be operated and an alternative way applying the Graf's addition theorem is developed.

Making use of the identity $H_m^{(1)}(kr_j^P)e^{im\theta_j^P} = (-1)^m H_m^{(1)}(kr_j^P)e^{im\theta_P^j}$, V is expressed in the coordinate system originated at $\mathbf{P}$. Applying the Graf's addition theorem with condition $r_i^P > r_i^j$, we have

$$\begin{aligned} H_m^{(1)}(kr_j^P)e^{im\theta_j^P} &= (-1)^m \sum_{n\in\mathbb{Z}} H_{n-m}(kr_i^P)e^{i(m-n)\theta_i^P} J_n(kr_i^j)e^{in\theta_i^j} \\ &= \sum_{n\in\mathbb{Z}} H_{m+n}(kr_i^P)e^{i(m+n)\theta_i^P} J_n(kr_i^j)e^{-in\theta_i^j} \\ &= \sum_{n\in\mathbb{Z}} J_{n-m}(kr_i^j)e^{i(m-n)\theta_i^j} H_n(kr_i^P)e^{in\theta_i^P}, \end{aligned} \tag{A.5}$$

which is the expression of V in the coordinate system about $\mathbf{o}_i$.

Appendix B

The Lippman-Schwinger formulation

Assume that $\mathbf{E}(\mathbf{r})$ is the electric field by the well-organized structure (which means they are no defects) at the point $\mathbf{r}$. According to the Helmholtz equation,

$$\bigtriangledown \times \bigtriangledown \times \mathbf{E}(\mathbf{r}) - k^2(\mathbf{r})\mathbf{E}(\mathbf{r}) = 0 \tag{B.1}$$

Similarly, the field corresponding to disorganized structure (now, with missing rods) $\widetilde{\mathbf{E}}(\mathbf{r})$ satisfies

$$\bigtriangledown \times \bigtriangledown \times \widetilde{\mathbf{E}}(\mathbf{r}) - \widetilde{k}^2(\mathbf{r})\widetilde{\mathbf{E}}(\mathbf{r}) = 0 \tag{B.2}$$

so the subtraction of the two equations,

$$\begin{aligned} &\bigtriangledown \times \bigtriangledown \times (\widetilde{\mathbf{E}}(\mathbf{r}) - \mathbf{E}(\mathbf{r})) - \widetilde{k}^2(\mathbf{r})\widetilde{\mathbf{E}}(\mathbf{r}) - k^2(\mathbf{r})\mathbf{E}(\mathbf{r}) \\ &= \bigtriangledown \times \bigtriangledown \times (\widetilde{\mathbf{E}}(\mathbf{r}) - \mathbf{E}(\mathbf{r})) - k^2(\mathbf{r})(\widetilde{\mathbf{E}}(\mathbf{r}) - \mathbf{E}(\mathbf{r})) - (\widetilde{k}^2(\mathbf{r}) - k^2(\mathbf{r}))\widetilde{\mathbf{E}}(\mathbf{r}) = 0 \end{aligned} \tag{B.3}$$

Let $\mathbf{y}(\mathbf{r}) = \widetilde{\mathbf{E}}(\mathbf{r}) - \mathbf{E}(\mathbf{r})$, then

$$\bigtriangledown \times \bigtriangledown \times \mathbf{y}(\mathbf{r}) - k^2((r))\mathbf{y}(\mathbf{r}) = (\widetilde{k}^2(\mathbf{r}) - k^2(\mathbf{r}))\widetilde{\mathbf{E}}(\mathbf{r}) \tag{B.4}$$

According to the definition of the Green function $\mathbf{G}(\mathbf{r})$,

$$\bigtriangledown \times \bigtriangledown \times \mathbf{G}(\mathbf{r}, \mathbf{r}') - k^2(\mathbf{r})\mathbf{G}(\mathbf{r}, \mathbf{r}') = \delta(\mathbf{r} - \mathbf{r}') \tag{B.5}$$

then $\mathbf{y}(\mathbf{r})$ can be written as

$$\mathbf{y}(\mathbf{r}) = \int \mathbf{G}(\mathbf{r}, \mathbf{r}')(\widetilde{k}^2(\mathbf{r}') - k^2(\mathbf{r}'))\widetilde{\mathbf{E}}(\mathbf{r}')d\mathbf{r}' \tag{B.6}$$

Assume that there are P missing rods, then, expect for the surface area of these P rods, $\widetilde{k}^2(\mathbf{r}') - k^2(\mathbf{r}') = 0$. so

$$\mathbf{y}(\mathbf{r}) = \sum_{p=1}^{P} \int_{D_p} \mathbf{G}(\mathbf{r}, \mathbf{r}')(\widetilde{k}^2(\mathbf{r}') - k^2(\mathbf{r}'))\widetilde{\mathbf{E}}(\mathbf{r}')d\mathbf{r}' \tag{B.7}$$

D_p is the surface area of the p-th missing rod.

Appendix C

Further complementary material on time reversal I

In the contribution —H. Tu, M. Serhir, P. Ran, and D. Lesselier, On the modeling and diagnosis of a micro-structured wire antenna system, *2018 International Conference on Microwave and Millimeter Wave Technology (ICMMT)*, Chengdu, May 2018. IEEE Conference Publication no. 8563875 (3 pp), Dec. 2018— that I delivered as a poster in the ICMMT conference, a 3-D full-wave configuration, supported by laboratory experiments on a properly built previous prototype in a microwave anechoic chamber, has been discussed in depth from simulated and experimental data: short monopole wire antennas apart by a small fraction of the operation wavelength are inserted within a finite set of regularly distributed, shorter thin metal wires also apart similarly, and the monopole that radiates must be found from far field patterns (those exhibit sharp changes versus the position of the radiator in the frequency band associated to resonances).

The investigation has not be pursued beyond 2018, as focus shifted to 2-D cases and dielectric micro-structures, yet this remains of good interest, as moving up to 3-D cases of dielectric micro-structures is one of the proposed paths of investigation, and experimental challenges of the same order should be faced with, while the fact that they may exhibit resonances of some sort, even if less obvious than as with the metal wire system, is also to be appraised further.

Notice that elements of the above have been orally given in September 2018 upon invitation at a Workshop in Singapore by D. Lesselier —Z. Liu, P. Ran, Y. Zhong, M. Serhir, and D. Lesselier, Computational imaging of micro-structured media at small scale - from one-shot first-order solutions to full-wave iterative ones, *Workshop on Qualitative and Quantitative Approaches to Inverse Scattering Problems, Institute for Mathematical Sciences, National University of Singapore*, Singapore, Sept. 2018.

Emphasize that no specific Chapter of the present PhD manuscript is associated to the issue, as seen somewhat aside the main investigation, yet brief comments in Introduction and Conclusion are made about it.

Appendix D

Further complementary material on time reversal II

The work about time reversal for a source and for missing rods is carried out at different stages of the present research, and if some parameters of the configuration are not identical, the condition of sub-wavelength geometries is always maintained. To be more specific, whenever preoccupied with time reversal for the active source, different distances D from the center of the structure to the observation point are used, including the 7.2λ which is the same as with the configuration for the investigation about the localization of missing rods, and also 20λ which is the original setting. Size of the radius of rod c has an influence on the performance of localization of the active source, that is, when c is as small as $\lambda/20$, which is the original setting of the configuration, the localization accuracy is high enough, while when c becomes larger, the accuracy of the localization reduces, —to be mentioned, all the discussion is under the assumption of an operating frequency as of 3 GHz.

Bibliography

[1] H. Ammari, J. Garnier, W. Jing, H. Kang, M. Lim, K. Sølna, and H. Wang, *Mathematical and Statistical Methods for Multistatic Imaging*. Springer, 2013.

[2] H. Ammari, E. Bonnetier, and Y. Capdeboscq, "Enhanced resolution in structured media," *SIAM Journal on Applied Mathematics*, vol. 70, no. 5, pp. 1428–1452, 2009.

[3] Z. Liu, D. Lesselier, and Y. Zhong, "Electromagnetic imaging of damages in fibered layered laminates via equivalence theory," *IEEE Transactions on Computational Imaging*, vol. 4, no. 2, pp. 219–227, 2018.

[4] H. Tu, M. Serhir, P. Ran, and D. Lesselier, "On the modeling and diagnosis of a micro-structured wire antenna system," in *2018 International Conference on Microwave and Millimeter Wave Technology (ICMMT), IEEE Conference Publication*, (Chengdu), p. 8563875, 2018.

[5] L. C. Botten, N.-A. P. Nicorovici, A. A. Asatryan, R. C. McPhedran, C. M. de Sterke, and P. A. Robinson, "Formulation for electromagnetic scattering and propagation through grating stacks of metallic and dielectric cylinders for photonic crystal calculations. part I. Method," *Journal of the Optical Society of America A*, vol. 17, no. 12, pp. 2165–2176, 2000.

[6] L. C. Botten, N.-A. P. Nicorovici, A. A. Asatryan, R. C. McPhedran, C. M. de Sterke, and P. A. Robinson, "Formulation for electromagnetic scattering and propagation through grating stacks of metallic and dielectric cylinders for photonic crystal calculations. part II. Properties and implementation," *Journal of the Optical Society of America A*, vol. 17, no. 12, pp. 2177–2190, 2000.

[7] D. Maystre, "Electromagnetic scattering by a set of objects: an integral method based on scattering operator," *Progress In Electromagnetics Research*, vol. 57, pp. 55–84, 2006.

[8] D. S. Jones, "Field computation by moment methods," *The Computer Journal*, vol. 12, p. 37, Feb 1969.

[9] C. Warren, A. Giannopoulos, and I. Giannakis, "gprmax: Open source software to simulate electromagnetic wave propagation for ground penetrating radar," *Computer Physics Communications*, vol. 209, pp. 163 – 170, 2016.

[10] H. Zaimaga, A. Fraysse, and M. Lambert, "Sparse reconstruction algorithms for nonlinear microwave imaging," in *2017 25th European Signal Processing Conference (EUSIPCO)*, pp. 713–717, 2017.

[11] H. Zaimaga, *Sparsity and Electromagnetic Imaging in Non-Linear Situations*. PhD thesis, University Paris-Sud University Paris-Saclay, Dec 2017.

[12] A. Hiles and O. Dorn, "Sparsity and level set regularization for near-field electromagnetic imaging in 3D," *Inverse Problems*, vol. 36, no. 2, 2020.

[13] Z. Liu, *Electromagnetic Modeling and Simulation of Fiber-Reinforced Periodically-Structured Planar Laminates*. PhD thesis, University Paris-Sud University Paris-Saclay, Oct 2017.

[14] I. T. Rekanos, "Neural-network-based inverse-scattering technique for online microwave medical imaging," *IEEE Transactions on Magnetics*, vol. 38, no. 2, pp. 1061–1064, 2002.

[15] S. Caorsi and P. Gamba, "Electromagnetic detection of dielectric cylinders by a neural network approach," *IEEE Transactions on Geoscience and Remote Sensing*, vol. 37, no. 2, pp. 820–827, 1999.

[16] I. Goodfellow, Y. Bengio, and A. Courville, *Deep Learning*. MIT Press, 2016. http://www.deeplearningbook.org.

[17] K. Cho, B. van Merrienboer, Ç. Gülçehre, F. Bougares, H. Schwenk, and Y. Bengio, "Learning phrase representations using RNN encoder-decoder for statistical machine translation," *CoRR*, vol. abs/1406.1078, 2014.

[18] T. Mikolov, S. Kombrink, L. Burget, J. Černocký, and S. Khudanpur, "Extensions of recurrent neural network language model," in *Proceedings of the 2011 IEEE International Conference on Acoustics, Speech and Signal Processing (ICASSP)*, pp. 5528–5531, 2011.

[19] A. Lucas, M. Iliadis, R. Molina, and A. K. Katsaggelos, "Using deep neural networks for inverse problems in imaging: Beyond analytical methods," *IEEE Signal Processing Magazine*, vol. 35, no. 1, pp. 20–36, 2018.

[20] A. Massa, D. Marcantonio, X. Chen, M. Li, and M. Salucci, "DNNs as applied to electromagnetics, antennas, and propagation—a review," *IEEE Antennas and Wireless Propagation Letters*, vol. 18, no. 11, pp. 2225–2229, 2019.

[21] Z. Xiang, A. Rashidi, and G. Ou, "An improved convolutional neural network system for automatically detecting rebar in GPR data," *CoRR*, vol. abs/1907.09997, 2019.

[22] X. L. Travassos, S. L. Avila, and N. Ida, "Artificial neural networks and machine learning techniques applied to ground penetrating radar: A review," *Applied Computing and Informatics*, Jul 2020.

[23] Y.-t. Chen, K. Ishitsuka, S. Iso, K. Onishi, and T. Matsuoka, "Object detection in ground-penetrating radar images using a deep convolutional neural network and image set preparation by migration," *International Journal of Geophysics*, vol. 2018, p. 9365184, 2018.

[24] L. Cui, Y. Zhang, R. Zhang, and Q. H. Liu, "A modified efficient KNN method for antenna optimization and design," *IEEE Transactions on Antennas and Propagation*, vol. 68, no. 10, pp. 6856–6866, 2020.

[25] J. Nagawkar, L. Leifsson, R. Miorelli, and P. Calmon, "Model-based sensitivity analysis of nondestructive testing systems using machine learning algorithms," in *Computational Science – ICCS 2020* (V. V. Krzhizhanovskaya, G. Závodszky, M. H. Lees, J. J. Dongarra, P. M. A. Sloot, S. Brissos, and J. Teixeira, eds.), (Cham), pp. 71–83, Springer International Publishing, 2020.

[26] S. Arridge, M. de Hoop, P. Maass, O. Öktem, C. Schönlieb, and C. Uns, "Deep learning and inverse problems," 2019.

[27] C. Qin, J. Schlemper, J. Caballero, A. N. Price, J. V. Hajnal, and D. Rueckert, "Convolutional recurrent neural networks for dynamic MR image reconstruction," *IEEE Transactions on Medical Imaging*, vol. 38, no. 1, pp. 280–290, 2019.

[28] T. W. Hughes, I. A. D. Williamson, M. Minkov, and S. Fan, "Wave physics as an analog recurrent neural network," *Science Advances*, vol. 5, no. 12, 2019.

[29] R. Pierrat, C. Vandenbem, M. Fink, and R. Carminati, "Subwavelength focusing inside an open disordered medium by time reversal at a single point antenna," *Physical Review A*, vol. 87, p. 041801, Apr 2013.

[30] H. Tu, S. Xiao, D. Lesselier, and M. Serhir, "Super-resolution characteristics based on time-reversed single-frequency electromagnetic wave," *Journal of Electromagnetic Waves and Applications*, vol. 30, no. 13, pp. 1670–1680, 2016.

[31] C. Li, *Electromagnetic Modeling and Simulation of Fiber-Reinforced Periodically-Structured Planar Laminates*. PhD thesis, University Paris-Sud, Sept 2015.

[32] P. C. Hansen, T. K. Jensen, and G. Rodriguez, "An adaptive pruning algorithm for the discrete l-curve criterion," *Journal of Computational and Applied Mathematics*, vol. 198, no. 2, pp. 483 – 492, 2007. Special Issue: Applied Computational Inverse Problems.

[33] P. C. Hansen and D. P. O'Leary, "The use of the l-curve in the regularization of discrete ill-posed problems," *SIAM Journal on Scientific Computing*, vol. 14, no. 6, pp. 1487–1503, 1993.

[34] P. M. van den Berg, A. L. van Broekhoven, and A. Abubakar, "Extended contrast source inversion," *Inverse Problems*, vol. 15, pp. 1325–1344, Oct 1999.

[35] L. Souriau, B. Duchêne, D. Lesselier, and R. E. Kleinman, "Modified gradient approach to inverse scattering for binary objects in stratified media," *Inverse Problems*, vol. 12, pp. 463–481, Aug 1996.

[36] D. Dos Reis, M. Lambert, and D. Lesselier, "Eddy-current evaluation of three-dimensional defects in a metal plate," *Inverse Problems*, vol. 18, pp. 1857–1871, Nov 2002.

[37] O. Dorn and D. Lesselier, "Level set methods for inverse scattering," *Inverse Problems*, vol. 22, pp. R67–R131, Jun 2006.

[38] A. Litman, D. Lesselier, and F. Santosa, "Reconstruction of a two-dimensional binary obstacle by controlled evolution of a level-set," *Inverse Problems*, vol. 14, pp. 685–706, Jun 1998.

[39] A. Litman, "Reconstruction by level sets of n-ary scattering obstacles," *Inverse Problems*, vol. 21, pp. S131–S152, Nov 2005.

[40] X. Chen, "Inverse scattering problems of small scatterers," in *Computational Methods for Electromagnetic Inverse Scattering*, pp. 67–102, IEEE, 2017.

[41] K. Xu, Y. Zhong, X. Chen, and D. Lesselier, "A fast integral equation-based method for solving electromagnetic inverse scattering problems with inhomogeneous background," *IEEE Transactions on Antennas and Propagation*, vol. 66, pp. 4228–4239, Aug 2018.

[42] S. Ioffe and C. Szegedy, "Batch normalization: accelerating deep network training by reducing internal covariate shift," *CoRR*, vol. abs/1502.03167, 2015.

[43] A. Krizhevsky, I. Sutskever, and G. E. Hinton, "Imagenet classification with deep convolutional neural networks," *Communications of the ACM*, vol. 60, p. 84–90, May 2017.

[44] D. Kingma and J. Ba, "Adam: a method for stochastic optimization," *CoRR*, vol. abs/1412.6980v9, 2017.

[45] J. Duchi, E. Hazan, and Y. Singer, "Adaptive subgradient methods for online learning and stochastic optimization," *Journal of Machine Learning Research*, vol. 12, p. 2121–2159, July 2011.

[46] T. Tieleman and G. Hinton, "Lecture 6.5-rmsprop, coursera: Neural networks for machine learning," *University of Toronto, Technical Report*, 2012.

[47] S. Hochreiter and J. Schmidhuber, "Long short-term memory," *Neural Comput.*, vol. 9, p. 1735–1780, Nov. 1997.

[48] J. Chung, Ç. Gülçehre, K. Cho, and Y. Bengio, "Empirical evaluation of gated recurrent neural networks on sequence modeling," *CoRR*, vol. abs/1412.3555, 2014.

[49] F. Lemoult, M. Fink, and G. Lerosey, "Acoustic resonators for far-field control of sound on a subwavelength scale," *Physical Review Letters*, vol. 107, p. 064301, Aug 2011.

[50] P. Ran, Z. Liu, D. Lesselier, and M. Serhir, "Diagnostic within a dielectric microstructure: time-reversal and sparsity-constrained imaging," in *Proceedings of the 13th European Conference on Antennas and Propagation (EUCAP), IEEE Conference Publication*, (Krakow), p. 8740223, 2019.

[51] I. J. Goodfellow, J. Pouget-Abadie, M. Mirza, B. Xu, D. Warde-Farley, S. Ozair, A. Courville, and Y. Bengio, "Generative adversarial networks," 2014.

[52] M. Arjovsky, S. Chintala, and L. Bottou, "Wasserstein GAN," 2017.

[53] Z. Ma, K. Xu, R. Song, C. F. Wang, and X. Chen, "Learning-based fast electromagnetic scattering solver through generative adversarial network," *IEEE Transactions on Antennas and Propagation*, pp. 1–1, 2020.

[54] Y. Sanghvi, Y. Kalepu, and U. K. Khankhoje, "Embedding deep learning in inverse scattering problems," *IEEE Transactions on Computational Imaging*, vol. 6, pp. 46–56, 2020.

[55] S. Dittmer, T. Kluth, P. Maass, and D. Otero Baguer, "Regularization by architecture: A deep prior approach for inverse problems," *Journal of Mathematical Imaging and Vision*, 10 2019.

[56] D. Otero Baguer, J. Leuschner, and M. Schmidt, "Computed tomography reconstruction using deep image prior and learned reconstruction methods," *Inverse Problems*, 07 2020.

[57] N. Abdollahi, D. Kurrant, P. Mojabi, M. Omer, E. Fear, and J. LoVetri, "Incorporation of ultrasonic prior information for improving quantitative microwave imaging of breast," *IEEE Journal on Multiscale and Multiphysics Computational Techniques*, vol. 4, pp. 98–110, 2019.

[58] Y. Qin, T. Rodet, M. Lambert, and D. Lesselier, "Microwave breast imaging with prior ultrasound information," *IEEE Open Journal of Antennas and Propagation*, vol. 1, pp. 472–482, 2020.

Publications

JOURNAL PAPERS

Submitted

P. Ran, S. Chen, M. Serhir, and D. Lesselier, "Imaging of sub-wavelength micro-structures by time reversal and neural networks, from synthetic to laboratory-controlled data," for *IEEE Transactions on Antennas and Propagation*, submitted.

Published

P. Ran, D. Lesselier, and M. Serhir, "Electromagnetic micro-structure non-destructive testing: sparsity-constrained and combined convolutional-recurrent neural networks methods," *Electronics, Special issue New Trends and Future Challenges in Computational Microwave Imaging*, Electronics 2020, 9(11), 1750; https://doi.org/10.3390/electronics9111750.

Published

P. Ran, Y. Qin, D. Lesselier, and M. Serhir "Subwavelength micro-structure probing by binary-specialized methods: contrast source and convolutional neural networks," *IEEE Transactions on Antennas and Propagation*, IEEE Early Access, July 2020, doi: 10.1109/TAP.2020.3016175.

CONFERENCE PAPERS

Oral Presentations

P. Ran, Z. Liu, D. Lesselier, and M. Serhir, "Diagnostic within a dielectric micro-structure: time-reversal and sparsity-constrained imaging," *3th European Conference on Antennas and Propagation (EUCAP)*, Krakow, March-April 2019, IEEE Conference Publication no. 740223 (5 pp), June 2019.

P. Ran "Diagnostic within a micro-structure using a micro-wave and analysis by convolutional neural network," *27th European Signal Processing Conference (EUSIPCO)*, A Coruña, Sept. 2019. 3 Minutes Thesis contest, selected within a 10-person short list of competitors.

P. Ran, D. Lesselier, and M. Serhir, "Convolutional neural network for imaging of micro-structures," *The 42th PIERS, PhotonIcs & Electromagnetics Research Symposium, Focused Session: Machine Learning for Inversion and Imaging*, Xiamen, Dec. 2019.

P. Ran, Y. Qin, D. Lesselier, and M. Serhir, "Imaging of a micro-structure: binary contrast source inversion and convolutional neural networks," *XXXIII General Assembly and Scientific Symposium (GASS) of the International Union of Radio Science*, Rome, August-Sept. 2020. Cancelled due to the pandemics, in Proc. B06-02.

Poster Presentations

H. Tu, M. Serhir, P. Ran, ands D. Lesselier, "On the modeling and diagnosis of a micro-structured wire antenna system," *2018 International Conference on Microwave and Millimeter Wave Technology (ICMMT)*, Chengdu, May 2018. IEEE Conference Publication no. 8563875 (3 pp), Dec. 2018.

P. Ran, Y. Qin, D. Lesselier, and M. Serhir, "Retrieving missing elements of a 2-D micro-structure: joint-sparsity inversion and convolutional neural networks," *9th International Conference on New Computational Methods for Inverse Problems (NCMIP)*, Cachan, May 2019.

P. Ran, Y. Qin, and D. Lesselier, "Electromagnetic imaging of a dielectric micro-structure via convolutional neural network *27th European Signal Processing Conference (EU-*

SIPCO), A Coruña, Sept. 2019, IEEE Conference Publication no. 8903073 (5pp), Nov. 2019.

université PARIS-SACLAY

ÉCOLE DOCTORALE
Sciences et technologies de l'information et de la communication (STIC)

Titre: Imagerie et diagnostic de micro-structures sous-longueur d'onde, d'approches semi-analytiques à l'apprentissage profond

Mots clés: Microstructure, imagerie microonde, apprentissage profond, réseaux neuronaux, représentation parcimonieuse, retournement temporel

Résumé: Le test électromagnétique d'un ensemble fini en forme de grille de tiges diélectriques cylindriques circulaires infiniment longues dont certaines manquent est investigué à partir de données fréquence simple et multiple et en régime temporel. Les distances sous-longueur d'onde entre tiges adjacentes et des diamètres de tige de sous-longueur d'onde sont considérées sur toute la bande de fréquences d'opération et cela conduit à un défi majeur en raison du besoin de super-résolution dans la micro-structure, bien au-delà du critère de Rayleigh.

Tout un ensemble de méthodes de résolution est étudié et des simulations numériques systématiques illustrent avantages et inconvénients, complétées par le traitement de données expérimentales en laboratoire acquises sur un prototype de micro-structure en chambre anéchoïque micro-onde. Ces méthodes, qui diffèrent selon les informations a priori prises en compte et la polyvalence qui en résulte, comprennent retournement temporel, inversions de source de contraste, binaires ou parcimonieuses, ainsi que réseaux de neurones convolutifs éventuellement combinés avec des réseaux récurrents.

Title: Imaging and diagnostic of sub-wavelength micro-structures, from closed-form algorithms to deep learning

Keywords: Microstructure, microwave imaging, deep learning, neural networks, sparsity representation, time reversal

Abstract: Electromagnetic probing of a grid-like, finite set of infinitely long circular cylindrical dielectric rods affected by missing ones is investigated from time-harmonic single and multiple frequency data. Sub-wavelength distances between adjacent rods and sub-wavelength rod diameters are assumed throughout the frequency band of operation and this leads to a severe challenge due to need of super-resolution within the present micro-structure, well beyond the Rayleigh criterion.

A wealth of solution methods is investigated and comprehensive numerical simulations illustrate pros and cons, completed by processing laboratory-controlled experimental data acquired on a micro-structure prototype in a microwave anechoic chamber. These methods, which differ per a priori information accounted for and consequent versatility, include time-reversal, binary-specialized contrast-source and sparsity-constrained inversions, and convolutional neural networks possibly combined with recurrent ones.

Université Paris-Saclay
Espace Technologique / Immeuble Discovery
Route de l'Orme aux Merisiers RD 128 / 91190 Saint-Aubin, France